Solution Processed Electronics for Flexible Hybrid Electronic Systems

Jonathan Ting

Electrical Engineering and Computer Sciences
University of California, Berkeley

May 1, 2023

Solution Processed Electronics for Flexible Hybrid Electronic Systems

by

Jonathan K'ang-Yu Ting

A dissertation submitted in partial satisfaction of the

requirements for the degree of

Doctor of Philosophy

in

Engineering - Electrical Engineering and Computer Sciences

in the

Graduate Division

of the

University of California, Berkeley

Committee in charge:

Professor Ana Claudia Arias, Chair
Professor Jan M. Rabaey
Professor Lydia Sohn

Spring 2021

Solution Processed Electronics for Flexible Hybrid Electronic Systems

Abstract

Solution Processed Electronics for Flexible Hybrid Electronic Systems

by

Jonathan K'ang-Yu Ting

Doctor of Philosophy in Engineering - Electrical Engineering and Computer Sciences

University of California, Berkeley

Professor Ana Claudia Arias, Chair

Recently, form factors of electronics have been changing from conventional rigid electronics to more novel and complex form factors including soft, flexible, and even stretchable forms. These unique form factors are lightweight and enable conformal interfaces between electronics and the objects they rest upon. Printing is a commercially viable manufacturing technology for fabricating these types of electronics, capable of depositing materials including conducting, insulating, and semiconducting materials. However, printed flexible electronics are not as efficient as silicon integrated circuits (ICs) in certain regimes, such as computation or communication. Flexible hybrid electronics (FHE) leverage the benefits of flexible printed electronics and ICs by combining the two onto flexible substrates.

In this dissertation, I will discuss the various components of an FHE system and the range of printing techniques that are used to fabricate them. This dissertation will also overview specific works highlighting advancements in developing FHE systems. For passive sensing applications, I will focus on our work on screen-printed thermistor arrays, and their applications in battery health monitoring. For active sensing applications, I will discuss our work using doctor-blade coated arrays of organic light-emitting diodes (OLEDs) and organic photodiodes (OPDs) for reflection mode blood oximetry, which accurately measures pulse rate and oxygenation. In addition to the discussion of the flexible sensor composed of OLEDs and OPDs, I will present our work on various unique geometries of optoelectronics and their significance in improving sensor efficiency. For power sources, I will present our work on screen-printed $Zn-Ag_2O$ battery arrays, and the scalability of these devices. Finally, I will discuss other techniques to develop robust conformal electronics, using a class of FHE systems called in-mold electronics.

This dissertation is dedicated to my parents, Yuan-Ping Ting and Wen-Hua Shui

Contents

List of Figures

List of Tables

Acknowledgments

Many different people at different points in my life have guided me to where I am now, as I finish my doctoral dissertation at UC Berkeley.

First of all, the person I must thank the most is my advisor, Prof. Ana Claudia Arias. Thanks to Ana, I had plenty of opportunities to work on various projects in a new and emerging field of electronics. Especially as a new student in a research group, there was never a scenario where I didn't have something to learn, or someone to learn from. Ana always let me move from project to project without asking any questions, and she always prioritized letting me work on the things I found fun or interesting. Ana was my biggest supporter, and my voice of reason and confidence, even when I couldn't find confidence in myself. She always listened to my concerns and my doubts, and countered calmly and logically with her years of experience. Not only did I learn significant technical knowledge through Ana's mentorship, but I also learned so much more about how I think, as well as how to best navigate my self-doubt. Ana's guidance has helped me grow into the researcher and person I am today, and behind the scenes she is doing so much more than what meets the eye. By slowly giving me more responsibilities and opportunities to develop my abilities as a researcher, such as presentations, trade-shows, and conferences, Ana has helped me develop some of the softer skills that aren't easily taught. Ana's mentorship has really shaped my experience as a Ph.D. student at UC Berkeley, and I believe there is no better group I could have joined.

The work presented in this dissertation could not have been possible without the support from the funding sources - National Science Foundation (NSF), Systems on Nanoscale Information fabriCs (SONIC), NextFlex, Intel Corporation, and Cambridge Display Technology Limited (CDT). In addition, I am most thankful for the EECS Departmental Fellowship.

My Ph.D. consists of many different projects, all amazing collaborations with brilliant people. Starting with the oximiter project, I'd like to thank Yasser Khan and Donggeon Han specifically for many hours in the dark room making PPG measurements, we had some great times. I'd also like to acknowledge Claire Lochner, Adrien Pierre, and Xingchun Wang for starting the project and allowing me to join when I started my Ph.D. In addition, I'd like to acknowledge Nir Yaacobi-Gross, Chris Newsome, Richard Wilson, Gianluca Bovo, Simon King, and Martin Humphries from Cambridge Display Technology for their support both by providing materials as well as helpful technical discussions. For the printed thermistor array project, I'd like to thank Yasser Khan, Natasha Yamamoto, and Abhinav Gaikwad for a fun side project and exciting battery testing. As part of a collaboration with NovaCentrix, we were able to start a collaboration with Prof. Jan Rabaey's group in developing printed electromyography electrodes used for real time gesture classification. I'd like to thank Yasser Khan, Natasha Yamamoto, Ali Moin, Andy Zhou, Abbas Rahimi, Simone Benattiz, Alisha Menon, Senam Tamakloe, Fred Burghardt, Luca Beninyz, Prof. Rikky Muller, and Prof. Jan Rabaey. For the NextFlex project, I'd like to thank Yasser Khan, Donggeon Han, Natasha Yamamoto, Carol Baumbauer, Juan Zhu, Jasmine Jan, Maruf Ahmed, Sina Faraji, Arno Thielens, Prof. Jan Rabaey, and Prof. Rikky Muller. I'd also like to thank Kaiping

x

Having a close friend who is also doing their Ph.D. really is a blessing, and we were truly able to share our experiences during our graduate studies. I am thankful that Kuan was always willing to listen to my frustrations in the lab, and he was willing to vent to me about his frustrations, even though we don't work on anything remotely related to each other. Thanks buddy, you're a real one.

Finally, the biggest thank-you must go to my parents, Yuan-Ping Ting and Wen-Hua Shui. They have supported me in so many ways since I left for college, and have been the most understanding parents I could ask for. When I put pressure on myself to do things a certain way, they were the people who told me no matter what it would be okay. When I rushed into graduate school doubtful of my own abilities, they were the ones who knew I was truly capable of much more than what I thought I was. When I was uncertain of what my future after graduate school would be, they were the ones who told me to take my time and figure things out as they come. Because of my parents, I knew no matter how bad of a day I had in the lab, I would have someone to talk to about it. Without their support and motivation, I definitely could not have made it through my graduate studies in one piece. Finishing a Ph.D. is **hard**, and having people who are there to support you is key to pushing through it. Those people are undoubtedly my parents.

I truly had a wonderful experience at Berkeley, and all of these people that I have thanked are the main reason why it was a smooth transition into a new city and lifestyle. Having consistently nice weather and many places to visit around the area makes the time off from research incredibly enjoyable. The quality of research and academic rigor that Berkeley provides is something that inspired me and kept me going throughout my time as a student. I am very grateful for this wonderful community that has supported me throughout my entire Ph.D. journey.

<div align="right">

Jonathan K'ang-Yu Ting
May, 2021
Berkeley, CA

</div>

Chapter 1

Introduction

1.1   Flexible electronics

Flexible electronics is a relatively broad term. In general, it encompasses any sort of electronics fabricated on a flexible substrate, substrate being the material that holds up the rest of the electronics in this sense. In recent years, this form factor of flexible electronics has really shifted from the traditional rigid, rectangular form factor, to a variety of new possibilities [1–8]. Researchers today are now looking into substrates made of plastic, paper, and even stretchable materials. Each of these substrates has individual challenges associated with them, such as surface energy, roughness, chemical compatibility, and thermal budget. One of the main advantages of flexible electronics is its form factor. A trend we will see throughout this dissertation is how having conformal electronics improves the use of printed sensors. Due to the conformal nature of flexible electronics, the interface between flexible electronics and the objects they are placed on is significantly more robust compared to a rigid printed circuit board (PCB). Take the circuit in Figure 1.1 for example: this flexible electronic circuit sits very nicely in the palm of the user, and we can see that it comforms very well to the various contours in the hand due to the flexible substrate the electronics are fabricated on. If we were to reimagine the same circuit on a conventional rigid PCB, we would see that the circuit wouldn't sit very well in the palm of the hand, nor would the electronics be sitting flush to the skin at all points of the circuit. There are a variety of applications where conformal electronics are a better form factor than rigid electronics, especially in the wearables and health sensing regime [4, 6, 7, 9–11, 11–16].

Although there have been major advancements in the realm of printed flexible electronics, especially in sensors, there are still a few major limitations in the current research grade devices. Most printed flexible electronics suffer from low yield, reduced lifetime, and high power consumption. In comparison to the conventional rigid electronics, silicon integrated circuits (ICs), printed electronics simply cannot provide the computational power required to develop full systems capable of interfacing with the printed flexible electronics. In general, silicon ICs have significantly fewer issues on this front, with standardized fabrication tech-
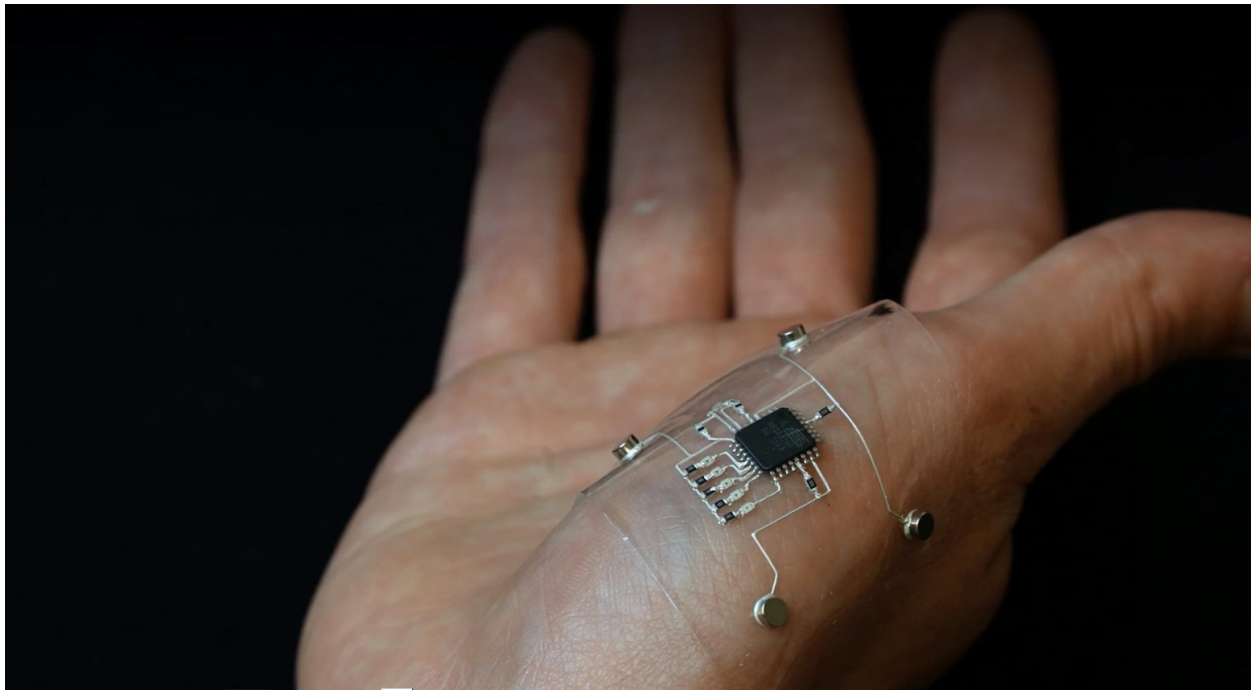
Figure 1.1: **ARFL, Harvard collaboration on 3D printed flexible electronics.** Figure from [17].

niques and highly optimized designs they have very good yield and performance, however are still limited by their bulky package sizes and form factors. In addition, the fabrication techniques required for silicon ICs typically involve vacuum deposition, making scaling to large area fabrication very difficult and costly.

Flexible Hybrid Electronics (FHE) is a concept introduced to leverage both the advantages of printed flexible electronics and conventional rigid ICs. As discussed earlier, the form factor advantage of printed flexible electronics is huge and can even improve sensing capabilities of lower quality sensors due to the highly conformal nature of the flexible electronics. Similarly, the reliability and high performance aspects of silicon ICs cannot be ignored. By combining the two, both printed flexible electronics and rigid silicon ICs, onto a single substrate we can utilize and maximize the advantages of both realms simultaneously on one platform for electronics. By using component mounting techniques, such as pick and place, we can attach silicon ICs onto flexible substrates with printed electronics fabricated directly on top of them. Ultimately, the scalability and flexibility of printed electronics is preserved, while gaining the computational power and reliability of silicon ICs on a new flexible platform.

There are a variety of ways to implement FHE, and a concept art from the NextFlex consortium is shown in Figure 1.2. This figure outlines a schematic of a FHE system, and

some components typically involved in FHE. There are a variety of components that can be printed, that are mostly printed, and are not usually printed categorized in this image. Starting with the components that can be printed, there has been a large amount of research in printed displays and printed interconnects. As discussed earlier, printing techniques can accommodate all sorts of materials, including conductors, semiconductors, and dielectrics. For printed interconnects, it is most commonly done with printed silver, however recent work has shown advancements in printed silver with plated copper. For printed displays, there is a huge effort in the printed organic light emitting diode (OLED) research area [2, 6, 7, 12, 18], and much of the research is focused on developing highly efficient emitters and scaling down pixel sizes to as small as possible, rivaling that of evaporated display configurations. That being said, there are many compatible technologies that do not require printing for displays and interconnects. Many commercial flexible printed circuit boards are developed with single layer copper, and there are many AMOLED displays that can be directly mounted onto a variety of substrates. Moving onto components that are mostly printed, these include thin film batteries, antennas, and polymer solar cells. Printed antennas have been developed over many years, and especially with the advancements in conductivity for solution processed metals, the quality of printed antennas is close to that of PCB antennas. From a fabrication perspective, a single layer of printed conductor, and perhaps a printed dielectric, is sufficient to develop a printed antenna for most NFC/RFID applications [5] For printed power, energy harvest and batteries are both viable printed technologies. There are a variety of printed solar cell works involving organic photovoltaic (OPV) materials, and several different battery chemistries have been shown in literature. Finally, there are a variety of components that are not usually printed for FHE systems. This usually includes microprocessors and memory, as there are silicon equivalents that are reliable and well commercialized.

If we break down the various components discussed into several categories, we can see there are generally four major categories: active components, passive components, power sources, and integrated chips. In general, components such as displays and certain sensors that draw power are considered active components. Passive components include components such as interconnects and sensors that do not draw power. Power sources included energy harvesting solutions and energy storage, such as batteries [8–10, 12, 19]. And finally integrated chips includes microcontrollers and any other logic that requires the assistance of ICs. Despite being four very broad categories, many of the components included in active components, passive components, and power sources can be printed. As part of this dissertation, we will discuss several works that showcase examples of each of these categories and how they can fit into the bigger picture of flexible hybrid electronic systems. For passive components, we discuss our work on printed thermistor arrays for battery health monitoring. For active components, we discuss our work on printed optoelectronics, and a multi-channel reflection mode oximeter. Finally, for power sources, we discuss our work on printed Zn-Ag_2O battery arrays. It should be noted that these are not the only works demonstrating each of these categories, however they have been selected for their importance during my Ph.D.
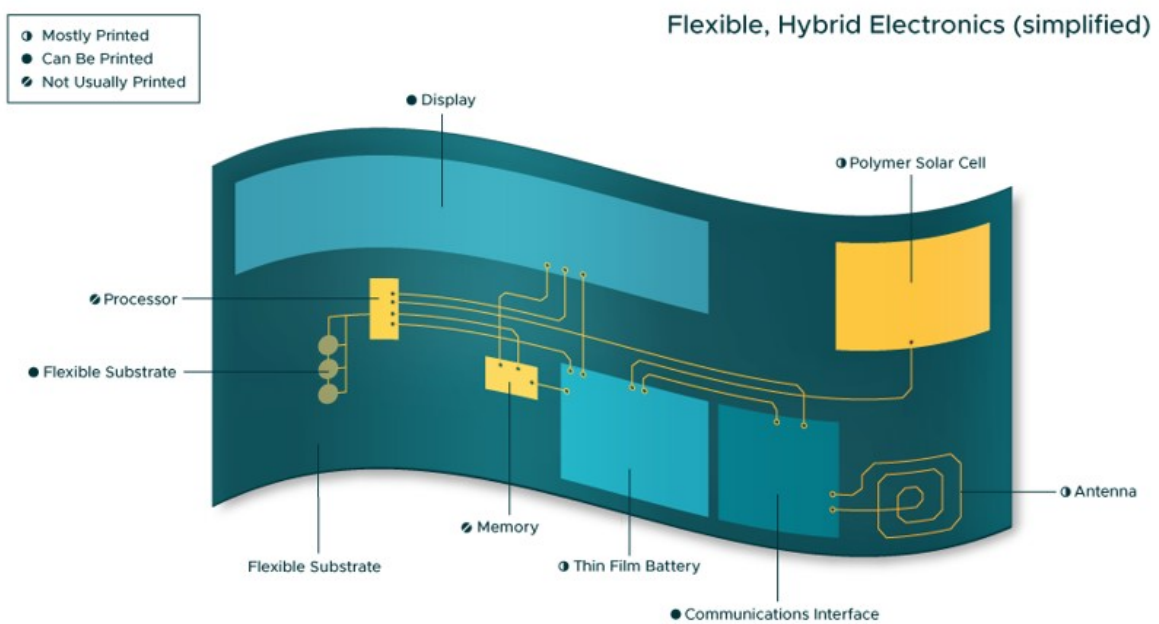
Figure 1.2: **Concept art of flexible hybrid electronic system.** Various components are identified as mostly printed, can be printed, or not usually printed. Figure from [20].

1.2 Printing methods

The advantages of using printing as a manufacturing method for flexible electronics is pretty extensive. Firstly, printing is typically considered an additive manufacturing process. This means that materials are deposited additively in a vertical fashion, building more and more layers to finish a full device stack. In contrast, many commercial silicon IC fabrication techniques require the use of lithography and etching based approaches, a subtractive process, starting with blanket deposition of material and removing excess as necessary. In general, solution processing also simplifies the fabrication process and removes the need for vacuum deposition, lithography, and etch steps. On this note, printing is considered a high throughput process. Commercial printing processes are on a roll-to-roll manufacturing line, and can have speeds up to meters/second per roll. In contrast, many conventional fabrication processes are heavily limited by vacuum deposition processes, which require time to pump down and evaporate. Similarly, many printing processes are highly scalable in comparison with conventional techniques. This means that regardless of the substrate dimensions, most printing techniques take the same amount of time to process, with only the amount of material that needs to scale. Processes that involve vacuum deposition do not scale well due to larger substrates requiring larger vacuum chambers, and thus longer pump down times. There are a variety of materials that printing can process as well. These include dielectrics, conductors, and semiconductors, which all enable a variety of applications for solution processing. One of the most common solution processing techniques is spin-coating, however it isn't considered a printing process. This involves depositing a small amount of ink on the surface of a substrate and spinning it at high speed to spin off excess ink, and leave a uniform film of ink the surface. Although this does have great yield, it is primarily considered a prototyping technique in our lab, with the intention of scaling to some of the following printing processes.

As mentioned, there are a variety of printing techniques available, and several of them are shown in Figure 1.3. Figure 1.3a shows the schematic process of inkjet printing. Inkjet printing involves a small print head with a piezoelectric nozzle that can dispense very controlled volumes of ink. Depending on the waveform provided to the nozzle, this volume of ink can be precisely varied. Inkjet printing is one of the few processes that is purely additive, and with the advancements with drop on demand technology, drops of ink can be deposited precisely in locations anywhere on the substrate. By merging several drops of ink, larger features can be formed. It should be noted that inkjet printing is not a very area high scaling process due to its raster scan printing process. Because it prints along both the x and y axis at every point, regardless of if there is a feature or not, scaling to larger areas requires significantly longer time. In addition, when printing very fine features, it can be difficult to detect defects and shorts without the assistance of an optical microscope. However, it should be noted that inkjet printing has the highest resolution and smallest possible feature spacing out of all the printing techniques, with resolutions as small as 20 μm, and films on the nanometer scale. Doctor blade coating, in Figure 1.3b, is the next printing technique, and involves using a doctor blade to uniformly guide ink across the surface of a substrate.

There are a variety of parameters that have an effect on the thickness of the film, including viscosity, blade speed, blade height, and surface energy. It should be noted that this printing technique is a non-contact method, meaning the blade never physically contacts the substrate itself, which is very good for thin sensitive films. Finally, the last technique discussed, in Figure 1.3c, is screen-printing. Screen-printing is very good for printing thicker films, especially due to the high viscosities of inks that it uses. Ink is first deposited on a patterned mesh and flooded with the flood bar to uniformly spread ink over the surface. From there, a squeegee moves across the surface of the screen applying pressure to force ink through the patterned openings and transfer, via contact, ink onto the substrate. Most of these inks are in the 1,000 - 10,000 cP range, and have a unique shear thinning behavior. There are several important parameters of optimization, including ink viscosity, substrate surface energy, squeegee pressure, and snap off distance.

1.3   Thesis organization

This thesis primarily describes the various design and fabrication challenges for each of the various components generalized in a FHE system. Because there are a variety of printing techniques available for each application, selecting the printing technique that is most suited for the application at hand is critical to the optimization and performance of these devices. The printing techniques used throughout this dissertation have already been outlined above, and each section will go into the critical optimization techniques and analysis for the device fabricated.

Chapter 2 goes through one example of passive components, printed thermistors. Temperature is a commonly measured signal in a variety of applications. Specifically motivated by the lack of *in vivo* battery health monitoring solutions, we explore a printed thermistor array for real time temperature mapping. Monitoring batteries for local heating can indicate regions of low series resistance, which can cause thermal runaway during battery operation. The fabrication process for the 4 x 4 array of thermistors involves screen-printing two layers of ink, one NiO sensing film and one silver electrode film. As there is no commercially available NiO ink for screen-printing, we optimized the NiO ink for film quality and uniformity by characterizing the viscosity of the ink. In addition, we explored various anneal times and film thicknesses to improve the sensitivity of the devices. Finally, the array is characterized with a commercially available Lithium-ion battery discharged at various C-rates, and compared with a commercial thermal camera to validate the accuracy of the printed devices. In addition to the thermistor characterization, a thorough analysis of design rules and toolkits for screen printing is outlined, including design and feature limits, as well as the process to submit a screen design.

Chapter 3 introduces an example of active components, printed optoelectronics. As most of my work during my PhD involves printed OLEDs, a thorough discussion of OLED performance metrics is included. In addition, two different measurement setups are discussed: integrating sphere and a custome photodiode measurement setup. The design of the photo-

diode setup is included, as well as an in depth discussion of the control software. In addition, an emission angle measurement setup is discussed and validated. From here, an example of optoelectronic sensing is discussed in detail, a multi-channel reflection oximeter. The oximeter uses both printed OLEDs and OPDs, and the assembly of the sensor is discussed in detail. Several different sensor design schemes are introduced and evaluated including varying pixel geometry and spacing, as well as introducing optical isolation between the emitter and detector. Finally, the overall performance of each sensing scheme is analyzed and compared via their calibrated photoplethysmogram signal magnitude.

Chapter 4 explores one example of printed power sources, Zn-Ag_2O batteries. Specifically, arrays of Zn-Ag_2O batteries are designed and connected in series to allow for application specific design flexibility. The design of the individual Zn-Ag_2O battery is discussed in detail, as well as the series interconnect scheme enabling any integer multiple of 1.5 V to be achieved. Furthermore, a custom electrode ink slurry was developed for both Zn and Ag_2O, and the optimization of the various electrode films are analyzed. Specifically, ink viscosity, mass loading, number of print passes, and screen integrity and their effects thoroughly analyzed. Finally, the characterization of both the single cell battery and arrays of various dimensions are shown.

Chapter 5 focuses on another approach in designing flexible hybrid electronics, specifically for applications demanding highly conformal designs for complex surfaces. The concept of in-mold electronics is introduced, as well as the various design processes associated with a standard in-mold electronics design approach. A software assisted design approach is proposed and outlined, and the fabrication process for in-mold electronics is thoroughly discussed. Key design criteria are discussed for the pick and place component attach process, and an optimized in-mold electronics fabrication process is explained. Additional design criteria for vacuum forming and mold design are outlined, and several examples of finished in-mold electronics are discussed. Finally, a detailed analysis of the software toolkit design is discussed with relevant algorithms.

Chapter 6 concludes this thesis. Several future works will be discussed including integrated impedance and optoelectronic sensors for wound monitoring and stimulation, printed sensors for food packaging, printed vias enabling double-sided electronics, and SimuPrint: multi-functional single substrate printed electronics. An overview of each future work with additional details about potential implementation will be discussed.
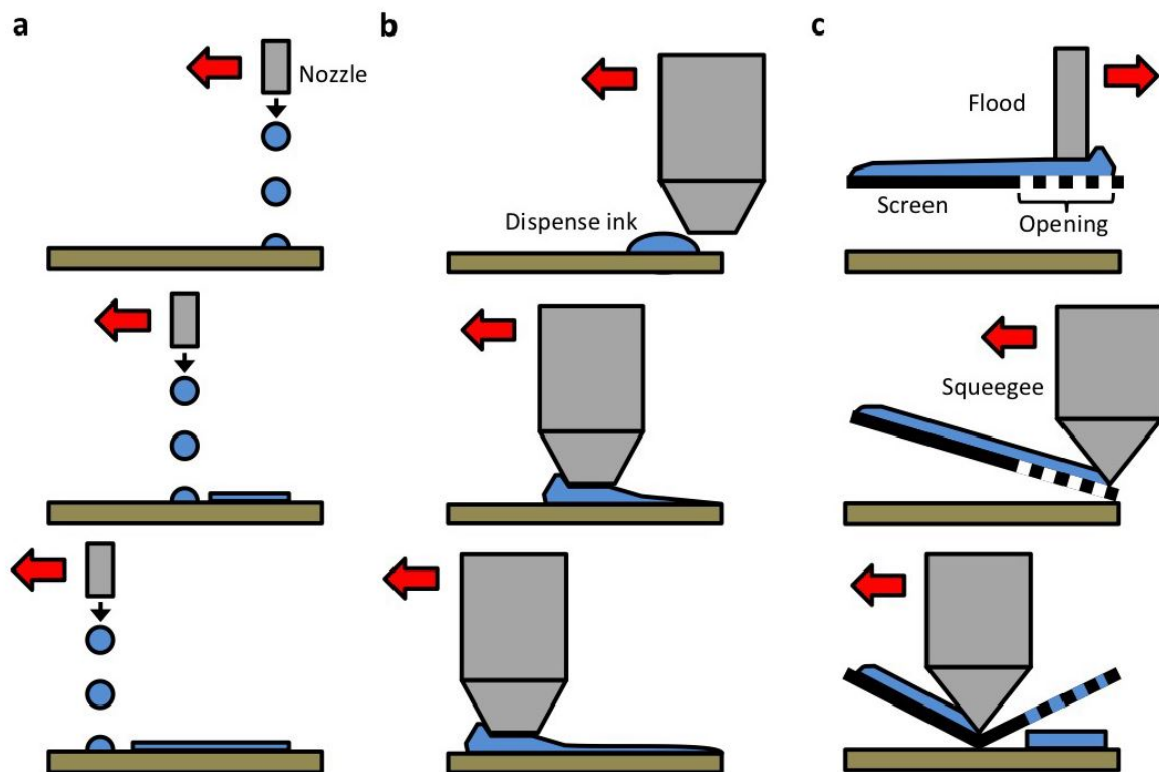
Figure 1.3: **Schematic view of various printing techniques.** Schematic of **(a)** inkjet printing technique, **(b)** doctor blade coating technique, and **(c)** screen-printing technique. Figure from [21].

1.4 References

[1] Ali Moin, Andy Zhou, Abbas Rahimi, Simone Benatti, Alisha Menon, Senam Tamakloe, Jonathan Ting, Natasha Yamamoto, Yasser Khan, Fred Burghardt, Luca Benini, Ana C. Arias, and Jan M. Rabaey. An EMG gesture recognition system with flexible high-density sensors and brain-inspired high-dimensional classifier. *arXiv*, 2018.

[2] Donggeon Han, Yasser Khan, Karthik Gopalan, Adrien Pierre, and Ana C. Arias. Emission Area Patterning of Organic Light-Emitting Diodes (OLEDs) via Printed Dielectrics. *Advanced Functional Materials*, 28(37), 2018.

[3] Chun Chih Huang, Zhen Kai Kao, and Ying Chih Liao. Flexible miniaturized nickel oxide thermistor arrays via inkjet printing technology. *ACS Applied Materials and Interfaces*, 5(24):12954–12959, 2013.

[4] Yu Liao, Rui Zhang, and Jun Qian. Printed electronics based on inorganic conductive nanomaterials and their applications in intelligent food packaging. *RSC Advances*, 9(50):29154–29172, 2019.

[5] Carol L. Baumbauer, Matthew G. Anderson, Jonathan Ting, Akshay Sreekumar, Jan M. Rabaey, Ana C. Arias, and Arno Thielens. Printed, flexible, compact UHF-RFID sensor tags enabled by hybrid electronics. *Scientific Reports*, 10(1):1–12, 2020.

[6] Tim R. Dargaville, Brooke L. Farrugia, James A. Broadbent, Stephanie Pace, Zee Upton, and Nicolas H. Voelcker. Sensors and imaging for wound healing: A review. *Biosensors and Bioelectronics*, 41(1):30–42, 2013.

[7] Claire M. Lochner, Yasser Khan, Adrien Pierre, and Ana C. Arias. All-organic optoelectronic sensor for pulse oximetry. *Nature Communications*, 5:1–7, 2014.

[8] Abhinav M. Gaikwad, Alla M. Zamarayeva, Jamesley Rousseau, Howie Chu, Irving Derin, and Daniel A. Steingart. Highly stretchable alkaline batteries based on an embedded conductive fabric. *Advanced Materials*, 24(37):5071–5076, 2012.

[9] Woo Jin Hyun, Ethan B. Secor, Mark C. Hersam, C. Daniel Frisbie, and Lorraine F. Francis. High-resolution patterning of graphene by screen printing with a silicon stencil for highly flexible printed electronics. *Advanced Materials*, 27(1):109–115, 2015.

[10] Rajan Kumar, Jaewook Shin, Lu Yin, Jung Min You, Ying Shirley Meng, and Joseph Wang. All-Printed, Stretchable Zn-Ag2O Rechargeable Battery via Hyperelastic Binder for Self-Powering Wearable Electronics. *Advanced Energy Materials*, 7(8), 2017.

[11] Yasser Khan, Felippe J. Pavinatto, Monica C. Lin, Amy Liao, Sarah L. Swisher, Kaylee Mann, Vivek Subramanian, Michel M. Maharbiz, and Ana C. Arias. Inkjet-Printed Flexible Gold Electrode Arrays for Bioelectronic Interfaces. *Advanced Functional Materials*, 26(7):1004–1013, 2016.

[12] Yasser Khan, Donggeon Han, Jonathan Ting, Maruf Ahmed, Ramune Nagisetty, and Ana C. Arias. Organic multi-channel optoelectronic sensors for wearable health monitoring. *IEEE Access*, 7:128114–128124, 2019.

[13] Manuel Ochoa, Rahim Rahimi, and Babak Ziaie. Flexible sensors for chronic wound management. *IEEE Reviews in Biomedical Engineering*, 7:73–86, 2014.

[14] Nattinee Bumbudsanpharoke, Jungwook Choi, and Seonghyuk Ko. Applications of nanomaterials in food packaging. *Journal of Nanoscience and Nanotechnology*, 15(9):6357–6372, 2015.

[15] Tiina Vuorinen, Juha Niittynen, Timo Kankkunen, Thomas M. Kraft, and Matti Mäntysalo. Inkjet-printed graphene/PEDOT:PSS temperature sensors on a skin-conformable polyurethane substrate. *Scientific Reports*, 6(September):1–8, 2016.

[16] Kaiping Wang, Udit Parekh, Jonathan K. Ting, Natasha A.D. Yamamoto, Juan Zhu, Todd Costantini, Ana Claudia Arias, Brian P. Eliceiri, and Tse Nga Ng. A Platform to Study the Effects of Electrical Stimulation on Immune Cell Activation During Wound Healing. *Advanced Biosystems*, 3(10):1–8, 2019.

[17] AFRL, Harvard researchers invent new hybrid 3-D printing method for flexible electronics. https://www.af.mil/News/Article-Display/Article/1345387/afrl-harvard-researchers-invent-new-hybrid-3-d-printing-method-for-flexible-ele/, Accessed: 10/3/2020.

[18] Yasser Khan, Arno Thielens, Sifat Muin, Jonathan Ting, Carol Baumbauer, and Ana C. Arias. A New Frontier of Printed Electronics: Flexible Hybrid Electronics. *Advanced Materials*, 32(15):1–29, 2020.

[19] Abhinav M. Gaikwad, Daniel A. Steingart, Tse Nga Ng, David E. Schwartz, and Gregory L. Whiting. A flexible high potential printed battery for powering printed electronics. *Applied Physics Letters*, 102(23), 2013.

[20] NextFlex Flexible Hybrid Electronics. https://www.nextflex.us/about/about-fhe/, Accessed: 5/1/2020.

[21] Adrien Pierre. Printed Organic Thin Film Transistors , Photodiodes , and Phototransistors for Sensing and Imaging. 2016.

Chapter 2

Printed thermistor arrays

2.1   Introduction

There are a variety of signals monitored by passive sensing technologies today. Temperature is a useful signal that is frequently used to evaluate the status of a variety of mechanical or microelectronic systems. A few temperature monitoring applications include IC chips, heat sinks, metal structural integrity, and battery health. Although using individual temperature sensors does provide meaningful information, an array of sensors is capable of measuring the spatial distribution of temperature, as well as provides signal redundancy.

Large-area printing has gained significant interest and is becoming one alternative to conventional lithography-based processes, especially for applications that require large area coverage of components. There are a variety of printing techniques available, but screen-printing is a particularly appealing method for large area material deposition and is in use today in manufacturing scale processing. The low complexity printing, fast turnaround time, and uniform large area deposition of materials that screen-printing enables makes it an attractive additive manufacturing process.

In order to monitor temperature over a surface, the sensors must be sitting as close to the surface of interest as possible to form a high-fidelity sensor-surface interface. With this in mind, fabricating large area flexible thermistors would enable this type of interface. Although semiconducting manufacturing technologies are reliable and widely used, they tend to require high vacuum or temperature environments, and have poor areal scaling for custom designs. In addition, these manufacturing techniques usually require lithography or additional masking steps, which can be expensive and result in high material waste.

In this chapter, we report on a fully screen printed 4 x 4 thermistor array. The thermistor array is highly sensitive and demonstrates temperature coefficient, α = -5.84 % K^{-1} and material constant, β = 4302 $\pm$ 401 K. This array can be applied not only for wearable and medical applications such as measuring skin temperature, but it could also be used for battery health monitoring as illustrated in Figure 2.1. We used the 4 x 4 array of thermistors to measure the temperature of a commercial lithium ion battery when operated at higher
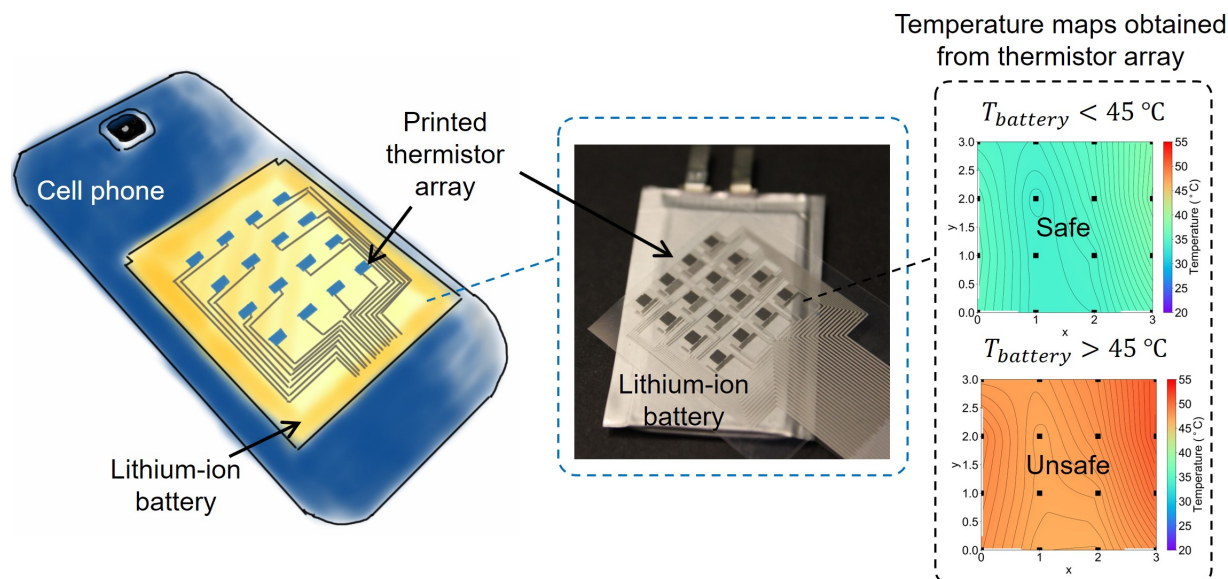
Figure 2.1: **Concept art for fully screen printed thermistor array used in as battery temperature monitoring sensor.** The 4 x 4 array would be placed on top of a battery and would monitor the heating, producing a real-time temperature map of the surface. The data obtained with the proposed device would be useful in monitoring battery performance, helping to prevent dangerous failure mechanisms resulted from overheating.

C-rates. By multiplexing the individual thermistor pixels, we were able to plot, in real-time, the temperature of the battery surface, and spatially resolve local heating. Additionally, the screen-printing was done on flexible plastic substrates, making the sensor array conformal to the object being measured, allowing higher efficiency at resolving surface temperatures when compared to conventional rigid thermistors [1–16]. Portions of this chapter are submitted for review in [1].

2.2   Thermistor array fabrication

The temperature sensitive ink used for the thermistor is composed of NiO nanoparticles mixed with a polystyrene–butadiene rubber (PSBR) binder and water. The number of charge carriers in the conduction band of NiO increases with higher temperature, resulting in a decrease in the resistivity. The PSBR holds the nanoparticles together to form the thermistor layer. An array of fabricated thermistors on PEN substrates is shown in 2.2. First, square pads of NiO are deposited on the PEN substrate using screen printing. After annealing the NiO, the conductive silver pads and traces are then screen printed directly on top of the NiO pads. The two-step process is depicted in 2.2a, with the inset showing a

magnified image of an individual thermistor pixel stack. Depending on the design, a variety of sensor densities can be achieved, as seen in 2.2b-d. The inset image of 2.2d shows the magnified image of the NiO pads, which have dimensions of 900 μm x 900 μm.

2.3 Screen-design guidelines

2.3.1 Design rules

In order to effectively print films using screen-printing, there are a variety of design rules that should be followed in the screen designing process. For the screen printer described in this work, we are assuming that we have a minimum feature distance of roughly 125 μm. Knowing this parameter is crucial to determining how to layout the various parts of the screen. An additional parameter used in the design process is the maximum printable area of the screen. Although the screen itself is very large, the printable region of the screen is determined by the squeegee width and the vertical actuation distance during the travel along the screen. For our printer, these dimensions are 150 x 170 mm. In addition, it is recommended to place most features as close to the center of the print axis as possible, to avoid any print region related defects. An example of a screen design used for this work is shown in Figure 2.3. If we look at this particular design, we can see there are a variety of design features on the screen. There are arrays of various different design densities, as well as electrode spacings. It should be noted that for any design that requires two or more layers, alignment marks are **mandatory** on the screen for each layer. This allows the user to vertically align consecutive layers using the fiducial camera on the screen printer. For this particular screen, each design has a small printed cross that acts as the alignment mark. One should take caution when designing placing these alignments, especially for smaller designs, as there is a physical limit on how close one can place the fiducial cameras on the screen printer without overlapping them.

Additionally, it is recommended to place a set of test structures on a screen when working with new or unfamiliar ink compositions. This primarily functions to allow the user to characterize several ink parameters, such as thickness, spreading, and feature definition without having to make a separate screen to do so. There is, in theory, a location dependence to these test structures, however it is in general negligible for most applications. As seen in Figure 2.4, we can see a zoomed in photo of an array design in 2.4a, as well as some test structures used in Figure 2.4b. Printing several lines of varying linewidth or length allows for quick 4 point probe measurements to characterize resistivity, and designing several squares of different dimensions allows one to test ink spreading.

There are a variety of issues one could encounter during screen-printing, and that warrants a dissertation on its own, however one of the most common issues to debug while working with conductive inks is electrode shorting. Figure 2.5 shows an example of two printed silver electrodes that have shorted on a microscopic level. To the naked eye, this would be very difficult to detect, however upon closer inspection it can be determined that the electrodes

are indeed slightly shorted. This is a sign that the screen design has reached the lower limit of feature separation. As we can see, this particular separation of electrodes seems to be below 125 μm, and with ink spreading this effect can occur at even larger spacing.

Figure 2.6 is a great example of the difference between designed feature specifications and actual printed specifications. For this particular flat flexible connector (FFC), the printed silver lines were designed to have a pitch of 1 mm, with each trace having a width of 750 μm and each space having a width of 250 μm. However, upon measuring the printed traces on the optical microscope, it can be seen that they have values closer to 800 μm and 200 μm respectively. This implies there is roughly a 25 μm spreading effect for the printed silver traces. Knowing this value is particularly helpful, and can potentially be accounted for in future design iterations by adjusting design dimensions. Specifically for connectors, it is particular helpful to design connectors such that precise alignment is not required should there be any ink spreading into adjacent pads. For example, this connector was used with a 500 μm pitch connector, however two traces and one gap were shorted together to avoid precise alignment requirements.

2.3.2   Toolkits

There are a variety of tools one could use to design screens for screen-printing. Personally, the most convenient design software has been AutoCAD in 2D. Most screen order companies use Gerber (.gbr) file formats to layout screens. However, many of them accept .dwg or .dwx file formats nowadays, and this is the default output format of AutoCAD. For designs such as Figure 2.4a, laying out geometric components such as square pads is quite trivial in AutoCAD, however there is no convenient trace routing function. To do so requires a combination of AutoCAD and a PCB layout software. I have found using DipTrace (freeware) is convenient in combination with AutoCAD. The easiest way to combine the two is to design all of the printed electrodes and features as closed objects in AutoCAD and export it as a .dxf file. DipTrace can handle .dxf files and they can be imported as "pads" into the layout software. From there, each component can be placed, just like in PCB layout, and routed manually using the DipTrace routing tool. I personally recommend designing the FFC separately such that you can use it like a library and import it to whatever project you need in the future. After the design has been completely routed, the DipTrace file can be exported in a few different file formats. I personally prefer exporting it in the .dxf file format, specifically exporting the "TOP" and "EDGE TOP" layers, however one could also directly export to .gbr, it is merely a matter of personal preference. From there, the files can be sent to the screen design company and a screen can be ordered.
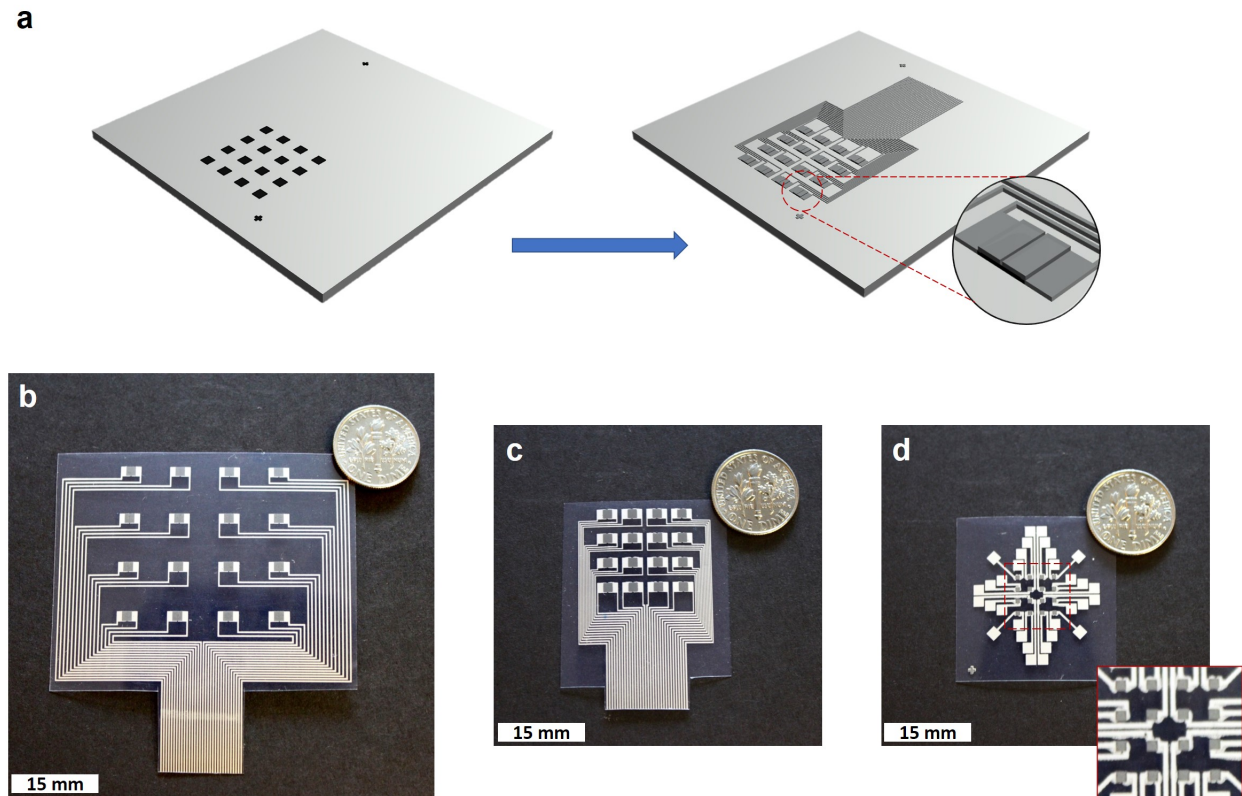
Figure 2.2: **Fabrication schematic and various printed array dimensions. (a)** Fabrication steps for fully-screen printed thermistor array. A layer of NiO is first deposited on a PEN substrate using screen printing, after which conductive silver pads and traces are printed directly on top. The inset image shows a magnified view of an individual thermistor pixel stack. **(b-d)** Various thermistor densities can be achieved by modifying the screen design, a dime is shown for scale. The inset image shows a magnified view of NiO pads for the smallest array design, which have dimensions of 900μm x 900μm.
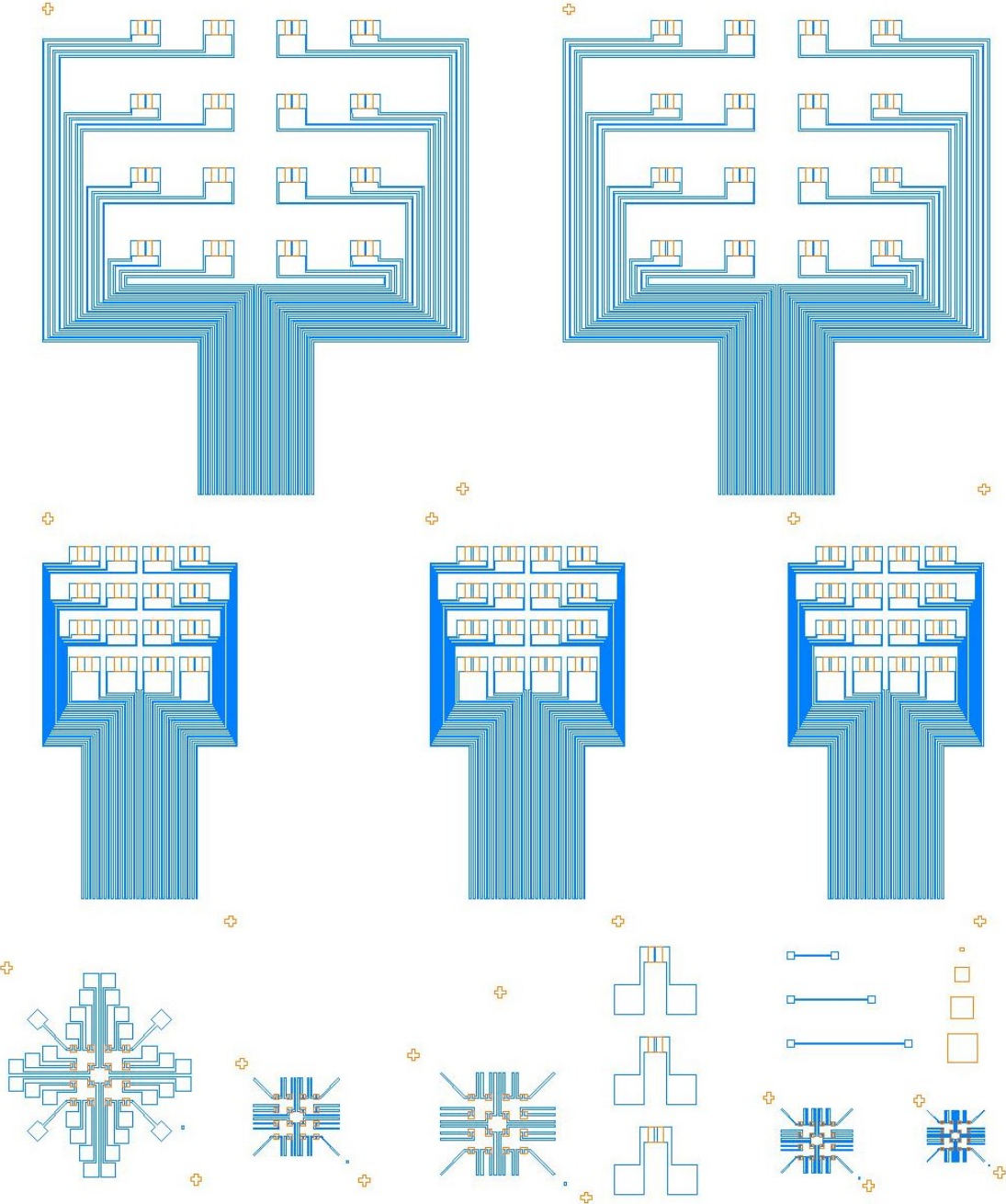
Figure 2.3: **Screen layout for thermistors, arrays, and test structures.**
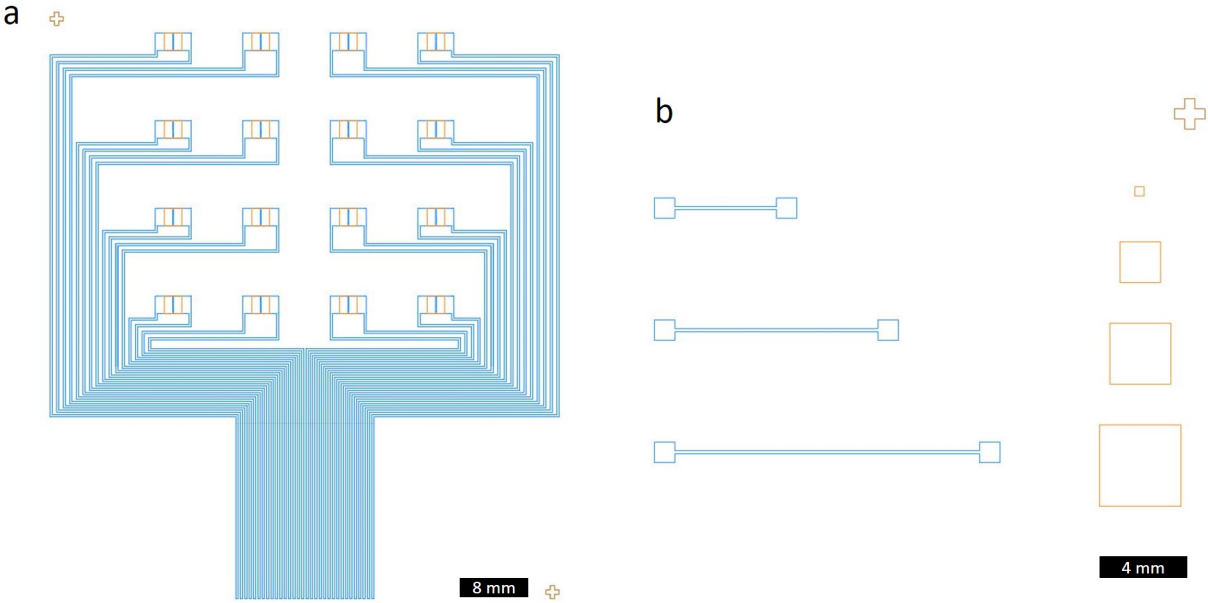
Figure 2.4: **Close-up of critical screen design elements. (a)** Layout of thermistor array with large pixel spacing. **(b)** Layout of test structures for print quality evaluation.
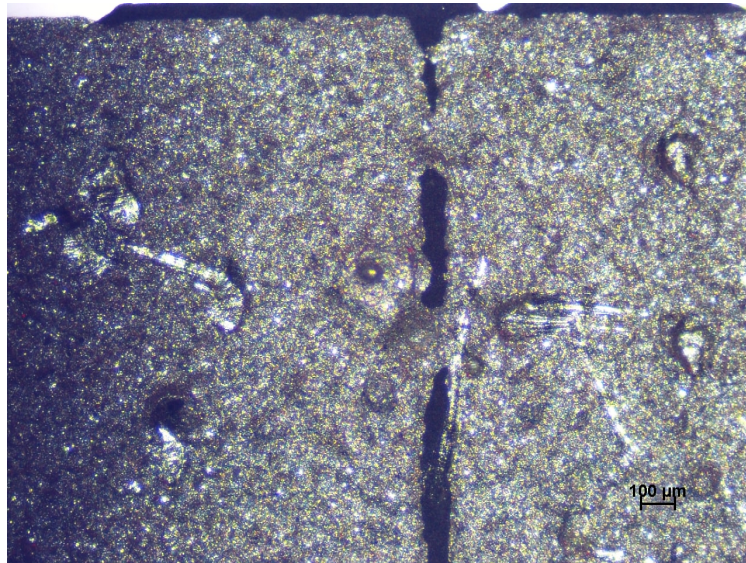
Figure 2.5: **Micrograph image of shorted printed silver electrodes on top of printed NiO film.** The scale bar represents 100 μm.
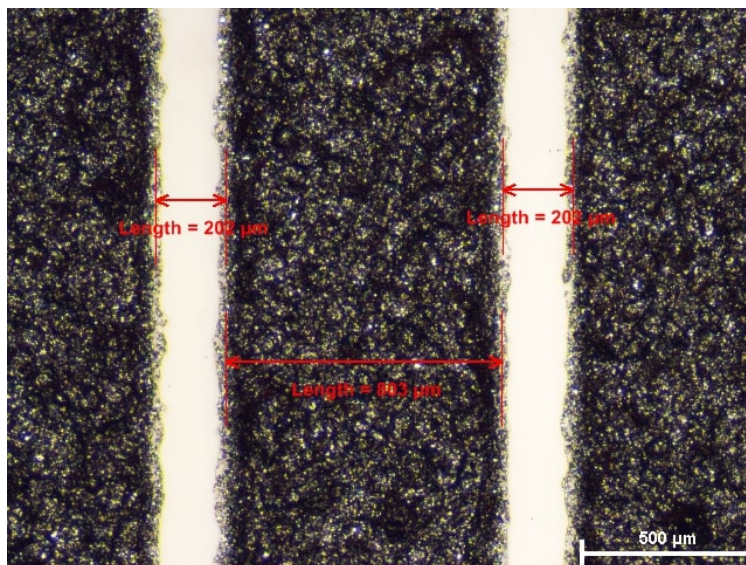
Figure 2.6: **Micrograph image of printed silver FFC connector.** The screen design dimensions are for a 750 μm pad width and a 250 μm spacing. The scale bar represents 500 μm.

2.4   NiO film optimization

2.4.1   Ink deposition and characterization

The thermistors were screen-printed, using an ASYS APM101 screen printer, onto a 120 μm thick polyethylene naphthalate (PEN) substrate. The thermistor first layer is consisted of a nickel oxide (NiO) nanoparticle ink with different weight ratio of NiO (nickel(II) oxide nanopowder, < 50 nm from Sigma-Aldrich), PSBR (Targray Technology), and deionized (DI) water. The mixture was then screen printed onto PEN substrates and then was cured for 12 hours at 140 °C in vacuum. To complete the thermistors, a silver electrode layer was screen printed on top of the NiO layer using a silver micro-flake ink, with flake size of 7 mm, purchased from Creative Materials (118-09A/B). The metal layer was annealed at 110 °C for 15 minutes after deposition. The thermistor layers thicknesses were measured with a Dektak profilometer. The temperature response of the thermistors was characterized on top of a custom-made hotplate by using a Keithley 2400 SourceMeter. SEM images were acquired with a Hitachi TM-1000 SEM. The ink viscosity was measured with a Brookfield DV3T viscometer.

2.4.2   NiO ink viscosity

There are three critical parameters when formulating screen printable inks: the ratio of the solid content, the particle size distribution, and the viscosity. The latter is related to the molecular attraction within the liquid and is the ratio of the shear rate of the fluid to the shear stress. The ink must have thixotropic characteristics, in which the shear rate/shear stress ratio is nonlinear. As the shear rate (which is the combination of the squeegee pressure, velocity, and screen tension) is increased, the ink becomes substantially thinner, causing it to flow readily. We tested different ink compositions whereas the amount of water and PSBR were varied: 6:2:1, 6:2:2, 6:1.5:2 and 6:1:2 (NiO:PSBR:H_2O). Figure 2.7a shows the viscosity of each tested ink as a function of shear rate. For inks with 6:2:1 composition, the viscosity reduces significantly as the shear rate increases from 25000 to 75000 cP. During the screen-printing process, while force is being applied by the squeegee (high shear rate), the ink viscosity must be low, causing the ink to flow readily so that it is transferred completely from the screen to the substrate. After the squeegee has passed (low shear rate) and the ink is on the substrate, the viscosity should be higher so that the ink will not flow, maintaining the definition of the pattern. This behavior was not observed for the ink compositions of 6:2:2, 6:1.5:2 and 6:1:2, whereas the viscosity change is low (from 5000 to 3500 cP) as the shear rate increases. Figures 2.7b-d indicate the correlation of ink viscosity with printing quality. As indicated in Figure 2.7b, using the 6:2:1 ink composition resulted in printed features with good shape definition and homogenously coated 2 x 2 mm film. For the 6:2:2 ink when the water content was doubled, the printed feature has poor feature definition, spreading ink along the edges and leaving pinholes on the film surface (Figure 2.7c). Poor film quality was also observed for the 6:1.5:2 and 6:1:2 compositions (Figures 2.7d and e).
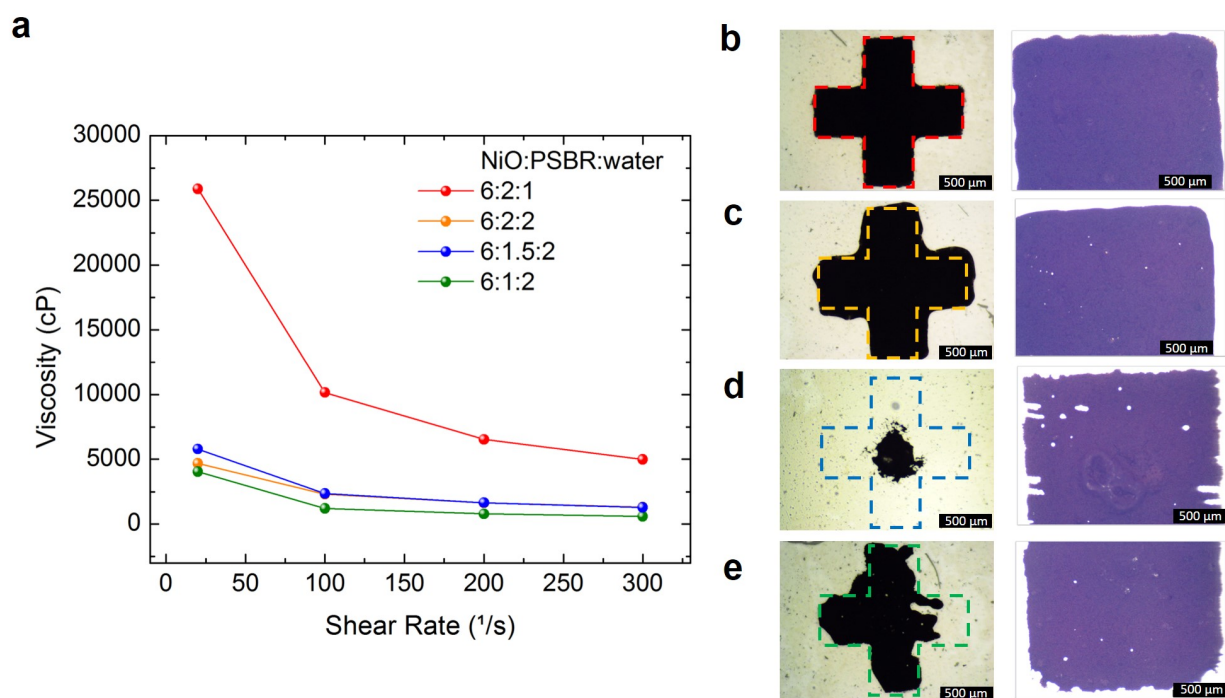
Figure 2.7: **Ink viscosity optimization for NiO ink and printed films.** **(a)** Ink viscosity obtained with a spindle rheometer and optical images of printed features for each ink compositions (NiO:PSBR:water): **(b)** 6:2:1, **(c)** 6:2:2, **(d)** 6:1.5:2 and **(e)** 6:1:2. The scale bars in the micrographs represent 500 μm. Printed features with higher quality was obtained for the 6:2:1 composition whereas the viscosity decreases with increasing shear rate. Ink viscosity of 6:2:2, 6:1.5:2 and 6:1:2 compositions is not significantly reduced when shear rate is higher and resulted in printed features with poor quality.
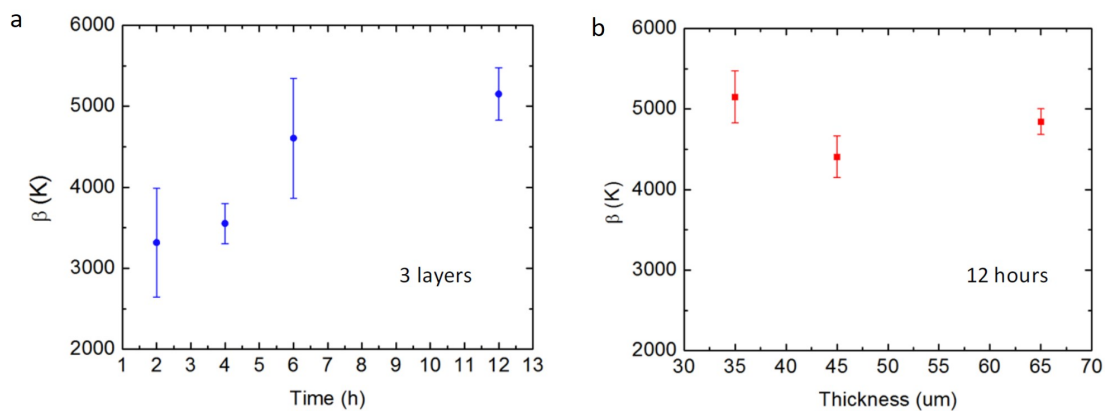
Figure 2.8: **Measured thermistor β as a function of annealing time and number of printed layers. (a)** Measured thermistor β as a function of film annealing time for printed NiO films with 3 layers. **(b)** Measured thermistor β as a function of printed NiO film thickness. 1 layer (35 μm), 2 layers (45 μm), and 3 layers (65 μm) are plotted.
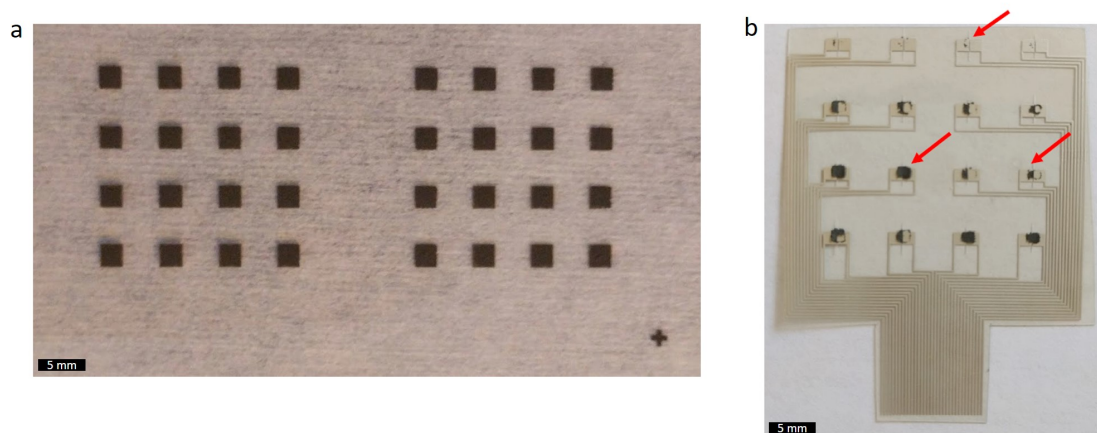
Figure 2.9: **Printed NiO film defects on printed silver electrodes. (a)** Printed 6:2:1 NiO ink on bare PEN. **(b)** Printed 6:2:1 NiO ink on printed silver electrodes. Low yield of electrodes is achieved due to many missing printed NiO films.
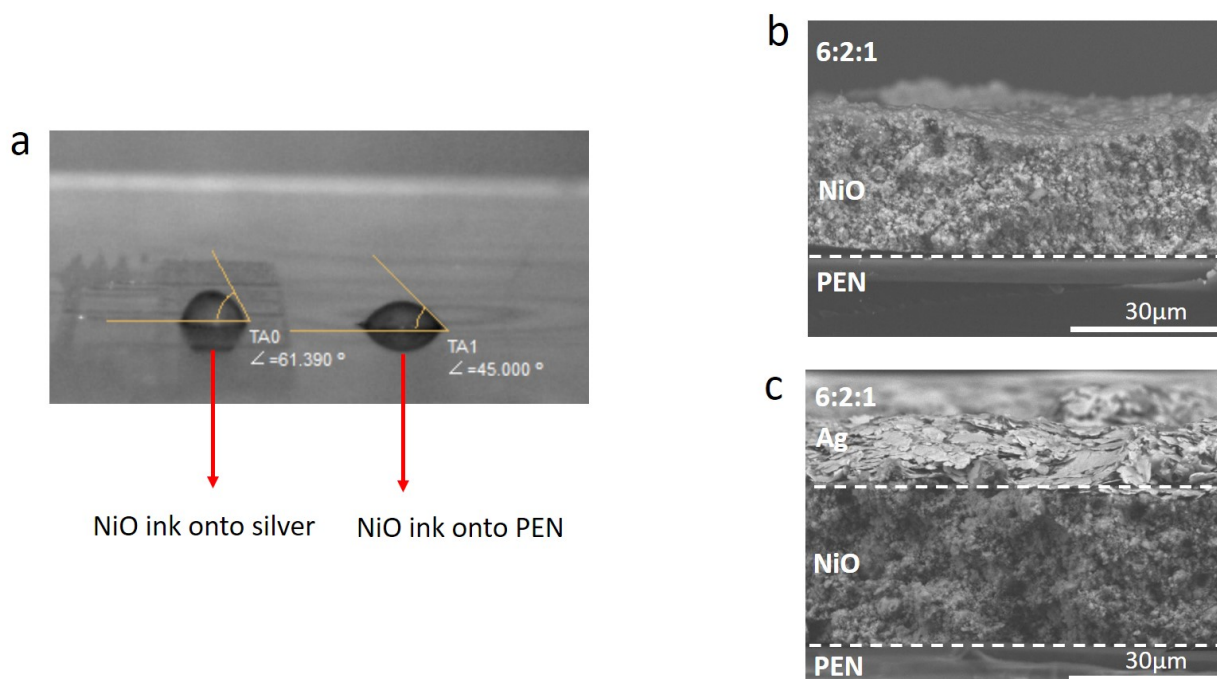
Figure 2.10: **Contact angle measurement of NiO ink and cross sectional film micrograph images.** **(a)** Contact angle measurement of 6:2:1 NiO ink drop casted on printed silver and on PEN substrate. **(b)** SEM cross sectional image of 6:2:1 NiO ink printed on PEN. **(c)** SEM cross sectional image of 6:2:1 NiO ink printed on PEN, with printed silver on top. The scale bar represents 30 μm.

2.4.3 Drying time and film thickness

Figure 2.8a shows a plot of measured β as a function of annealing time for a NiO film with 3 printed layers. We can see that a longer anneal time tends to yield a higher β device, with closer grouping between devices. Specifically, we chose to use the devices annealed for 12 hours at 140 °C. In Figure 2.8b, we see a plot of measured β as a function of NiO film thickness. By varying the number of print passes for the NiO film, we can tune the thickness of the film. We see that the devices with the closest grouping when annealed for 12 hours was the 5 layer thick (65 μm) NiO films. However, each print pass requires a cleaning and realignment, and becomes very time consuming. As such, we selected to move forward with the middle ground, the 3 layer (45 μm) NiO films.

2.4.4   Layer orientation

As noted from Figure 2.2, the fabrication process of the thermistor arrays involves first depositing the NiO film before depositing the silver electrodes. This configuration is inverted from the conventional NiO thermistor configuration due to the interaction between the NiO ink developed (6:2:1 ratio) and the printed silver electrodes. Figure 2.9a shows the 6:2:1 NiO directly printed on the PEN substrate. However, when moving to printing the NiO films onto the printed silver electrodes, we can see from Figure 2.9b that there are some major print defects in the NiO film. Notably, there are several pixels that have incomplete NiO films, as well as many electrode pairs that are completely missing a NiO layer. Our suspicion was that the NiO film was delaminating from the silver electrodes during the screen printing process and adhering to the backside of the screen as the squeegee passes over. To confirm our suspicions, Figure 2.10a shows a contact angle measurement of a drop casted NiO ink on top of a printed silver electrode. It can be seen that the NiO ink drop casted onto the silver directly has a contact angle of 61.39 °, whereas the NiO ink drop casted onto the PEN substrate itself has a contact angle of 45 °. We then tried the inverted configuration and deposited the NiO film directly onto the PEN before printing the silver electrodes on top of it. Figures 2.10b and c show the SEM cross sectional image of a thermistor pixel at each fabrication step. The NiO directly fabricated on the PEN substrate has a rough thickness of 20 μm with good cross sectional uniformity, and the silver fabricated on top has a thickness of 10 μm. From this analysis, we concluded the inverted pixel structure was optimal.

2.5   Temperature mapping

2.5.1   Sensor characterization

Figure 2.11a shows the photograph of the thermistor array that was fabricated by screen printing the 6:2:1 ink composition. Two 2 x 2 mm silver pads with 140 μm gap distance and 10 μm thick were printed on top of each 2 x 2 mm nickel oxide pads with thickness of 30 μm. The resistance versus temperature characterization is illustrated on Figure 2.11b. As indicated by Figure 2.11b, the resistance of the thermistor decreases with temperature increase, hence, the sensors exhibit NTC behavior. All 16 pixels of the array present similar values of resistance for each temperature, indicating good reproducibility of the pixels within the array at 25 °C. The β, the slope of the graph in Figure 2.11c, is a measure of the temperature sensitivity and higher values result in greater change in resistance with temperature change. For the array fabricated in Figure 2.11a, we obtained an average $\beta = 4302 \pm 401$ K which is comparable with previous reported values for a single pixel NiO thermistor fabricated by ink-jet and stencil printing. The thermistor change in the resistance is given by the following equation:

$$R_t = R_0 \exp \beta (\frac{1}{T} - \frac{1}{T_0}) \tag{2.1}$$

R_t is the resistance at temperature T, R_0 is the resistance at the reference temperature T_0 and β is the material constant for the thermistor and can be calculated by rearranging Equation (2.1):

$$\ln R_t = \ln R_0 + \beta(\frac{1}{T} - \frac{1}{T_0}) \tag{2.2}$$

β represents the slope of the $\ln R_t$ versus $1/T$ plot, which is related to the Boltzmann relation (E/kT), where E is the bandgap of the thermistor material and k is the Boltzmann's constant. By differentiating Equation (2.1) with respect to T and dividing by R_t, it is possible to obtain the temperature coefficient of the thermistor α, which represents the percentage change in resistance per degree Kelvin.

$$\alpha = \frac{1}{R_t}\frac{dR_t}{dT} = \frac{\beta}{T^2}(\%K^{-1}) \tag{2.3}$$

For calibrating the thermistor array, we probed resistance values for different temperature for each pixel and calculated β using Equation (2.2). These β are used in Equation (2.1) for calculating the temperatures from the thermistor resistances, which are read from a voltage divider network composed of the thermistor in series with a 660 kΩ resistor (R). The variable voltage from the thermistor (V_t) is recorded and can be related to the thermistor resistance (R_t) by Equation (2.4), where V_b is the bias voltage.

$$V_t = V_b \times \frac{R}{(R_t + R)} \tag{2.4}$$

The resistance of the thermistor at a given temperature also depends on the geometry of the electrodes. Figure 2.11d shows resistance values at 25 °C for the 2 x 2 mm silver electrode pads with distance gap of 75, 175 and 285 μm, which resulted in the exponential increase of 4 to 9 MΩ.

The thermistor array was designed such that each individual thermistor pixel could be individually addressed. By addressing each individual pixel, we can spatially map the temperature of a surface using the fabricated thermistor array. 2.12 demonstrates the temperature map acquired when the first column of pixels is touched by a finger. The temperature rises from 25 °C to 33 °C as a finger is placed on the thermistor pads. (Figure 2.12a and 2.12c). As it is shown on Figure 2.12a and 2.12c, the thermistor array is capable of resolving local heating in areas as small as one-pixel dimension.
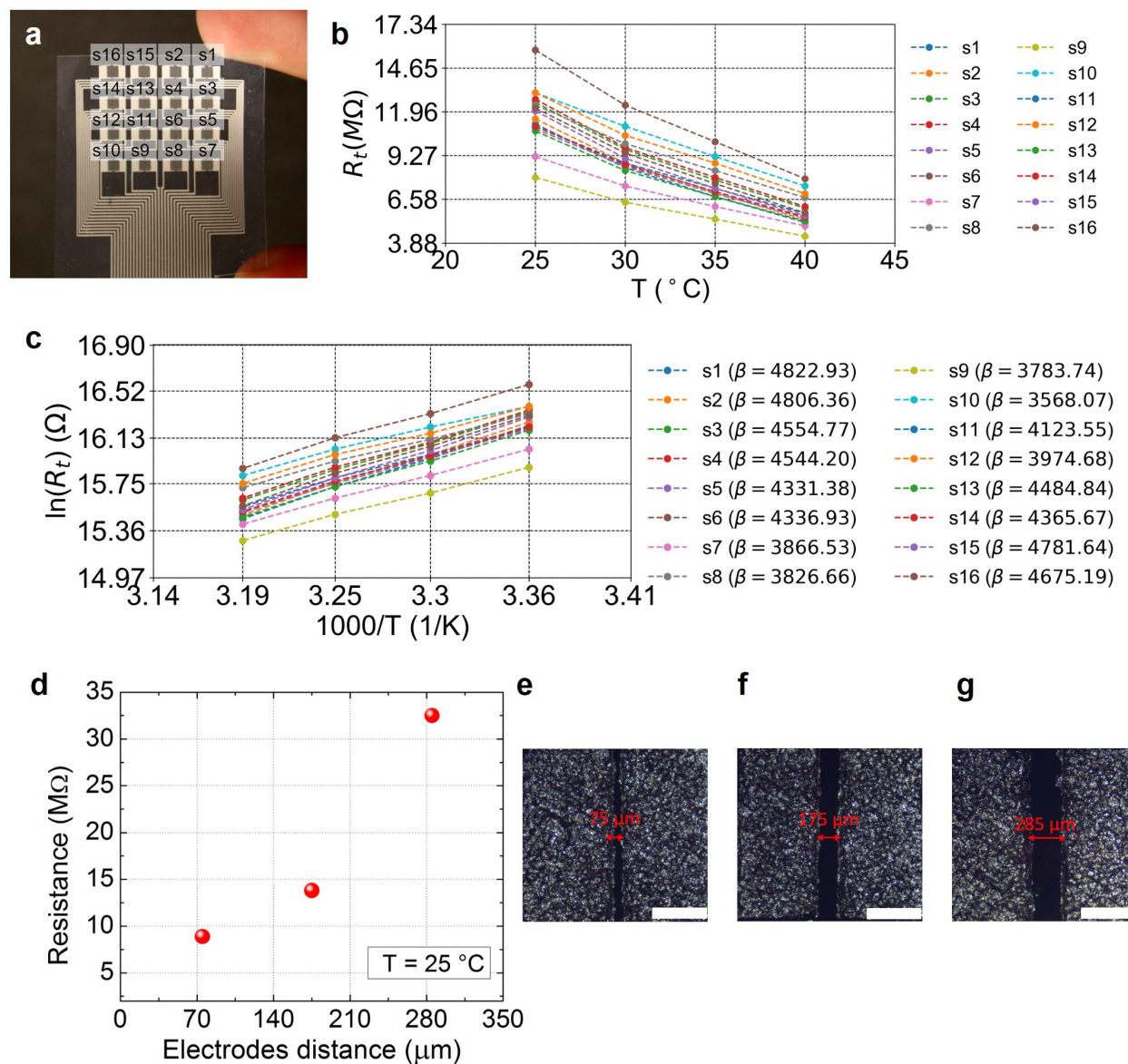
Figure 2.11: **Resistance characterization of the various thermistor pixels.** **(a)** Photograph of the 16 pixels thermistor array with each corresponding pixel number. **(b)** Resistance versus temperature plot for each pixel in the array and **(c)** β plot of each pixel. **(d)** Resistance versus silver electrode gap distance. **(e)**, **(f)**, and **(g)** micrographs of the silver electrode gap for 75, 175 and 285 μm, respectively. The scale bars represent 500 μm.
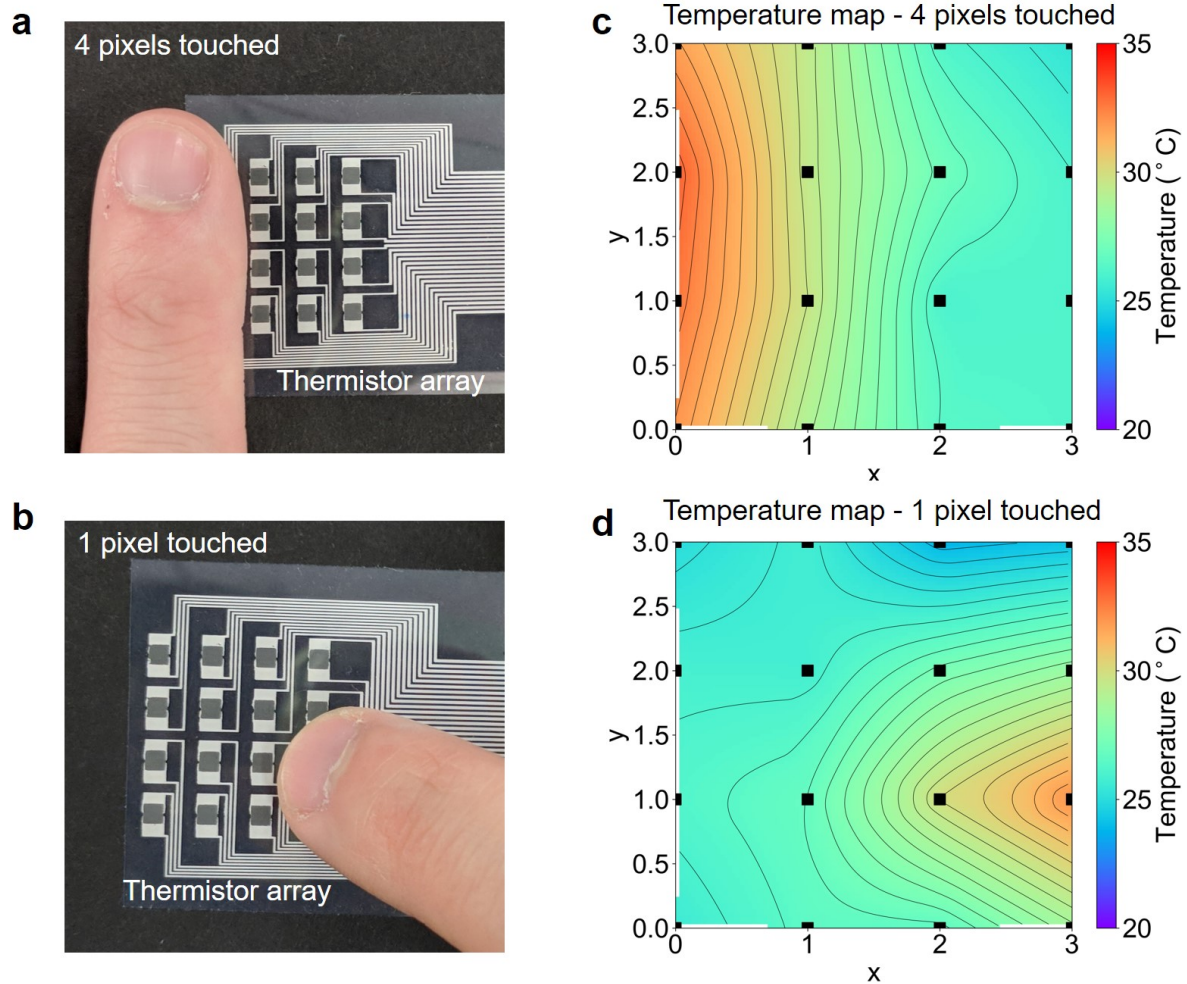
Figure 2.12: **Temperature mapping capability of the printed thermistor arrays.** **(a)** Photograph of index finger placed over 4 pixels of the thermistor array and **(b)** corresponding temperature map. When touched, the temperature rises from 25 °C to 33 °C. **(b)** Photograph of index finger placed over a single pixel of the thermistor array and **(d)** corresponding temperature map.

2.5.2 Battery temperature characterization

With the fabricated thermistor arrays, we monitored battery surface temperature in real-time with an experimental setup that varied battery discharge rate. C-rate is one way of describing a batteries discharge rate. A 1C rate corresponds to a discharge current that will completely discharge the battery in 1-hour. For a battery capacity of 200 Amp-hours, a 1C discharge current would be 200 Amps, a 2C rate would be 400 Amps, and a 0.5C rate would be 100 Amps. For real-time temperature monitoring, the thermistor data was obtained using a voltage divider network, where the variable voltage across an individual thermistor pixel is recorded using an ADC, and then individual pixels are selected using a multiplexor. The measured values are then sent to a laptop via USB for collection and processing. The printed thermistor array is connected to the board and placed on top of a commercially available lithium-ion battery, connected to power resistors of various values such that the battery discharge rate would be 0.5, 2, or 3C. A schematic view of the setup can be found in Figure 2.13a-b. In Figure 2.13c-e, the values collected from the thermistor array are plotted over time, with the red regions depicting when the battery was discharging, and the green regions depicting when the battery was disconnected. Depending on the discharge rate selected, different discharge profiles were used as to not heat the battery in a dangerous way. The peak temperatures of the battery were confirmed using a thermal imaging camera, which is plotted as red dots superimposed over the thermistor array data.

For the 0.5C discharge rate, the battery is connected to the power resistor for 6 minutes continuously. Because this is a very low discharge rate, almost no temperature change is observed, which can be observed in Figure 2.13c. There is a slight monotonic increase in temperature over the 6 minutes window, but the temperature change is no more than 2 °C. For the 2C discharge rate in Figure 2.13d, the battery was connected to the power resistor for 3 minutes, and then disconnected for the remaining 3 minutes. Here, we observe a significant increase in temperature during the time when the battery is discharging. Again, there is a monotonic increase in temperature, this time from around 23 °C to a peak of about 45 °C. When the battery is disconnected, it begins to cool and the temperature gradually decreases until around 33 °C at 6 minutes. For the 3C discharge rate in 2.13e, the battery was connected to the power resistor for 1 minute, and then disconnected for 1 minute. This was repeated two more times over the 6 minute experiment duration. Similar to the 2C experiment, we observe that the battery temperature increases linearly when it is discharging, and cools slightly when it is disconnected. However, because the rate at which the battery heats up is higher than its cooling rate, we observe that over the three charging and discharging cycles, the peak battery temperature continues to increase. This is depicted in 2.13f-g, where a snapshot from the thermal imaging camera and the thermistor temperature plot are plotted side-by-side at 60 seconds, and at 300 seconds respectively. The peak temperature the battery reached at 60 seconds was around 35 °C and around 46 °C at 300 seconds.
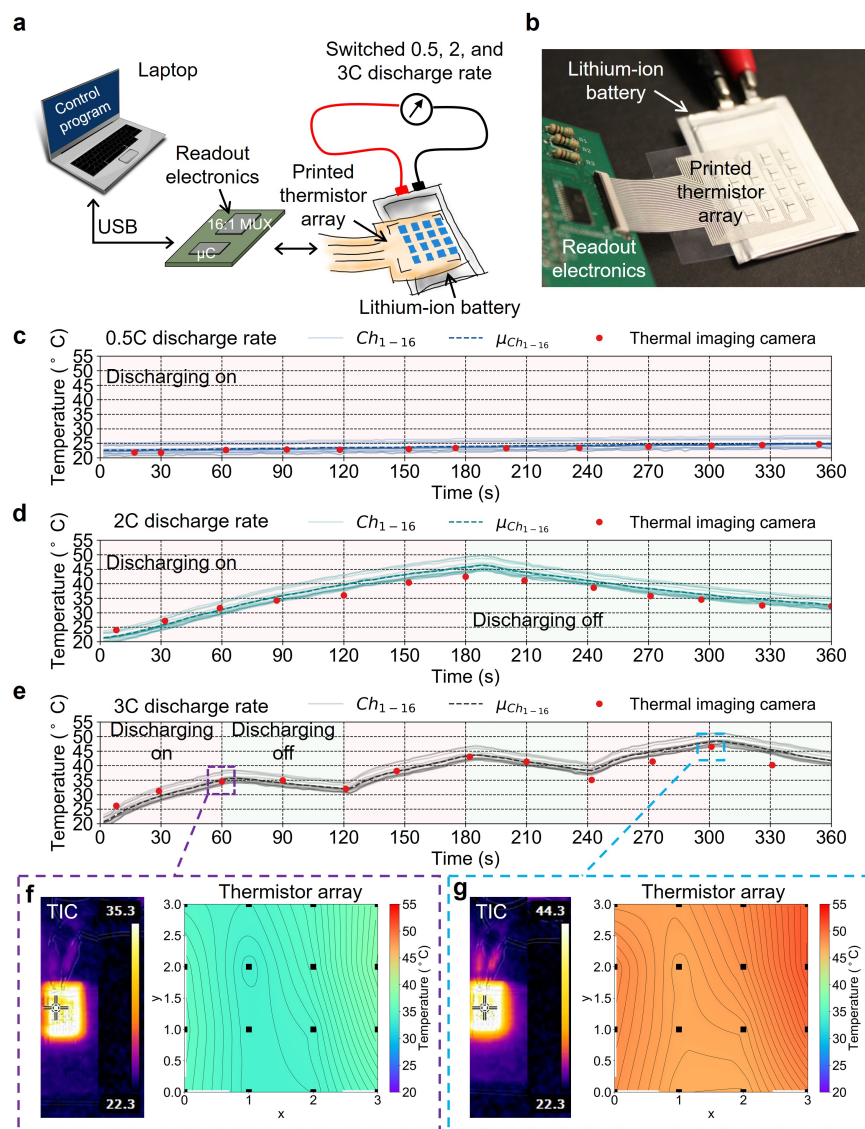
Figure 2.13: **Battery temperature monitoring characterization.** **(a)** Schematic of battery monitoring setup. (b) Optical image of thermistor array connected to readout electronics and placed on top of Lithium-ion battery. **(c-e)** Temperatures recorded from 16 channels of the array are plotted over 6 minutes. The discharge rate is set to 0.5C, 2C, and 3C, and the discharge profiles are different for each rate. The red regions depict when the battery is connected to the resistor and discharging, and the green regions depict when the battery is disconnected. A thermal camera was used to verify the temperatures recorded by the array, and is plotted as red dots. **(f,g)** The left image was captured using the thermal camera from the top view of the battery and the right image is the temperature map captured by the thermistor array, at 60 and 300 seconds.

2.6   Chapter conclusions

In conclusion, in this chapter, we have demonstrated a 4 x 4 array of fully screen-printed thermistors based on a custom NiO ink, printed on a flexible substrate. NiO inks of various viscosities were created and characterized to optimize the print quality of the NiO films, as well as their feature definition. By utilizing an array of devices, as well as a microcontroller to interface with the printed sensors, real time temperature monitoring was demonstrated. As a system level implementation, the printed sensor array was tested on commercially available Lithium ion batteries to observe and quantify battery heating as they were discharged at various C-rates. The temperature maps were confirmed using a thermal camera and on average had an error of 5 %. We believe that this fully screen-printed thermistor arrays will motivate more research on these printed sensors and will contribute with useful insight for future works. This demonstration of printed thermistor arrays will help stretch the applications of these sensors beyond conventional sensing regimes, such that benefits of low-cost fully printed thermistors can be effectively used.

2.7 References

[1] Jonathan K Ting, Natasha A D Yamamoto, Yasser Khan, Abhinav Gaikwad, and C Ana. Fully Screen-Printed Thermistor Array for Battery Health Monitoring.

[2] Yasser Khan, Mohit Garg, Qiong Gui, Mark Schadt, Abhinav Gaikwad, Donggeon Han, Natasha A.D. Yamamoto, Paul Hart, Robert Welte, William Wilson, Steve Czarnecki, Mark Poliks, Zhanpeng Jin, Kanad Ghose, Frank Egitto, James Turner, and Ana C. Arias. Flexible Hybrid Electronics: Direct Interfacing of Soft and Hard Electronics for Wearable Health Monitoring. *Advanced Functional Materials*, 26(47):8764–8775, 2016.

[3] A. Aliane, V. Fischer, M. Galliari, L. Tournon, R. Gwoziecki, C. Serbutoviez, I. Chartier, and R. Coppard. Enhanced printed temperature sensors on flexible substrate. *Microelectronics Journal*, 45(12):1621–1626, 2014.

[4] Chia Wang, Guan Yi Hong, Kuan Ming Li, and Hong Tsu Young. A miniaturized nickel oxide thermistor via aerosol jet technology. *Sensors (Switzerland)*, 17(11), 2017.

[5] J. Courbat, Y. B. Kim, D. Briand, and N. F. De Rooij. Inkjet printing on paper for the realization of humidity and temperature sensors. *2011 16th International Solid-State Sensors, Actuators and Microsystems Conference, TRANSDUCERS'11*, pages 1356–1359, 2011.

[6] Anurag Ganguli, Bhaskar Saha, Ajay Raghavan, Peter Kiesel, Kyle Arakaki, Andreas Schuh, Julian Schwartz, Alex Hegyi, Lars Wilko Sommer, Alexander Lochbaum, Saroj Sahu, and Mohamed Alamgir. Embedded fiber-optic sensing for accurate internal monitoring of cell state in advanced battery management systems part 2: Internal cell signals and utility for state estimation. *Journal of Power Sources*, 341:474–482, 2017.

[7] Shingo Harada, Wataru Honda, Takayuki Arie, Seiji Akita, and Kuniharu Takei. Fully printed, highly sensitive multifunctional artificial electronic whisker arrays integrated with strain and temperature sensors. *ACS Nano*, 8(4):3921–3927, 2014.

[8] A. G. Hsieh, S. Bhadra, B. J. Hertzberg, P. J. Gjeltema, A. Goy, J. W. Fleischer, and D. A. Steingart. Electrochemical-acoustic time of flight: In operando correlation of physical dynamics with battery charge and health. *Energy and Environmental Science*, 8(5):1569–1577, 2015.

[9] Chun Chih Huang, Zhen Kai Kao, and Ying Chih Liao. Flexible miniaturized nickel oxide thermistor arrays via inkjet printing technology. *ACS Applied Materials and Interfaces*, 5(24):12954–12959, 2013.

[10] S. A. Kanade and Vijaya Puri. Composition dependent resistivity of thick film Ni(1-x)Co xMn2O4: ($0 \le x \le 1$) NTC thermistors. *Materials Letters*, 60(11):1428–1431, 2006.

[11] De Kong, Linh T. Le, Yue Li, James L. Zunino, and Woo Lee. Temperature-dependent electrical properties of graphene inkjet-printed on flexible materials. *Langmuir*, 28(37):13467–13472, 2012.

[12] Zhe Li, Jianbo Zhang, Bin Wu, Jun Huang, Zhihua Nie, Ying Sun, Fuqiang An, and Ningning Wu. Examining temporal and spatial variations of internal temperature in large-format laminated battery with embedded thermocouples. *Journal of Power Sources*, 241:536–553, 2013.

[13] Madhu Santosh K. Mutyala, Jingzhou Zhao, Jianyang Li, Hongen Pan, Chris Yuan, and Xiaochun Li. In-situ temperature measurement in lithium ion battery by transferable flexible thin film thermocouples. *Journal of Power Sources*, 260:43–49, 2014.

[14] Susana Novais, Micael Nascimento, Lorenzo Grande, Maria Fátima Domingues, Paulo Antunes, Nélia Alberto, Cátia Leitão, Ricardo Oliveira, Stephan Koch, Guk Tae Kim, Stefano Passerini, and João Pinto. Internal and external temperature monitoring of a li-ion battery with fiber bragg grating sensors. *Sensors (Switzerland)*, 16(9):1–9, 2016.

[15] R. Schmidt, A. Basu, and A. W. Brinkman. Production of NTCR thermistor devices based on NiMn2O4+δ. *Journal of the European Ceramic Society*, 24(6):1233–1236, 2004.

[16] Tiina Vuorinen, Juha Niittynen, Timo Kankkunen, Thomas M. Kraft, and Matti Mäntysalo. Inkjet-printed graphene/PEDOT:PSS temperature sensors on a skin-conformable polyurethane substrate. *Scientific Reports*, 6(September):1–8, 2016.

Chapter 3

Printed optoelectronics

3.1 Introduction

In this chapter we will discuss one example of "active" sensors, a reflection oximeter. Specifically, using printed optoelectronics, we can combined organic light emitting diodes (OLEDs) and organic photodiodes (OPDs) and use it as a reflection mode sensor. In particular, OLEDs have been primarily used in the display industry as well as area lighting applications, however here I will discuss how OLEDs have applications in the sensor realm. First, I will discuss my work on OLED characterization, and how a custom luminance characterization setup was developed. From there, I will dive into the multi-channel reflection oximeter work and discuss the fabrication of the devices, as well as the various studies we designed to determine optimal device placement, device geometry, and sensor redundancy. Portions of this chapter are published in [1].

3.2 OLED characterization

3.2.1 Performance metrics

There are a variety of key performance metrics to characterize the OLEDs we fabricate. Here we will loosely introduce some of those paramaters and their relevant equations [2]. It should be noted that many metrics have both a radiometric and photometric equivalent. The latter is specifically concerned with the measurement of light as perceived by the human eye.

The radiant flux Φ is defined as the rate of change of radiant energy with respect to time. Radiant flux has units of Watts and is defined as:

$$\Phi = \frac{dQ}{dt} \tag{3.1}$$

Irradiance E is defined as the radiant flux per unit area emerging from a point in a given

surface. It is defined as:

$$E = \frac{d\Phi}{ds_0} \tag{3.2}$$

where ds_0 is defined as the surface area element on the surface of interest. Irradiance has the units of Wm^{-2}.

Radiance is a measurement of area and solid angle density for radiant flux, and is recorded in units of $\mathrm{Wm}^{-2}\mathrm{sr}^{-1}$. Generally it can be explained as the amount of radiant flux per unit area, per unit solid angle emerging from a point on the surface of interest. It is defined as

$$L = \frac{d^2\Phi}{d\omega ds} \tag{3.3}$$

where ω is defined as the solid angle in a specific direction and s is the projected area onto the surface containing the point of interest. It should be noted that irradiance has both the initial surface, source point, and the direction that the measurement is taken.

For most OLED applications, the human eye is used as the detector in the system. As such, the optical performance of OLEDs in this particular application space requires the definition of how the human eye behaves and receives various forms of light. This particular analysis is defined as photometry. Detecting light itself through the eye is a very complex process. Light enters the eye and is transmitted through a variety of optics before being received by the retina. The retina itself has two different types of receptors, split into rods and cones. Even within rods and cones, there are further degrees of classification [2]. From the light absorbed in these receptors, the light is converted into a series of electrochemical signals sent to the brain via the optic nerve. It is understood that rods are used for low light vision, known as scotopic vision, and cones are used for ambient light vision, known as photopic vision, and are how we perceive various colors. There are different types of cones responsible for a variety of wavelengths, loosely split into short, medium, and long cones. From Figure 3.1, we can see the photopic response of the human eye defined as $V(\lambda)$. Note that this particular spectrum is more green cenetered, around the 500-600 nm wavelength regime. This has to do with the aforementioned short, medium, and long cones and how they overlap in their absorption spectra. We happen to have more cones that absorb and overlap in absorption in this region, and as such human vision is green-weighted.

From our previous introduction of radiance, the photometric equivelant is defined as luminance, L_v. The units of this measurement are $\mathrm{lm\ m}^{-2}\mathrm{sr}^{-1}$, alternatively $\mathrm{cd/m}^2$ or nits. This is conceptually the human perception of brightness in photometry, where as radiometric radiance is the quantitative value of brightness. It can be computed as follows:

$$L_v = 683[\frac{lm}{W}] \int_{380}^{770} L(\lambda)V(\lambda)d\lambda \tag{3.4}$$

As part of the luminance calculation for OLEDs, the responsivity of the detector used for the measurement, as well as the spectral emission pattern of the OLEDs are required. The other plots $R(\lambda)$ and $S(\lambda)$ in Figure 3.1 are examples of what this may look like.

External quantum efficiency (EQE) conceptually is defined as the ratio of number of photons emitted by a device to the number of electrons injected into the device. Note that this does not specifically mean the number of electrons injected into the emission layer of the device, specifically this is the injection of electrons at the electrode [2]. The EQE can be defined as

$$\eta = \frac{n_{ph}}{n_e} \times 100\% \tag{3.5}$$

where n_{ph} is the total number of photons emitted from the device and n_e is the total number of electrons injected into the device. It should be noted that light emitted directly horizontal and at angles greater than 180 degrees are not included in this calculation and be considered as not relevant for emitted light, as they are waveguided into the substrate.

An additional parameter that is frequently reported is the current efficacy of the device, η_I. The current density measurement has units of cd/A and is defined as

$$\eta_I = 0.1\frac{L_v}{J} \tag{3.6}$$

where J is the current density of the device under test, measured in units of mA/cm^2. This measurement is particularly useful in the display industry, as knowing the amount of luminance, or perceived brightness, a certain amount of current can provide is important to circuit designers for display controllers. In addition, radiance isn't used as perceived brightness by the human eye matters more than total energy radiated.

The luminous efficacy of radiation is a parameter that tells us how effictive a beam of light is at stimulating the human eye response, with units of lm/W. First, by defining the luminous flux Φ_v (the radiant flux weighted by the photopic response):

$$\Phi_v = 683[\frac{lm}{W}] \int_{380}^{770} \Phi(\lambda)V(\lambda)d\lambda \tag{3.7}$$

The luminous flux is defined in units of lumen (lm). From there, the luminous efficacy of radiation, K_r can be defined as this ratio between luminous flux and radiant flux, or mathematically noted as:

$$K_r = \frac{\Phi_v}{\Phi} \tag{3.8}$$

Finally, the power efficacy of a device measures the luminous flux produced by a light source at given input power. It is recorded in units of lm/W and expressed as:

$$K_s = \frac{\Phi_v}{P} \tag{3.9}$$

where P is the electrical power inputted to the source in units of Watts.
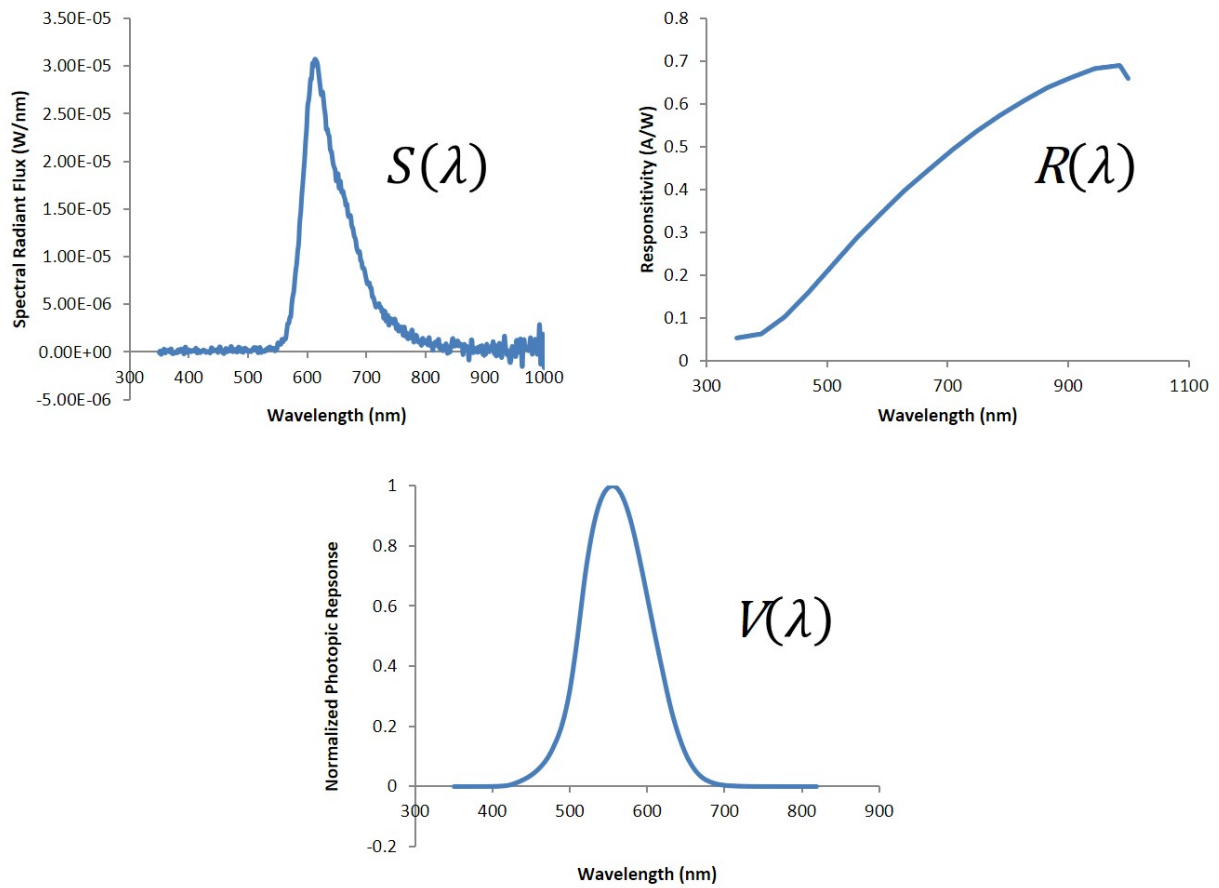
Figure 3.1: **Spectral response of OLED, photodiode responsivity, and human photopic response.**

3.2.2   Custom photodiode setup

As part of the OLED characterization, two measurements are frequently performed. Current vs. Luminance, and Luminance vs. Voltage characteristics are typically aquired using a commercial luminance setup, however for the characterization of our devices, we built a custom photodiode measurement setup [2]. In conjunction with an integrating sphere, a custom built setup consisting of several equipments connected to a computer running control software (LabVIEW) can perform the J-V-L (current density-voltage-luminace) characterization. A schematic of the custom setup is shown in Figure 3.2. The OLEDs are placed in an OLED holder, allow for individual wires connecting to up to eight cathodes and one anode to be addressed. The OLEDs are driven by a Keithley 2601A sourcemeter, and the J-V can be measured directly from this sourcemeter. Separated by a 21.4 cm distance, a commercial silicon photodide (PDB-C609) is placed on a goniometer. This allows the photodiode to be precisely aligned at various angles to the incoming OLED light. The photodiode generates photodiode current based on the incident OLED light, and the photocurrent is measured by the Keithley 2400 sourcemeter, synchronized in time to the OLED driver. Using LabVIEW, this setup can precisely record and time the data for both the J-V, and the photocurrent of the photodiode. A photo of the setup is shown in Figure 3.3. From Figure 3.4, we can see the LabVIEW software interface for controlling the J-V-L setup. The sweep to and from voltages can be defined, and the delay between applying the voltage to the OLED can also be defined. On the right, both the J-V, and the V-L plots are displayed in real time.

In addition to this particular setup, the goniometer on the bottom of the OLED mount can allow for interesting emission angle measurements. In general, most fabricated OLEDs are considered Lambertian emitters, meaning they follow a cosine angle rule regarding the angle of emission and intensity. To validate that, the LabVIEW software can be adapted to measure the photodiode current when applying a constant voltage to the OLED at various angles. In Figure 3.5, we can see the LabVIEW control software for the setup. At each inputted angle, the user can be prompted to turn on the OLED through the software, and the photodiode current is recorded. An example plot of several different OLEDs measured from 0-180 °emission angles is shown in Figure 3.6. As mentioned earlier, it is expected they have similar emission behavior.
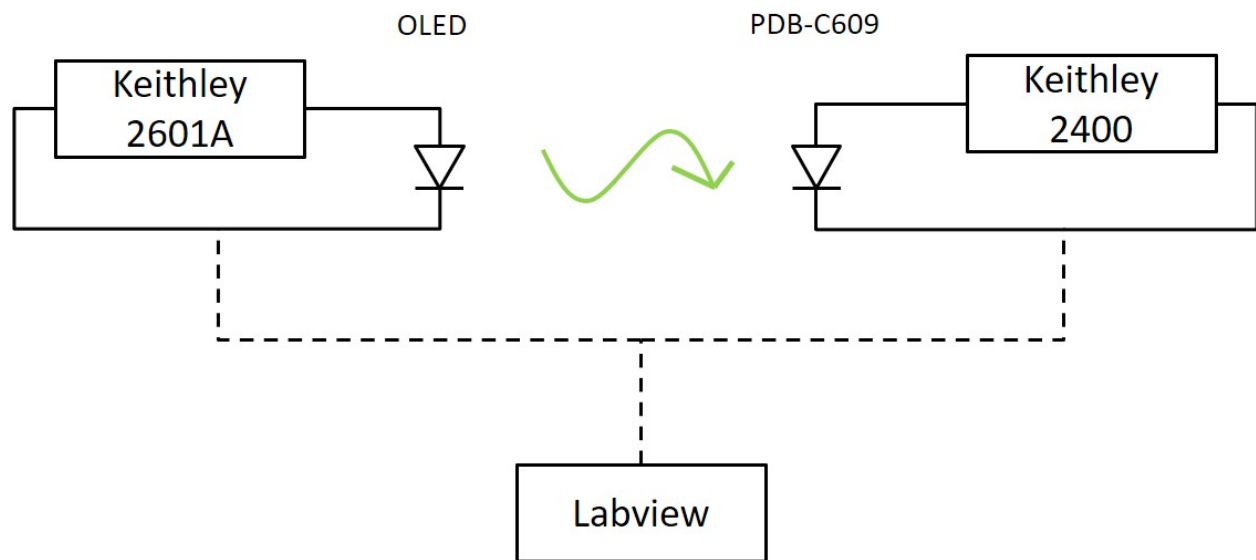
Figure 3.2: **Custom photodiode setup schematic for OLED characterization.**
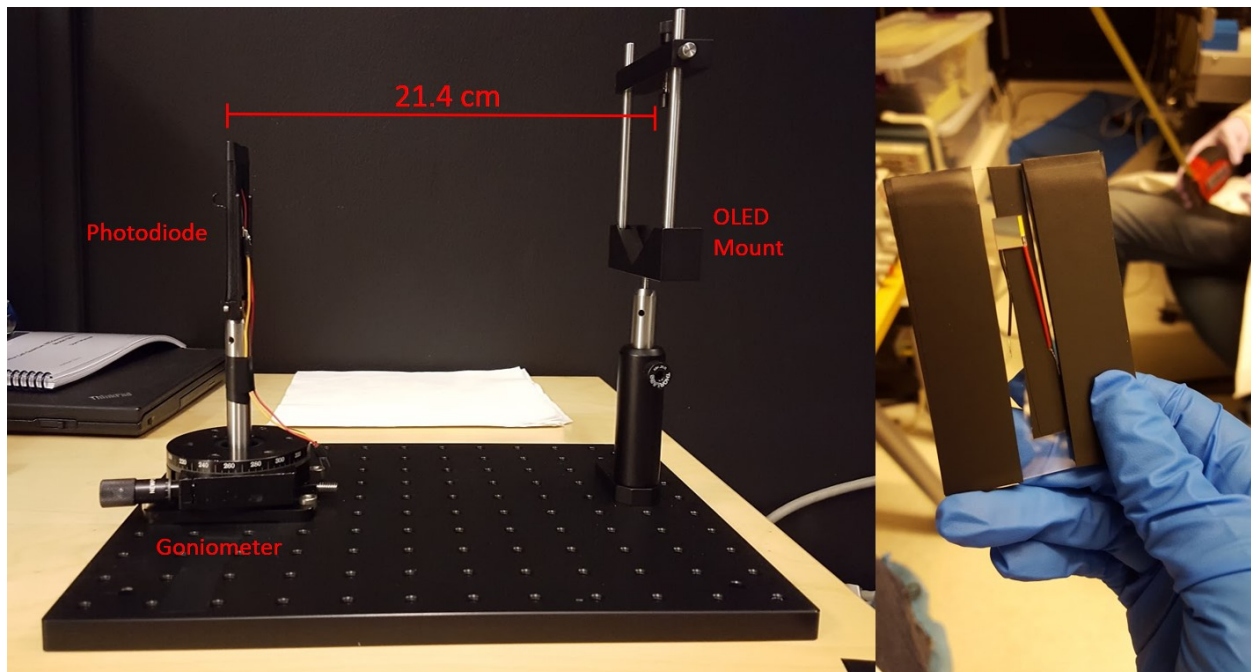
Figure 3.3: **Photo of custom photodiode setup for OLED characterization.**
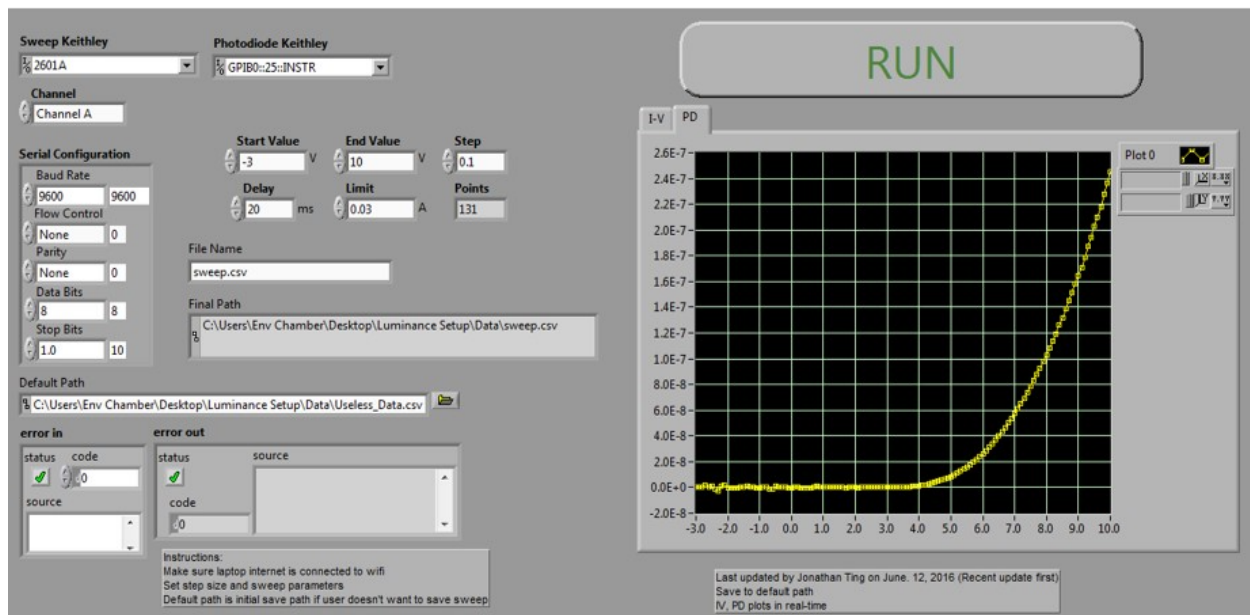
Figure 3.4: **LabVIEW control software for J-V-L measurement.**
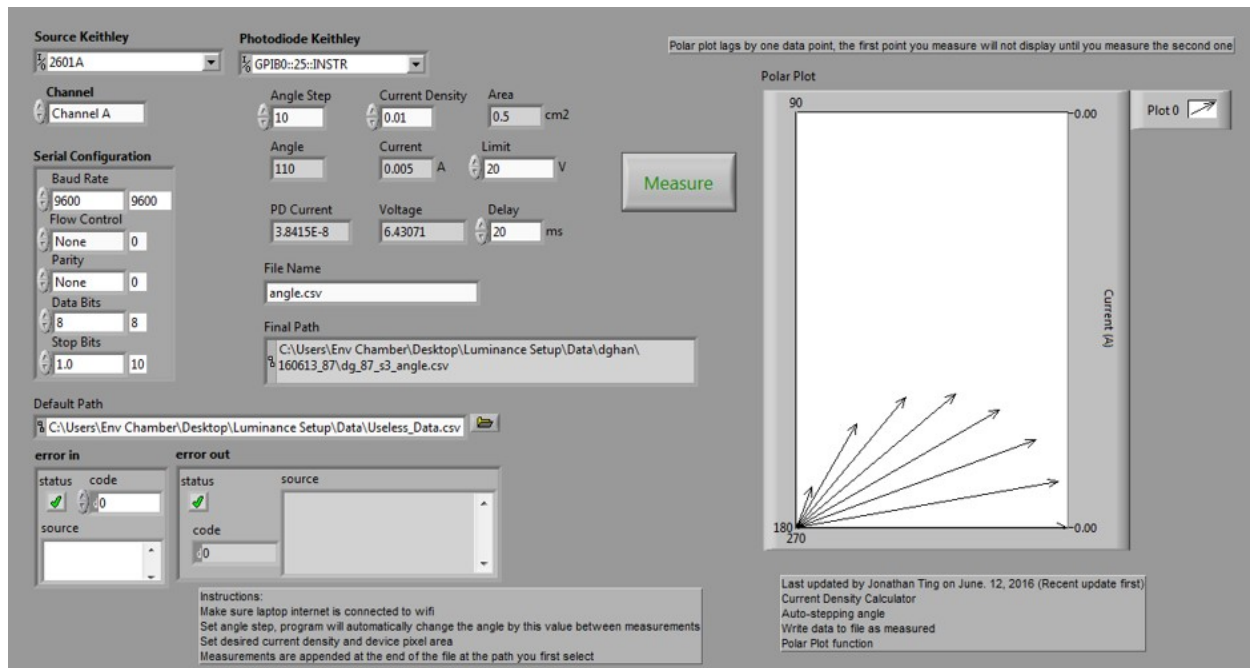
Figure 3.5: **LabVIEW control software for emission angle measurement.**
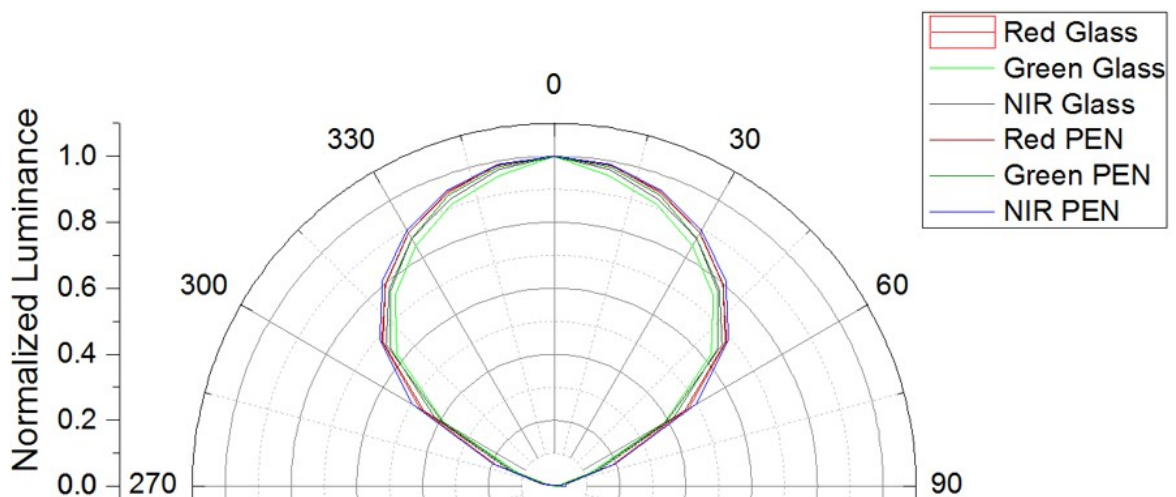
Figure 3.6: **Plotted normalized luminance vs. emission angle for vaious OLEDs.**

3.2.3   Radiometric and photometric values

Between a conventional integrating sphere setup, which is used frequently to characterize OLEDs, and the custom photodiode measurement setup described in the previous section, there are a variety of values that can be measured from device characterization. It is important to separate which values can be acquired by which measurement technique. In Tables 3.1 and 3.2, we can see the breakdown of these values. In each table, values are separated into the radiometric and photometric equivalents, and then color coded into values that can be acquired with said measurement technique, and values that cannot. Notably from Table 3.1, we find that many of the relevant photometric quantities cannot be acquired. In literature, values such as luminance and current efficacy are regularly reported. However, from Table 3.2, we find that almost all of the radiometric and photometric values can be computed, and the EQE can be interpolated from certain measurements. However, it should be noted that as part of the photodiode setup, a series of integrating sphere measurements must first be made in order to acquire information about the spectral intensity of the OLED emission. Without that information, the photometric values cannot be computed.

Radiometric			Photometric		
Quantity	Symbol	Units	Quantity	Symbol	Units
Radiant Power	Φ_e	W	Luminous Flux	Φ_v	lm
Irradiance	E_e	W/m^2	Illuminance	E_v	lm/m^2
Radiance	L_e	W/m^2-sr	Luminance	L_v	cd/m^2
EQE	η_{EQE}	%	Current Efficacy	η_I	cd/A

Table 3.1: Radiometric and photometric values for integrating sphere measurement. Cells marked in green are measurements that can be measured directly using the integrating sphere, where cells in red cannot.

Radiometric			Photometric		
Quantity	Symbol	Units	Quantity	Symbol	Units
Radiant Power	Φ_e	W	Luminous Flux	Φ_v	lm
Irradiance	E_e	W/m^2	Illuminance	E_v	lm/m^2
Radiance	L_e	W/m^2-sr	Luminance	L_v	cd/m^2
EQE	η_{EQE}	%	Current Efficacy	η_I	cd/A

Table 3.2: Radiometric and photometric values for photodiode setup measurement. Cells marked in green are measurements that can be measured directly using the integrating sphere, where cells in gray can be approximated.

3.3 Multi-channel reflection oximeter

3.3.1 Overview

A schematic illustration of a two-channel wrist-worn reflectance PPG sensor is shown in Figure 3.7a. The multi-channel sensor is designed using two circular sensors to collect PPG signals from the radial and the ulnar arteries (Figure 3.7b). The sensor is interfaced to multiplexers that switch between the pixels and connects to an analog front end (AFE). The AFE sequentially drives the OLEDs and reads out the OPD signals. Since the focus of this article is sensor design and optimization, we use a wired interface for data collection. However, the AFE can be interfaced with a wireless transceiver for wearable applications. Both red and NIR PPG signals are collected using the two pixels. Since most wearable PPG sensors are wrist-worn, we utilize the two-channel PPG sensor for on-wrist measurements. The underside of the wrist, especially on the radial and ulnar arteries, provide the best PPG signal magnitudes. One pixel (Ch 1) is placed on the ulnar artery, while the other pixel (Ch 2) is placed on the radial artery. A photograph of the multi-pixel sensor is shown in Figure 3.7c, where the sensor is bent to a radius of curvature of 5 cm to resemble bending on the wrist.

Reflection-mode sensors require light emitters and detectors assembled on a substrate or a circuit board [3–16]. Traditionally, red and NIR LEDs are placed on either side of the PD to assemble the sensor [17–24]. The designs of commercially available optoelectronic sensors are limited in shape - typically rectangular, which do not provide much versatility to vary the sensor geometry [1, 25–35]. On the other hand, printed optoelectronics can be fabricated in various shapes and sizes [4]. In this work, we explore three different sensor geometries as shown in Figure 3.8a-c: (1) Rectangular geometry (R), where the OLEDs are placed at either side of the OPD; (2) Bracket geometry (B), where the OLEDs are shaped as brackets and placed around the square OPD; (3) Circular geometry (C), where the OLEDs are shaped as block arcs and placed around the circular OPD. The rectangular sensor design is chosen to represent conventional sensors that use side-by-side optoelectronics placement. The bracket and the circular sensor geometries are non-traditional geometries chosen to improve PPG SNR. Figure 3.8d shows the sensor placement on the underside of the arm. Radial and ulnar arteries are marked to show sensor placement. All sensors are composed of printed red and NIR OLEDs with emission peaks at 630 and 725 nm respectively, and OPDs with external quantum efficiency (EQE) of 20% at the aforementioned wavelengths (Figure 3.8e). PPG signal magnitudes vary appreciably based on the sensor placement locations on the wrist.
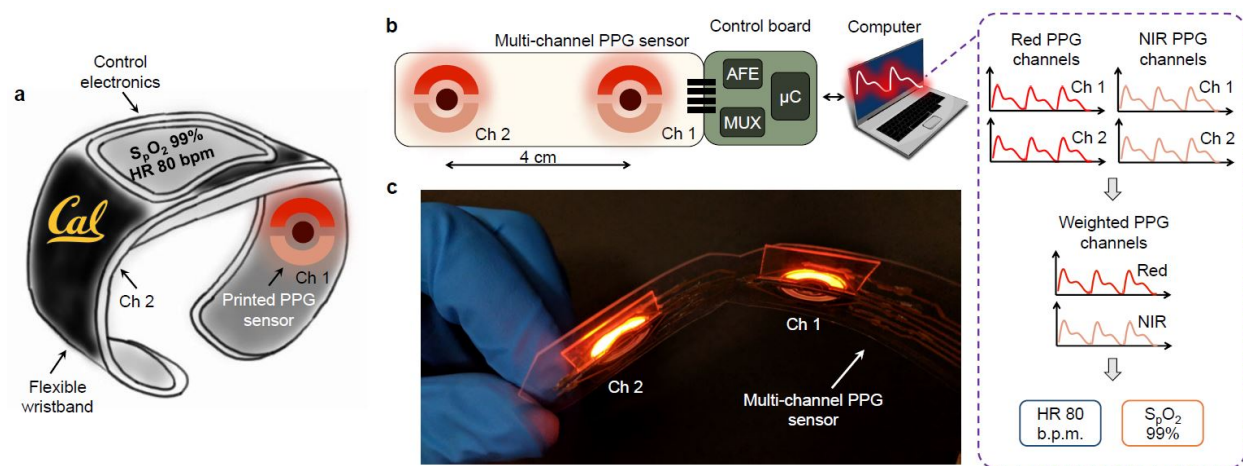
Figure 3.7: **Multi-channel reflectance PPG sensor overview. (a)** Schematic illustration of a wearable two-channel PPG sensor, where the PPG sensor pixels are mounted on the wristband. **(b)** Setup for the multi-channel PPG sensor. Two circular sensors are spaced 4 cm apart to collect data from the ulnar artery (Ch 1) and the radial artery (Ch 2). The sensor pixels are driven using an AFE, while multiplexers are used to switch between the pixels. Both red and NIR PPG signals are collected and processed for extracting HR and pulse oxygenation data. **(c)** Photograph of the multi-pixel reflectance PPG sensor bent to a radius of curvature of 5 cm.
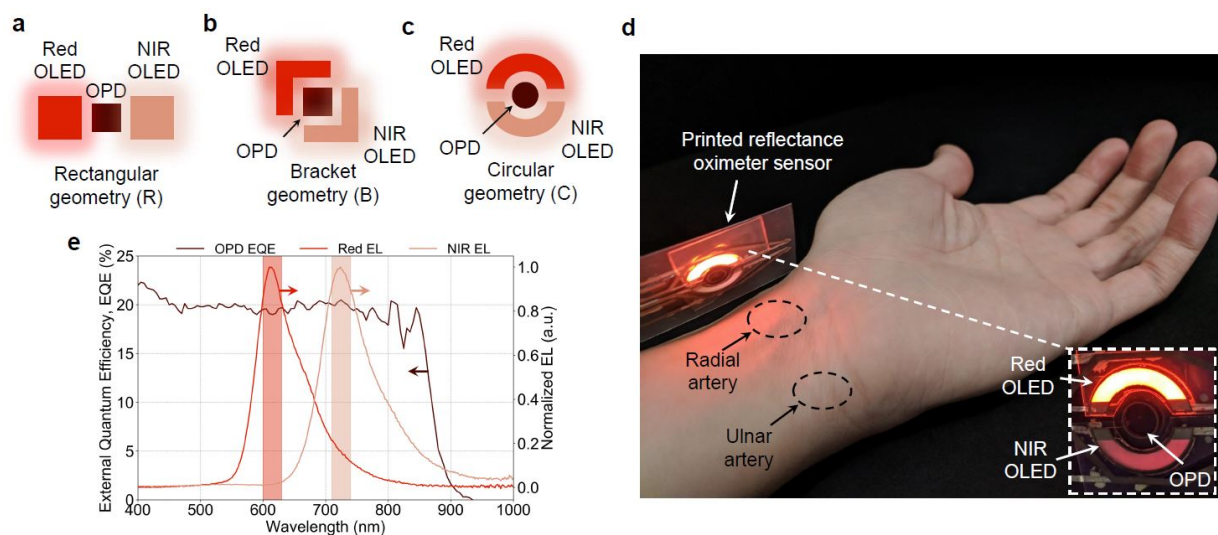
Figure 3.8: **Reflectance PPG sensor design and placement on the wrist. (a-c)** Different sensor geometries with the same active areas. **(a)** Rectangular geometry (R), where the OLEDs are placed at either side of the OPD. **(b)** Bracket geometry (B), where the OLEDs are shaped as brackets and placed around the square OPD. **(c)** Circular geometry (C), where the OLEDs are shaped as block arcs and placed around the circular OPD. **(d)** Photograph of the printed reflectance oximeter sensor placed on the underside of the wrist. The radial and ulnar artery sensing locations are marked to show sensor placement locations. The inset shows a circular sensor with red and NIR OLEDs on the top and the bottom side of the OPD, respectively. **(e)** Normalized electroluminescence (EL) of the red (red line) and NIR (peach line) OLEDs and EQE of the OPD (brick line). The OPD shows similar EQE at both red and NIR wavelengths.

3.3.2 Sensor assembly and calibration

A base polyethylene naphthalate (PEN) substrate is used to assemble the reflectance sensor. Inkjet-printed silver traces are used to route connections from the optoelectronics to the control electronics that consists of an AFE and a microcontroller with a universal serial bus (USB) interface to a computer. The OLEDs and the OPD are printed on separate plastic substrates and then assembled on the PEN substrate with silver traces as shown in Figure 3.9a. The photograph of the assembled sensor with the OLEDs and the OPD is shown in Figure 3.9b. Since we are comparing different sensor geometries, a two-step calibration is used to account for the batch-tobatch device variability of the OLEDs and the OPDs. A calibration platform composed of a silicon photodiode and a red LED is used to calibrate the assembled sensor, seen in Figure 3.10. In the first step, the OLEDs are calibrated using the silicon photodiode by operating the OLEDs at a fixed current and recording the photodiode current. The OLEDs of the assembled sensor are turned on sequentially to measure their intensities using the silicon photodiode. Each OLED is then calibrated to the maximum current measured in a batch of devices, $\kappa_{OLED} = \frac{max(I_{SiPD})}{I_{SiPD}}$. In the second step, the OPDs are calibrated by recording the OPD current while running the solid-state red LED at a fixed drive current. The red LED of the calibration platform is turned on and the OLEDs are turned off for calibrating the OPDs. The fabricated OPD detects light from the red LED and the measured photocurrent is recorded. Similar to the OLEDs, each OPD is then calibrated to the maximum OPD current measured in a batch of devices, $\kappa_{OPD} = \frac{max(I_{OPD})}{I_{OPD}}$. The obtained values are then used together with the measured PPG signal to calculate the calibrated signal magnitude. The calibration equation is given below, which is used to compare sensor performances for the three different geometries.

$$PPG_{cal} = \kappa_{OLED} \cdot \kappa_{OPD} \cdot PPG_{meas}[mV] \tag{3.10}$$

3.3.3 Placement

We explored three sensing locations: (i) On top of the wrist, (ii) on top of the ulnar artery, and (iii) on top of the radial artery and recorded PPG signals (Figure 3.11a and b). While the radial artery provided the cleanest signal (49.50 mV for red and 19.08 mV for NIR), the pulsatile PPG signal on top of the wrist was the weakest (Figure 3.11c). At the ulnar artery an order of magnitude improvement (26.12 mV for red and 9.02 mV for NIR) in PPG signal is observed over the wrist (3.24 mV for red and 0.94 mV for NIR). Therefore, we used our sensor on the underside of the wrist for both single and multi-channel measurements.
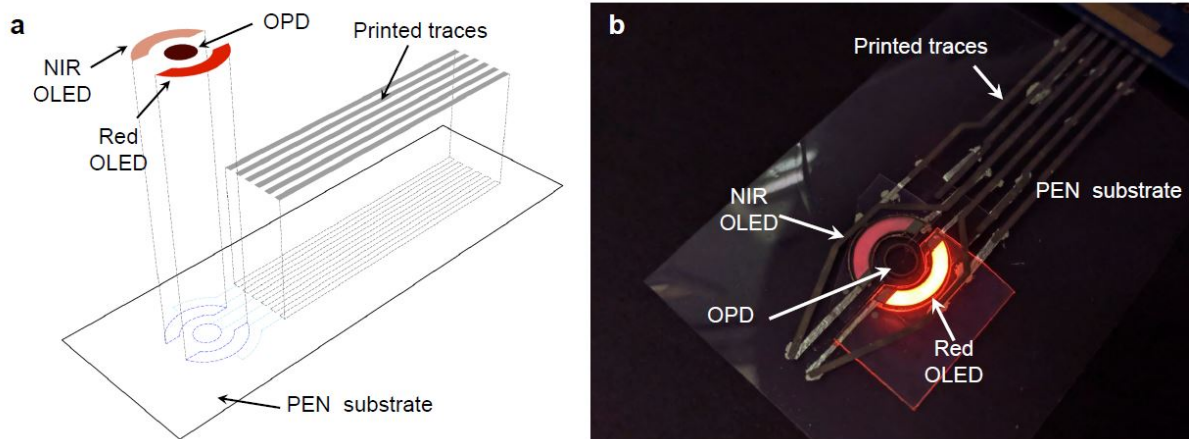
Figure 3.9: **Assembly of the printed sensor.** **(a)** Schematic depicting the sensor assembly. Polyethylene naphthalate is used as the base substrate. Inkjet-printed silver traces are used to connect the optoelectronic sensor to the control electronics. Red and NIR OLEDs and the OPD are then connected to complete the sensor. **(b)** Photograph of the assembled sensor.

$$Scaled\ Signal = \frac{Si\ PD\ Current\ Max}{Si\ PD\ Current} * \frac{OPD\ Current\ Max}{OPD\ Current} * Measured\ Signal$$
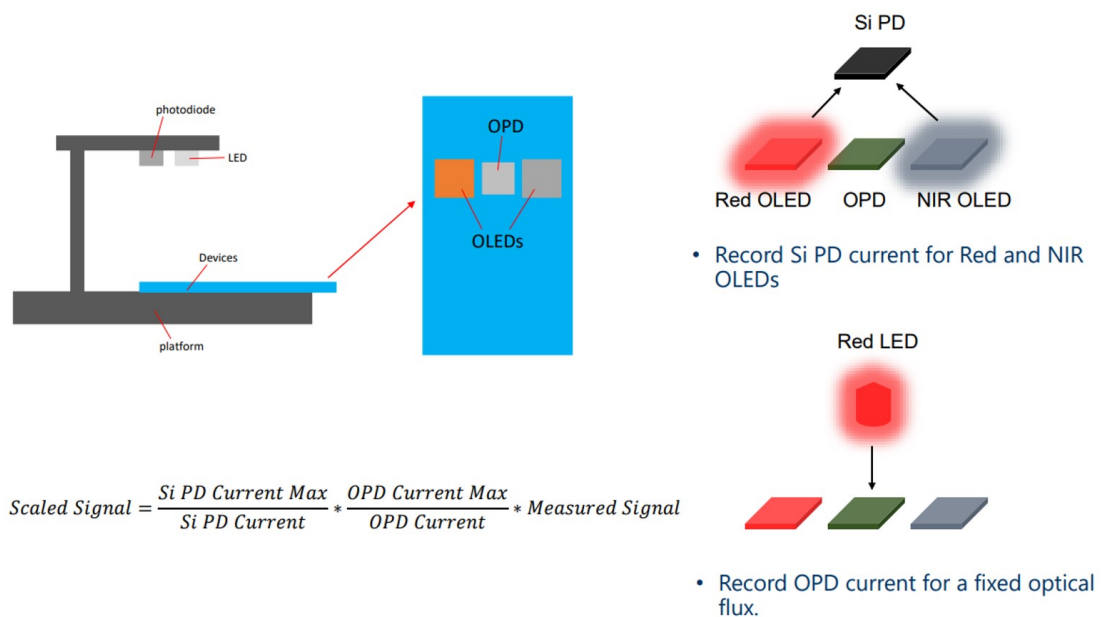
Figure 3.10: **Calibration setup and calculation for the various batches of OLEDs and OPDs.**
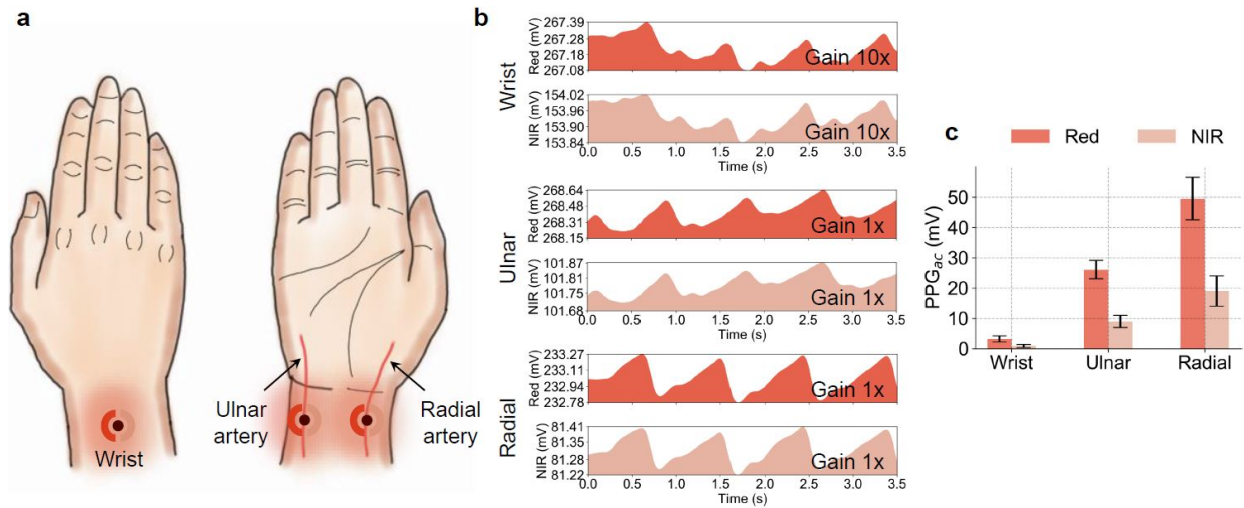
Figure 3.11: **PPG signal variation on the wrist. (a)** Three sensor placement locations are shown - (i) On top of the wrist, (ii) on top of the ulnar artery, and (iii) on top of the radial artery. **(b)** PPG signals from the wrist, ulnar and radial arteries are shown. Red color for the red channels and peach color for the NIR channels. Since the signal on the wrist is weak, a 10x gain setting is used to resolve the pulsatile PPG signal. **(c)** PPG signal magnitudes at the wrist, ulnar and radial arteries. The error bars represent data from 3 separate trials.

3.3.4 Spacing

After the calibration step, a fair comparison among the three different geometries can be performed. Additionally, we evaluate another important design parameter, emitter-detector spacing, d. Figure 3.12a-c show the photographs of the rectangular, bracket, and circular sensors with an emitter-detector spacing of 2, 4, and 6 mm, which are labeled as R2, R4, R6, B2, B4, B6, C2, C4, and C6. These labels are used in Figure 3.12d to show pulsatile PPG signal magnitude, PPG_{cal} based on (3.10). The rectangular sensor consists of OLEDs and an OPD that are all square-shaped which are placed side-by-side. Since the OLEDs do not surround OPD from the top and the bottom, this scheme is susceptible to ambient light, which contributes to the noise of the measurement. Also, a significant amount of light coming out from the left edge of the red OLED and the right edge of the NIR OLED do not contribute to the measurement, hence, gets lost. Ideally, a perimeter light source that surrounds the OPD would be the best. The two new schemes, the bracket, and the circular designs, where the light sources encompass the perimeter of the OPD enhance measurement SNR. As shown in Figure 3.12d, all three designs show an exponential decay with increasing d. Due to the perimeter lighting and better light collection by the OPD, both bracket and circular geometries outperform the rectangular design in terms of pulsatile PPG signal mag-
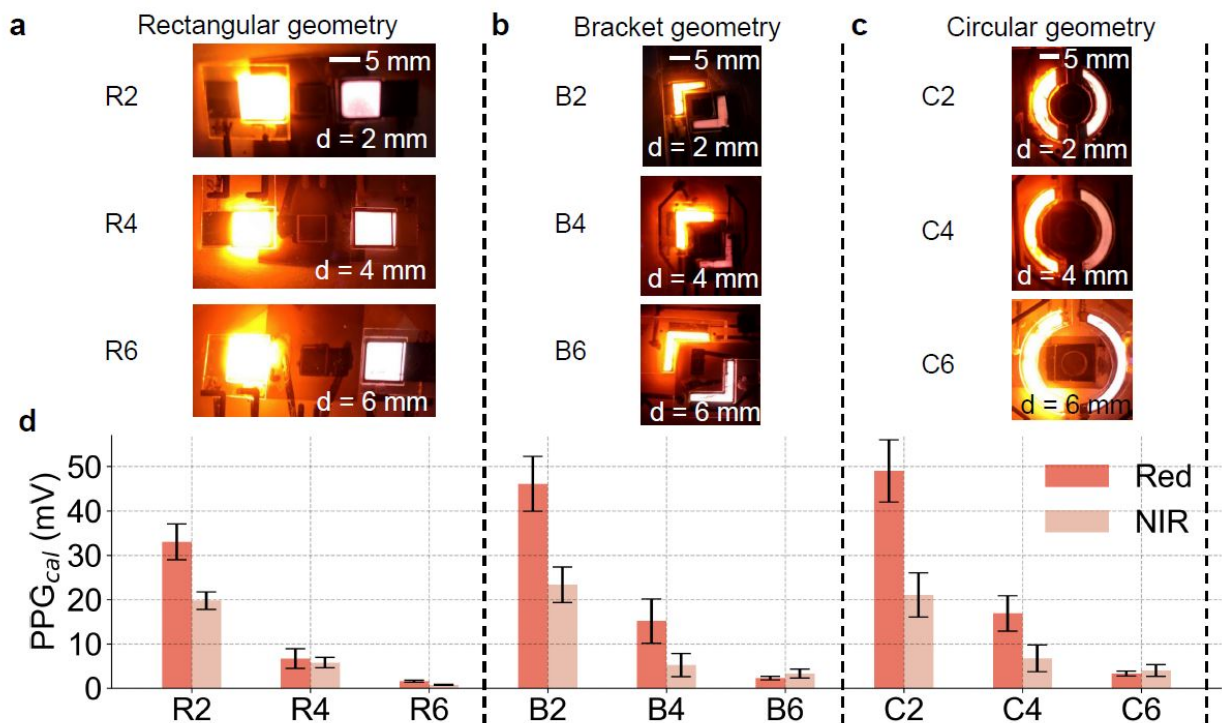
Figure 3.12: **Pulsatile signal magnitudes for different sensor spacings. (a)** Photographs of the rectangular sensors with emitter-detector spacing, d = 2, 4, 6 mm. The devices are labeled as R2, R4, and R6. **(b-c)** Similar to a, photographs of the bracket and circular sensors with emitter-detector spacing, d = 2, 4, 6 mm. The devices are labeled as B2, B4, B6, C2, C4, and C6. **(d)** The pulsatile signal magnitudes for all rectangular, bracket and circular sensors. Red-colored bars represent data for the red channel, while the peach-colored bars represent data from NIR channel. The error bars represent data from 3 separate trials.

nitude. While comparing the bracket and circular design, we observe a negligible difference in PPGcal.

3.3.5 Geometry

For a direct comparison of the different geometries, we kept the emitter-detector spacing constant at 2 mm, and kept the device area of the OLEDs and the OPDs same for all three geometries as shown in Figure 3.13a. The OPD areas are kept fixed at 16 mm2 and the OLED areas are kept fixed at 28 mm2. The PPG waveforms for the different geometries are shown in Figure 3.13b. Utilizing the bracket geometry, we observe 39.7% and 18.2% improvements in PPG signal magnitude in the red and NIR channels, respectively over the rectangular geometry. For the circular geometry, we observe 48.6% and 9.2% improvements in the red and NIR channels, respectively over the rectangular geometry. The bracket and the circular design show similar performance in the PPGcal (Figure 3.13c). Additionally, the two new designs bring down the overall length of the sensor from 18.6 mm for the rectangular geometry to 12 mm for the bracket and 13.2 mm for the circular geometry.

3.3.6 Optical isolation

In reflectance PPG and oximetry, the light coming back from the arteries contributes to the signal, while the light scattered from the skin surface contributes to noise. Therefore, blocking the light scattered from the skin surface enhances SNR. We incorporated the light blocking feature in our design by utilizing an optical barrier between the OLEDs and OPD. Black tape is cut into the shape that fits the area between the OLEDs and the OPD and is used to block scattered light. Figure 3.14a shows the schematic of the sensor. With the blocking layer, we observe 26.5 % improvement in PPG_{cal} in the red channel, and while PPG_{cal} remained almost the same in NIR. Red light scatters more on the skin surface than the NIR. Therefore, more red light scattered by skin surface gets blocked by the optical barrier, resulting in an improved red PPG_{cal} (Figure 3.14).

3.4 Chapter conclusions

In this chapter, we discussed the various performance parameters of OLEDs. We further explained the different types of characterization for OLEDs, and outlined a custom photodiode measurement setup for J-V-L characterization, as well as emission angle measurements. We additionally outlined our work on a multi-channel reflection oximeter. By utilizing the versatility of printed electronics, optoelectronic sensors for PPC and oximetry are fabricated in different shapes and sizes. In this work, we utilized non-conventional geometries such as bracket and circular designs to improve sensor performance. The new sensor geometries demonstrated a clear improvement over the conventional rectangular sensor design. The new sensor geometries not only improved the PPG signal magnitudes but also decreased the overall sensor size and reduced power consumption. These sensor designs coupled with multi-channel redundancy can be incorporated into wrist-worn devices, making them promising for wearable reflectance PPG and oximetry.
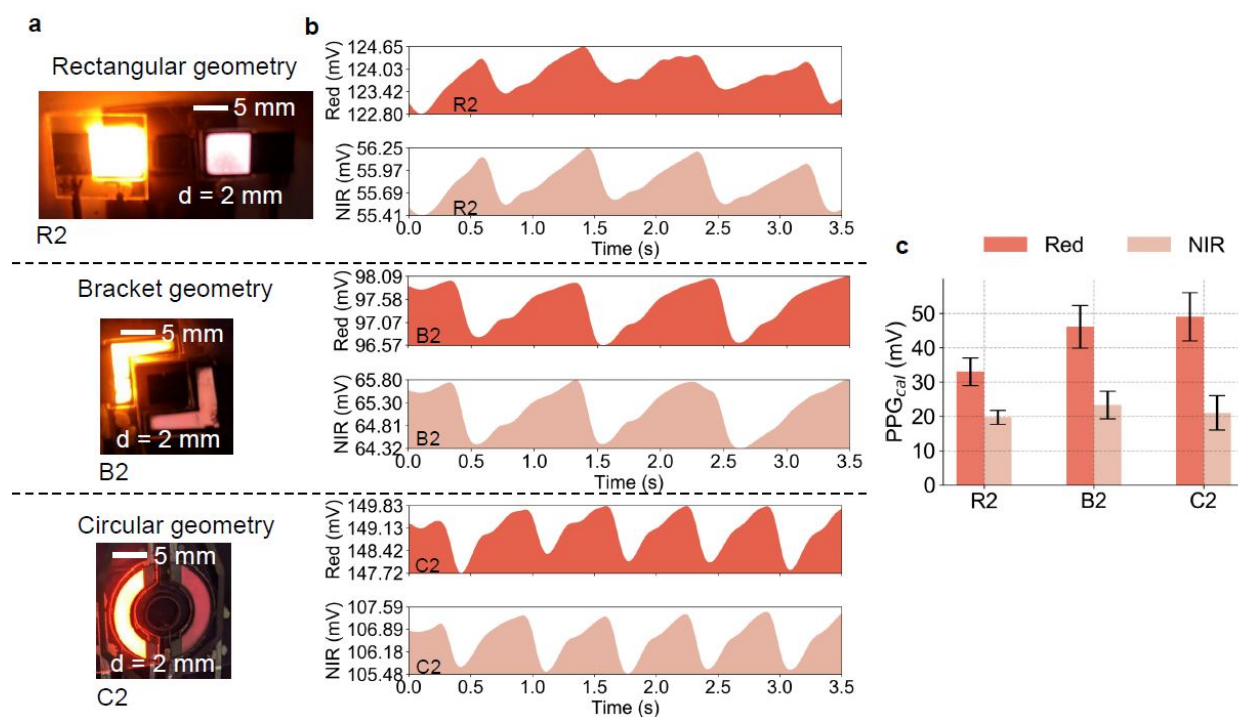
Figure 3.13: **Performance comparison of different sensor geometries.** **(a)** Photographs of the rectangular, bracket and circular sensors with an emitter-detector spacing of 2 mm. **(b)** PPG signals from the red and NIR channels for the sensors shown in a. **(c)** The pulsatile signal magnitudes for the smallest rectangular, bracket and circular sensors. Red-colored bars represent data for the red channel, while the peach-colored bars represent data from NIR channel. The error bars represent data from 3 separate trials.
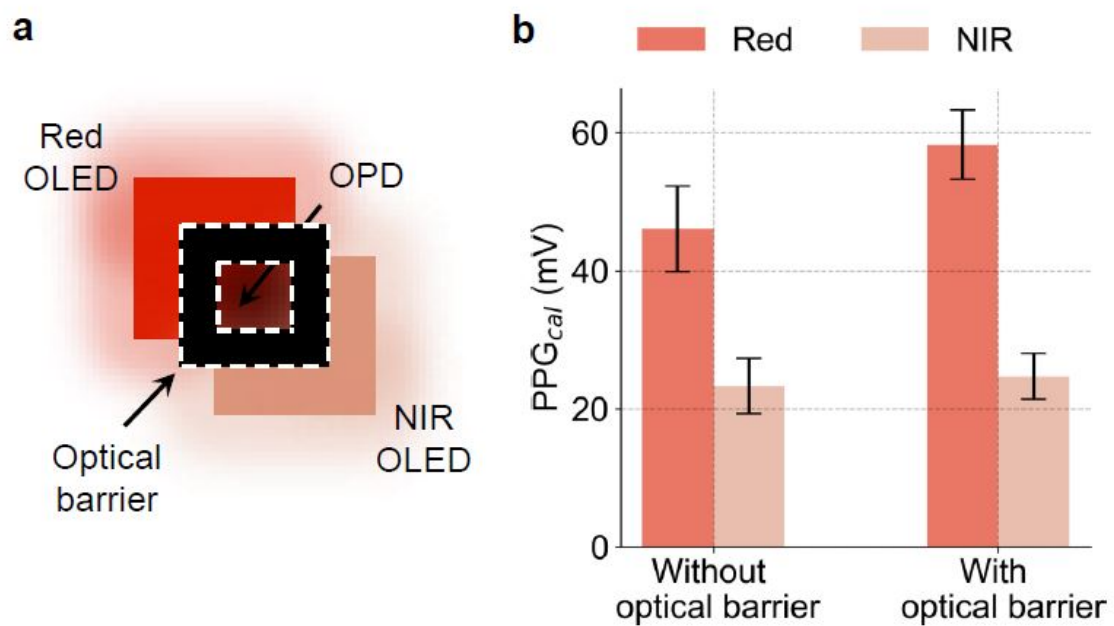
Figure 3.14: **The effect of an optical barrier in sensor performance. (a)** Schematic of a reflectance oximeter sensor, where an optical barrier is placed in between the emitters and the detector. **(b)** The pulsatile signal magnitudes of the red and NIR channels without and with the optical barrier. The error bars represent data from 3 separate trials.

3.5 References

[1] Yasser Khan, Donggeon Han, Jonathan Ting, Maruf Ahmed, Ramune Nagisetty, and Ana C. Arias. Organic multi-channel optoelectronic sensors for wearable health monitoring. *IEEE Access*, 7:128114–128124, 2019.

[2] Keith Anthony Knauer. High-Performance Single-Unit and Stacked Inverted Top-Emitting Electrophosphorescent Organic Light-Emitting Diodes. (May), 2014.

[3] Shahid Ismail, Usman Akram, and Imran Siddiqi. Heart rate tracking in photoplethysmography signals affected by motion artifacts: a review. *Eurasip Journal on Advances in Signal Processing*, 2021(1), 2021.

[4] Donggeon Han, Yasser Khan, Karthik Gopalan, Adrien Pierre, and Ana C. Arias. Emission Area Patterning of Organic Light-Emitting Diodes (OLEDs) via Printed Dielectrics. *Advanced Functional Materials*, 28(37), 2018.

[5] Shu Tyng Lin, Wei Hao Chen, and Yuan Hsiang Lin. A pulse rate detection method for mouse application based on multi-PPG sensors. *Sensors (Switzerland)*, 17(7), 2017.

[6] Yanbing Yang, Xiangdong Yang, Yaning Tan, and Quan Yuan. Recent progress in flexible and wearable bio-electronics based on nanomaterials. *Nano Research*, 10(5):1560–1583, 2017.

[7] Xudong Yang and Huanyu Cheng. Recent developments of flexible and stretchable electrochemical biosensors. *Micromachines*, 11(3), 2020.

[8] Arno Thielens, Igal Deckman, Reza Aminzadeh, Ana C. Arias, and Jan M. Rabaey. Fabrication and Characterization of Flexible Spray-Coated Antennas. *IEEE Access*, 6:62050–62061, 2018.

[9] Tomoyuki Yokota, Peter Zalar, Martin Kaltenbrunner, Hiroaki Jinno, Naoji Matsuhisa, Hiroki Kitanosako, Yutaro Tachibana, Wakako Yukita, Mari Koizumi, and Takao Someya. Ultraflexible organic photonic skin. *Science Advances*, 2(4):1–9, 2016.

[10] Ali Moin, Andy Zhou, Abbas Rahimi, Simone Benatti, Alisha Menon, Senam Tamakloe, Jonathan Ting, Natasha Yamamoto, Yasser Khan, Fred Burghardt, Luca Benini, Ana C. Arias, and Jan M. Rabaey. An EMG gesture recognition system with flexible high-density sensors and brain-inspired high-dimensional classifier. *arXiv*, 2018.

[11] Aminy E. Ostfeld, Abhinav M. Gaikwad, Yasser Khan, and Ana C. Arias. High-performance flexible energy storage and harvesting system for wearable electronics. *Scientific Reports*, 6(April):1–10, 2016.

[12] John G. Webster. *Design of pulse oximeters.* CRC Press, 1st edition, 1997.

[13] Da Yin, Nai Rong Jiang, Yue Feng Liu, Xu Lin Zhang, Ai Wu Li, Jing Feng, and Hong Bo Sun. Mechanically robust stretchable organic optoelectronic devices built using a simple and universal stencil-pattern transferring technology. *Light: Science and Applications*, 7(1), 2018.

[14] Hyeonwoo Lee, Eunhye Kim, Yongsu Lee, Hoyeon Kim, Jaeho Lee, Mincheol Kim, Hoi Jun Yoo, and Seunghyup Yoo. Toward all-day wearable health monitoring: An ultralow-power, reflective organic pulse oximetry sensing patch. *Science Advances*, 4(11):1–9, 2018.

[15] Jeonghyun Kim, Giovanni A. Salvatore, Hitoshi Araki, Antonio M. Chiarelli, Zhaoqian Xie, Anthony Banks, Xing Sheng, Yuhao Liu, Jung Woo Lee, Kyung In Jang, Seung Yun Heo, Kyoungyeon Cho, Hongying Luo, Benjamin Zimmerman, Joonhee Kim, Lingqing Yan, Xue Feng, Sheng Xu, Monica Fabiani, Gabriele Gratton, Yonggang Huang, Ungyu Paik, and John A. Rogers. Battery-free, stretchable optoelectronic systems for wireless optical characterization of the skin. *Science Advances*, 2(8), 2016.

[16] Zhiyuan Chen, Sofian N. Obaid, and Luyao Lu. Recent advances in organic optoelectronic devices for biomedical applications. *Optical Materials Express*, 9(9):3843, 2019.

[17] Varun V. Soman, Yasser Khan, Madina Zabran, Mark Schadt, Paul Hart, Michael Shay, Frank D. Egitto, Konstantinos I. Papathomas, Natasha A.D. Yamamoto, Donggeon Han, Ana Claudia Arias, Kanad Ghose, Mark D. Poliks, and James N. Turner. Reliability Challenges in Fabrication of Flexible Hybrid Electronics for Human Performance Monitors: A System-Level Study. *IEEE Transactions on Components, Packaging and Manufacturing Technology*, 9(9):1872–1887, 2019.

[18] Sungmook Jung, Seungki Hong, Jaemin Kim, Sangkyu Lee, Taeghwan Hyeon, Minbaek Lee, and Dae Hyeong Kim. Wearable Fall Detector using Integrated Sensors and Energy Devices. *Scientific Reports*, 5:1–9, 2015.

[19] Mark Poliks, James Turner, Kanad Ghose, Zhanpeng Jin, Mohit Garg, Qiong Gui, Ana Arias, Yasser Kahn, Mark Schadt, and Frank Egitto. A Wearable Flexible Hybrid Electronics ECG Monitor. *Proceedings - Electronic Components and Technology Conference*, 2016-August:1623–1631, 2016.

[20] Takao Someya, Zhenan Bao, and George G. Malliaras. The rise of plastic bioelectronics. *Nature*, 540(7633):379–385, 2016.

[21] Joanna M. Nassar, Kush Mishra, Kirklann Lau, Andres A. Aguirre-Pablo, and Muhammad M. Hussain. Recyclable Nonfunctionalized Paper-Based Ultralow-Cost Wearable Health Monitoring System. *Advanced Materials Technologies*, 2(4):1–11, 2017.

[22] Suji Choi, Sang Ihn Han, Dongjun Jung, Hye Jin Hwang, Chaehong Lim, Soochan Bae, Ok Kyu Park, Cory M. Tschabrunn, Mincheol Lee, Sun Youn Bae, Ji Woong

Yu, Ji Ho Ryu, Sang Woo Lee, Kyungpyo Park, Peter M. Kang, Won Bo Lee, Reza Nezafat, Taeghwan Hyeon, and Dae Hyeong Kim. Highly conductive, stretchable and biocompatible Ag–Au core–sheath nanowire composite for wearable and implantable bioelectronics. *Nature Nanotechnology*, 13(11):1048–1056, 2018.

[23] Muhammad Fahad Farooqui and Atif Shamim. Low Cost Inkjet Printed Smart Bandage for Wireless Monitoring of Chronic Wounds. *Scientific Reports*, 6(June):1–13, 2016.

[24] Christina Orphanidou, Timothy Bonnici, Peter Charlton, David Clifton, David Vallance, and Lionel Tarassenko. Signal-quality indices for the electrocardiogram and photoplethysmogram: Derivation and applications to wireless monitoring. *IEEE Journal of Biomedical and Health Informatics*, 19(3):832–838, 2015.

[25] Yongbo Liang, Mohamed Elgendi, Zhencheng Chen, and Rabab Ward. Analysis: An optimal filter for short photoplethysmogram signals. *Scientific Data*, 5:1–12, 2018.

[26] Hao Qu and Jean Gotman. A patient-specific algorithm for the detection of seizure onset in long-term EEG monitoring: Possible use as a warning device. *IEEE Transactions on Biomedical Engineering*, 44(2):115–122, 1997.

[27] Mathias Baumert, Vito Starc, and Alberto Porta. Conventional QT variability measurement vs. template matching techniques: Comparison of performance using simulated and real ECG. *PLoS ONE*, 7(7), 2012.

[28] Francesco Rundo, Sabrina Conoci, Alessandro Ortis, and Sebastiano Battiato. An advanced bio-inspired photoplethysmography (PPG) and ECG pattern recognition system for medical assessment. *Sensors (Switzerland)*, 18(2), 2018.

[29] Hyonyoung Han, Min Joon Kim, and Jung Kim. Development of real-time motion artifact reduction algorithm for a wearable photoplethysmography. *Annual International Conference of the IEEE Engineering in Medicine and Biology - Proceedings*, pages 1538–1541, 2007.

[30] Zhilin Zhang, Zhouyue Pi, and Benyuan Liu. TROIKA: A general framework for heart rate monitoring using wrist-type photoplethysmographic signals during intensive physical exercise. *IEEE Transactions on Biomedical Engineering*, 62(2):522–531, 2015.

[31] M. Raghu Ram, K. Venu Madhav, E. Hari Krishna, Nagarjuna Reddy Komalla, and K. Ashoka Reddy. A novel approach for motion artifact reduction in PPG signals based on AS-LMS adaptive filter. *IEEE Transactions on Instrumentation and Measurement*, 61(5):1445–1457, 2012.

[32] Fulai Peng, Zhengbo Zhang, Xiaoming Gou, Hongyun Liu, and Weidong Wang. Motion artifact removal from photoplethysmographic signals by combining temporally constrained independent component analysis and adaptive filter. *BioMedical Engineering Online*, 13(1), 2014.

[33] Kristen M. Warren, Joshua R. Harvey, Ki H. Chon, and Yitzhak Mendelson. Improving pulse rate measurements during random motion using a wearable multichannel reflectance photoplethysmograph. *Sensors (Switzerland)*, 16(3), 2016.

[34] Yasser Khan, Donggeon Han, Adrien Pierre, Jonathan Ting, Xingchun Wang, Claire M. Lochner, Gianluca Bovo, Nir Yaacobi-Gross, Chris Newsome, Richard Wilson, and Ana C. Arias. A flexible organic reflectance oximeter array. *Proceedings of the National Academy of Sciences of the United States of America*, 115(47):E11015–E11024, 2018.

[35] Claire M. Lochner, Yasser Khan, Adrien Pierre, and Ana C. Arias. All-organic optoelectronic sensor for pulse oximetry. *Nature Communications*, 5:1–7, 2014.

Chapter 4

Printed battery arrays

4.1 Introduction

Miniaturization of electronic components has been realized; this has allowed us to fabricate miniature devices that can be used in a wide range of applications: from Internet of Things (IoT) devices [1, 2] to wearable health monitoring devices [3–5]. While advances have been made to scale these devices, further work is needed to design on-board power supplies for these miniaturized devices [6, 7]. Printed batteries are an emerging solution to providing on board power supplies due to their small form factor, design flexibility, ease of manufacturing, and low fabrication cost [7, 8]. Printing-based fabrication techniques offer several advantages towards on-chip integration and are capable of simplifying system level design [6, 9]. These methods utilize high-throughput processing methods that can additively integrate battery packaging and interconnects, eliminating the need for traditional battery form factors such as coin or pouch cells. Furthermore, printing-based techniques are compatible with emerging microelectronics processing techniques such as wafer-level and chip-scale packaging.

While printed single-cell batteries using various chemistries such as Zn-MnO$_2$, Zn-Ag$_2$O, and lithium ion have been demonstrated [10–18], they are shown to be suitable for low voltage applications due to their low operating voltages of less than 4 V. As electronics tends towards device miniaturization, there continues to be a demand for higher voltage on-board power supplies. For example, millimeter scale single chip nodes will likely rely on microelectromechanical system (MEMS) components, which typically require relatively high pull-in voltages (5–30 V) [16]. Although electrochemical cell potentials cannot meet these demands, combining several cells in series can provide sufficient energy and power to drive high voltage components. By combining these solution processable battery systems with high throughput printing techniques, we can realize highly customizable batteries of varying dimension and capacity. Printed battery arrays offer one way of addressing the variable design requirements for application specific cell potentials [16].

In this chapter, we will discuss our efforts towards developing an printed energy stor-

age solution for flexible hybrid electronics. For this work, a fully solution-processed battery design and process utilizing the Zn-Ag$_2$O chemistry is demonstrated. The batteries are screen-printed in ambient conditions with custom Zn and Ag$_2$O inks. The viscosity of these inks were optimized to maximize the quality and thickness of the printed films. The individual battery cells are designed with a vertical geometry where printed current collectors, anode, separator, and cathode are stacked together. The screen-printed batteries have an area of 0.25 cm^2, with 120 μm thick Zn electrode films and 70 μm thick Ag$_2$O electrode films. In addition, the vertical geometry is designed to allow for vertical interconnects, creating series connections between adjacent cells. By connecting these cells in series, we are able to realize battery arrays with open circuit voltages of 3 V, 6 V, and 9 V, and can reach power densities up to 72 mW cm^{-2}. Because any number of cells can be connected in series, any open circuit voltage that is a multiple of 1.5 V could be demonstrated. [1–29] Portions of this chapter are submitted for review in [23].

4.2 Battery architecture

4.2.1 Substrate

There are a variety of substrates used to fabricate printed batteries in literature. For this work, we initially considered glass as the substrate based on previous works demonstrating printed batteries from [10]. However, due to the thick cross section of the glass slide substrate, around 1 mm, the screen-mesh began to form light indentation patterns during the screen-printing process. Because of this significant stretching defect, the screen began to slightly lose tension in regions that were repeatedly printed during prolonged use, ultimately affecting the amount of force required to maintain screen contact to the substrate. In addition, because of the sharp edges of the glass substrate, the damage to the screen could ultimately cause screen tearing and permanently render the screen unusable. A discussion on screen degradation is included below. Unlike flexible substrates, glass substrates cannot be easily cut and resized without leaving potentially sharp edges from the use of a diamond tip cutter. Even with the use of these tools, it is very difficult to acquire a precise dimension for the substrate. Using a diamond tip cutter requires scoring the substrate and then folding it along the scored region, which does not guarantee a perfectly straight edge, or an exact dimension. Because of the fixed dimensions of the glass slides used in the lab (75 mm x 25 mm x 1 mm, or 75 mm x 50 mm x 1 mm), the dimensions of the batteries fabricated can only be as large as the dimension of the substrates if not smaller, ultimately limited the fabrication dimensions of the arrays.

One solution was to move to a different substrate entirely, and as such a flexible substrate was selected. Flexible substrates remove many of the restrictions that the glass substrates had. The can be easily cut and resized, as well as being arbitrarily thin without damaging the screens during printing. We selected polyimide (PI), colloquially known as Kapton, as the substrate for this work. 125 μm thick Kapton is commonly available in the lab and was

used in the rest of the fabrication for this work.

4.2.2 Current collector

A current collector is needed in order to transfer charge to the anode and cathode of the battery. Ideally, this current collector should be as conductive as possible to minimize series internal resistance of the battery, reducing the performance. Furthermore, the current collector must be chemically stable and not react with the electrolyte of the battery. Should there be poor chemical stability between the two, the current collector or electrodes could corrode or delaminate, which would ultimately reduce the performance of the cell. In addition, the electrodes fabricated must have good adhesion to the current collector below it, else there would be additional delamination issues. Finally, to fabricate a fully solution processable battery, the currently collector itself must also be solution processable.

At the early stages of this work, evaporated gold on glass was used as a current collector. However, this process is time consuming and expensive, and we eventually moved away from using gold. Despite there being screen-printable gold inks from Creative Materials, our unfamiliarity with the ink and the cost drove us to select a different material system.

We briefly tested screen-printed nickel (Creative Materials #116-26) as an alternative printed current collector. Although the printed nickel current collectors were chemically stable in the presence of the 8 M KOH electrolyte, the nickel films were not as electrically conductive as we would have liked. The datasheet provided from the nickel ink stated they would have a sheet resistance of 50 Ω/sq at the suggested curing temperature [22], however we wanted to further minimize this resistance. Several experiments varying temperature, anneal time, and plasma treatment were carried out, however we were unable to realize current collectors with sheet resistance below 10 Ω/sq. Therefore, printed nickel was not selected as the current collectors of the system.

We were already familiar with printed silver inks from previous works, and so we tried using a screen-printed silver ink (Creative Materials #126-33) as the current collector. Commercially available silver inks exhibit very low resistance. Although the chemical stability of silver in the presence of KOH is not as good when compared to the stability of nickel [19, 21], we went ahead and fabricated batteries with this current collector configuration. To date, we have yet to see any swelling, cracking, or corrosion of the current collectors fabricated with silver. However it should be noted that all of these defects would pose an issue in the battery system and reduce battery performance, and should be regularly investigated to ensure the quality of the current collector.

4.2.3 Electrodes

In the Zn-Ag$_2$O battery chemistry, zinc functions as the anode and silver-oxide functions as the cathode [18]. For a printed battery system, the areal capacity is directly proportional to the electrode film thickness, as well as the mass loading in the films. In addition, thicker zinc electrode films result in higher long term stability, which can improve the yield rate and

cell performance. The effects of various parameters on the printed film quality is discussed in the following sections.

Polyethylene oxide (PEO) binder is used to make Zn and Ag2O slurries for screen printing. PEO is chosen for the binder for the electrode slurries because it is water soluble [24], eliminating the need for flammable components from the electrode slurry. Furthermore, PEO is biodegradable, which is a desirable property for disposable primary batteries. Most importantly, by varying the concentration of PEO, the viscosity of the binder can be tuned; details about the effects of viscosity on printing are discussed in a later section.

The binder used for the zinc slurries consists of 4 wt% PEO (M_v = 600, 000) (Sigma #182028) with 1 wt% PEG 400 in DI water. The binder solution was stirred with a stir bar for 2 hours at 500 rpm to homogenize the solution. The zinc slurry contained 92 wt% Zn (Alfa#10835), 5 wt% ZnO (Sigma #677450), 1 wt% Bi2O3 (Alfa #45582), 1 wt% In2O3 (Alfa #40394), and 1 wt% binder. The additives (ZnO, Bi2O3, In2O3) help to suppress hydrogen gas evolution and reduce the rate of zinc corrosion during fabrication and operation. The slurry was hand mixed in a vial using a wooden applicator for about 5 minutes. The Zn electrodes were screen printed on top of the current collectors. After printing, the electrodes are dried at 40 °C to improve electronic conductivity in the electrode.

The binder used for the silver oxide slurries consists of 4.5 wt% PEO (M_v = 600, 000) (Sigma #182028) with 1 wt% PEG 400 in DI water. The binder solution was stirred with a stir bar for 2 hours at 500 rpm to homogenize the solution. The slurry contained 96 wt% Ag_2O (Strem #93- 4743), and 4 wt% binder. The slurry was hand mixed in a vial using a wooden applicator for about 5 minutes. The Ag_2O electrodes were screen printed on top of a separate sheet of current collectors. The printed square electrodes have an area of 0.25 cm^2. The printed Zn electrodes have thicknesses of approximately 120 μm and the printed Ag_2O electrodes have thicknesses of approximately 70 μm.

4.2.4 Separator, electrolyte, and encapsulation

A printable sol–gel using a photopolymerizable polyacrylic acid (PAA) solution previously reported in our group was used as the separator between the anode and the cathode [22]. In addition to being printed, this sol-gel allows a vertical cell structure to be realized, which helps limit the device footprint. The sol-gel separator soaked in 8 M KOH electrolyte dissolved with 2.1 g ZnO was then encapsulated in a polydimethylsiloxane (PDMS) ring to prevent electrolyte dehydration and ensure suitable ionic conductivity across the separator throughout battery operation [26].

To prepare the separator, a solution of composed of 0.092 g PEO (M_v = 400, 000) (Sigma #372773), 250 μL of acrylic acid (Sigma #147230), and 1 wt% PEG 400 mixed in 3.125 mL of 1 M KOH was prepared by stirring it for 2 hours at 500 rpm to allow the PEO to dissolve. Next, and 0.0185 g of photoinitiator (M_w = 224.25) (Sigma #410896) and 0.037 g of PEDGE crosslinker (M_n = 250) (Sigma #410195) were added to the solution and stirred for 15 min at 650 rpm. The solution was then bubbled with nitrogen gas for 10 min to deoxygenate the solution. The solution was UV cured using a Spectroline SB-100P UV lamp

for 10 min. Finally, the separator was soaked in $15\mu L$ of 8 M KOH electrolyte mixed with 2.1g ZnO for 15 min.

The PDMS ring was prepared by mixing the PDMS stock and the curing agent in a 10:1 ratio and then placed in a desiccator for about 15 minutes to remove any bubbles. Next, the PDMS was spin coated on a silicon wafer for 30 seconds at 150 rpm. The PDMS was cured at 150 °C for 10 minutes. Finally, the PDMS was cut to its desired pattern using a laser cutter.

4.2.5 Series interconnects

In order to connect adjacent printed Zn-Ag$_2$O cells in series, a vertical interconnect was introduced to the fabrication process. After laminating the separator, a screen-printable silver ink (Creative Materials #126-22) was drop-cast directly on top of the printed silver current collector. This configuration allows for a direct contact between the anode of one cell to the cathode of the adjacent cell. By doing so, we are able to fabricate any integer number of cells in series to form an $n \times n$ array, however for this work we report on the results of single-cell batteries, as well as 2 x 1, 2 x 2, and 2 x 3 arrays.

4.2.6 Fabrication process

Figure 4.1b shows the full process flow of the printed Zn-Ag$_2$O battery arrays. Starting with an untreated Kapton substrate, silver current collectors are deposited using screen printing. A second substrate with the same current collector pattern is prepared. We then screen-print Zn and Ag$_2$O electrodes onto their respective current collector substrates. Spin-coated polydimethylsiloxane (PDMS) encapsulation rings are then laminated to the surface of the zinc electrode array substrate. The PDMS encapsulation layer has shown to be printed in other works. In order to connect the anode of one battery cell to the cathode of an adjacent cell, silver interconnects were added to the design. The silver interconnects for the series connection were drop-casted onto the Kapton substrate in between the PDMS encapsulation layers, before laminated the two separate zinc and silver oxide electrode arrays together. These interconnects were drop casted directed in between two adjacent PDMS ring edges, separated the adjacent zinc electrodes. Afterwards, the sol-gel soaked in KOH electrolyte was placed on top of each zinc electrode. Finally, the array of Ag$_2$O electrodes were laminated together by visually aligning the printed alignment marks on the zinc and silver oxide substrates. A single-cell battery schematic is shown in Figure 4.1a, and a fully assembled 2 x 3 Zn-Ag$_2$O battery array schematic is shown in Figure 4.1c.
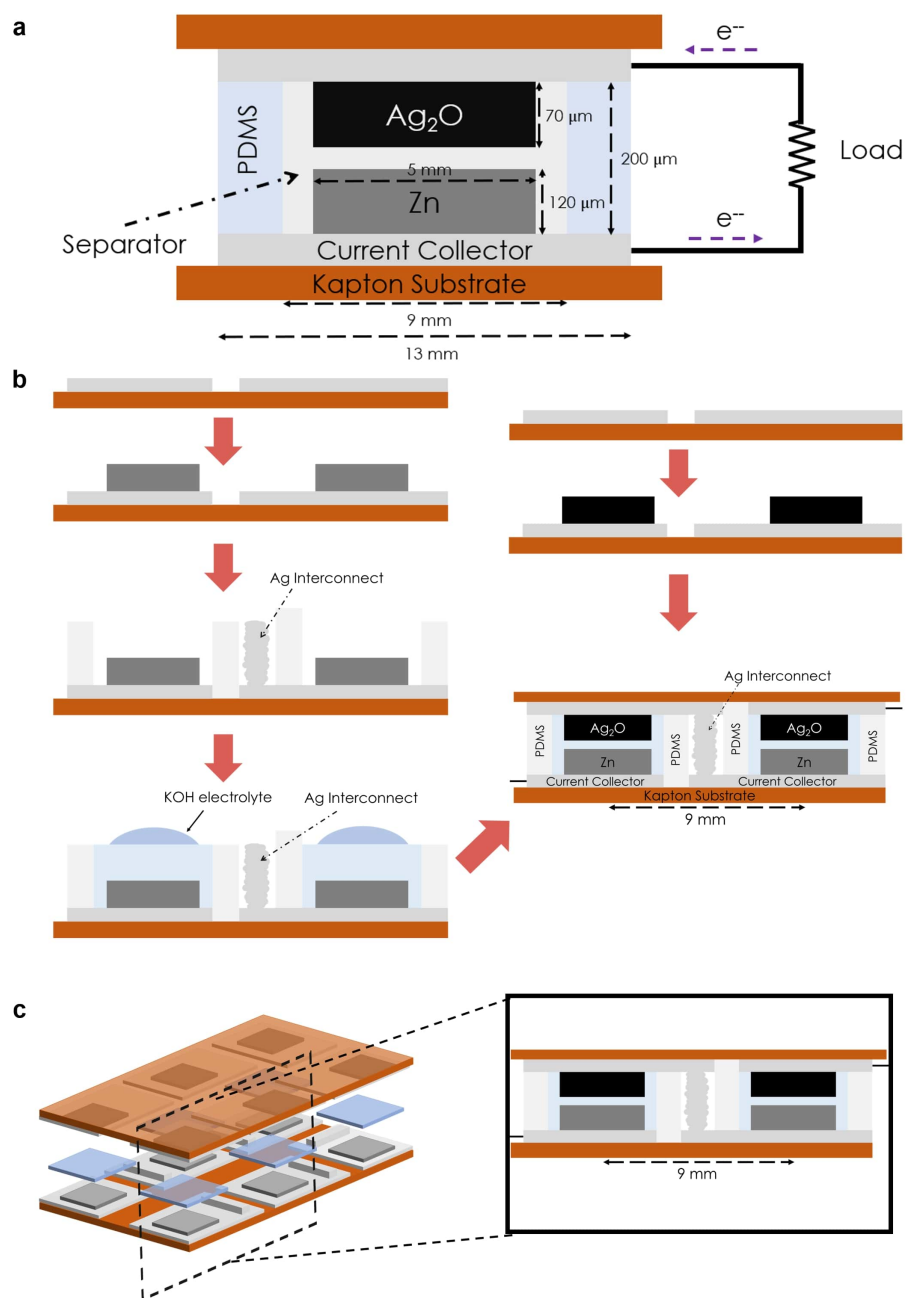
Figure 4.1: **Zn-Ag$_2$O single-cell and array fabrication schematic.** **(a)** Schematic of single-cell screen-printed Zn-Ag$_2$O battery. **(b)** Process flow for printing and assembling printed 2 x 1 Zn-Ag$_2$O battery array. **(c)** Schematic of printed Zn-Ag$_2$O battery array assembly.
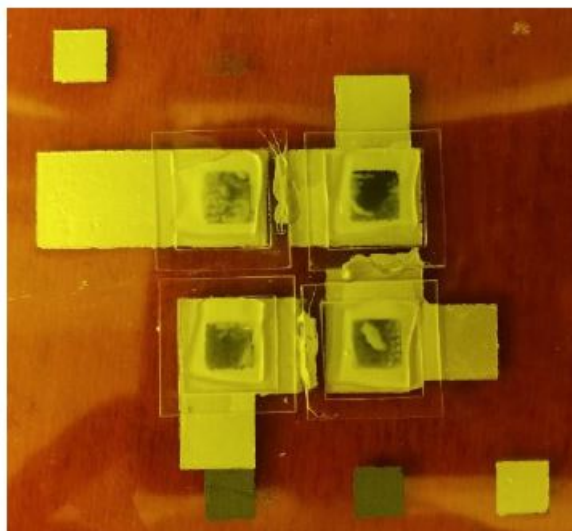
Figure 4.2: **White ZnO precipitate formation on printed Zn electrodes due to poor electrode print quality.**

4.3 Screen-printable electrode optimization

4.3.1 Electrode film quality

As part of the ink optimization process, the film quality of the zinc and silver oxide printed electrodes was evaluated. To first order, the quality of each of these films influences the performance of the battery. A variety of defects can occur during the printing process, including non-uniform film thickness, pinhole defects, misprints, etc. All of these influence the quality of the battery to some degree and, depending on the severity, can cause the battery to fail catastrophically. In Figure 4.2, we see an example of a battery with poorly printed electrode films resulting in rapid corrosion on the zinc electrodes. As such, the following sections discuss how the electrode inks were optimized for thickness and film uniformity.

4.3.2 Ink viscosity

Figure 4.3a shows a plot of shear rate against viscosity for PEO binder at various concentrations (by weight) in water. It is shown that the viscosity of the binder can be tuned by varying the concentration of the PEO in the binder. In general, as the PEO concentration of the binder increases, the viscosity of the binder increases. This allows us to tune the viscosities of the binders for the electrode inks used in screen printing. Optical microscope images of printed Ag_2O film using binder concentrations of 1-4 % are found in Figures 4.3b-e. One critical parameter when developing screen printable inks is the ink viscosity. While screen
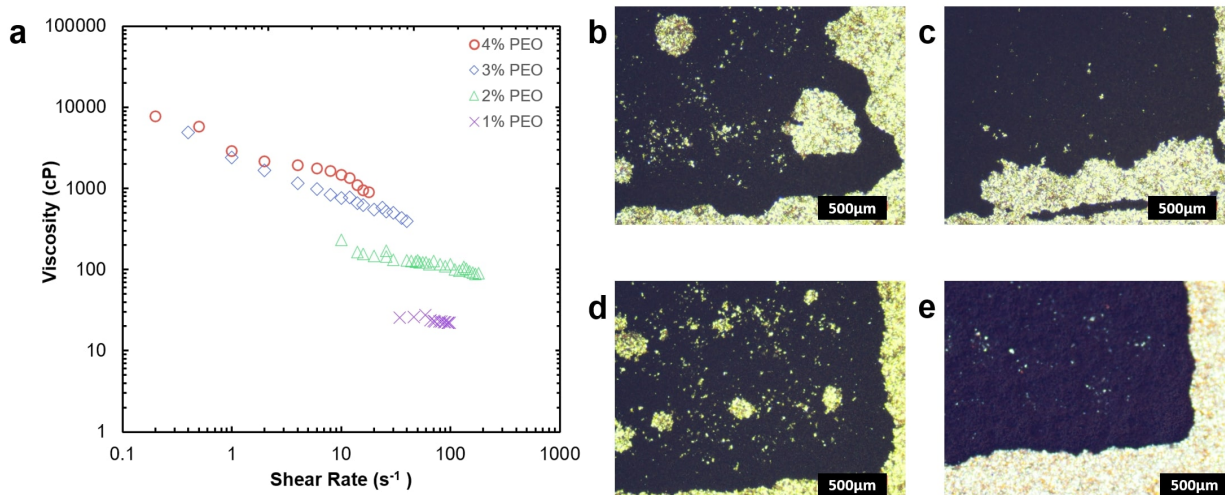
Figure 4.3: **Influence of ink viscosity on printed electrode quality].** **(a)** Plot of shear rate against viscosity for PEO binder at various concentrations. Optical microscope image of printed Ag2O film using **(b)** 1 % PEO binder, **(c)** 2 % PEO binder, **(d)** 3 % PEO binder, and **(e)** 4 % PEO binder. Printed features with the highest quality were obtained with inks printed with the 4 % PEO binder. The scale bar for the micrographs represents 500 μm.

printing, force is being applied by the squeegee on the ink (high shear rate), and the ink viscosity must be low to allow it to flow readily through the mesh of the screen. Once the squeegee has passed and the ink is sitting on the substrate (low shear rate), the viscosity must be higher so that the ink will maintain the definition of the printed feature. For general purpose screen printable inks, viscosity at no shear is in the range of 104-105 cP. Depending on which PEO binder concentration was used in the ink preparation, different print qualities were obtained. In screen printing, there are a variety of typical print defects. One of the most common defects is a lack of material in a small area on the printed film, called a pinhole defect. Another major defect, called delamination, is when the ink itself does not maintain adhesion to the substrate and pulls away from itself. Notable delamination was found in the lower concentrations, as well as a high pinhole density yielding high film roughness in the lower concentrations of PEO binder. However, the 4 % PEO binder yielded a relatively uniform single layer print and was used for all future Ag$_2$O ink preparations. From our measurements of these various binder concentrations, we can show that by increasing the concentration of binder we are generally able to improve the quality of the printed electrodes films. However, there are diminishing returns, as we can see that the binder viscosity plotted against shear rate does not increase drastically between 3 % - 4 %.
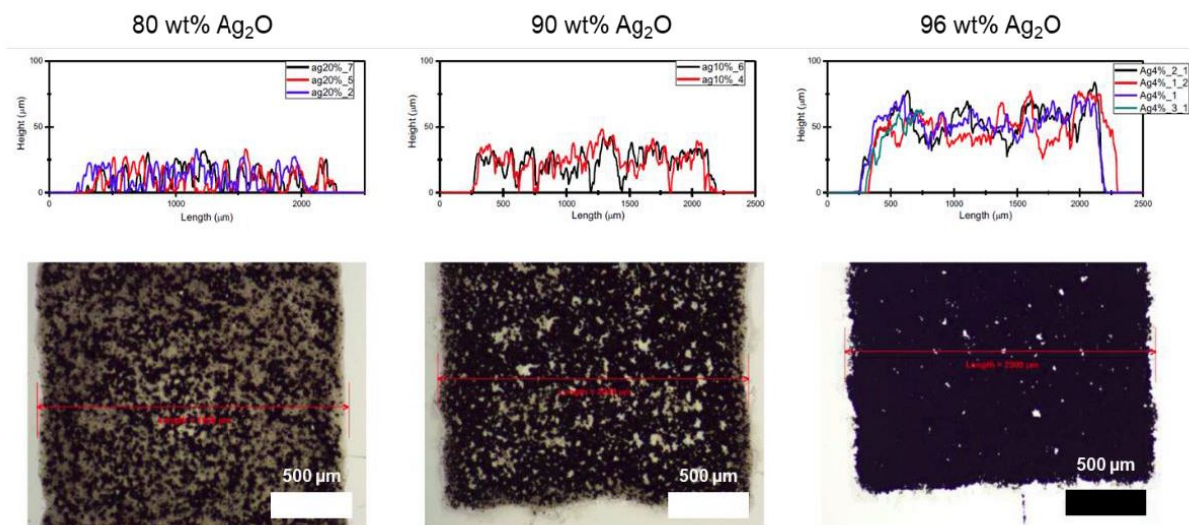
Figure 4.4: **Print quality of Ag$_2$O electrode films when varying mass loading of ink.** The scale bar of the micrographs represents 500 μm. Legends for each plot represent a different trial within the same experiment.

4.3.3 Mass loading

In addition to tuning binder viscosity, print quality of the electrode films may be tuned by varying the mass of the active material. As shown in Figure 4.4, it can be observed that printed films with 96 wt% Ag2O and 4 % binder solution results in film thicknesses of around 50 μm with fewer pinholes and print defects compared to inks with lower mass loadings. Similar experiments were done for Zn electrodes and it was found that the optimal mass loading for Zn consists for 1 % binder with 99 wt% of active material and 1 % binder solution. Film thicknesses of around 50 μm were also achieved for Zn electrodes in a single pass.

4.3.4 Film thickness

First, we wanted to validate the thickness uniformity of the screen-printed electrode arrays. To do this, we printed a 4 x 4 grid of each electrode on a glass substrate. For this particular experiment, the individual electrode dimensions were 5 mm x 5 mm, for an area of 25 mm^2. After printing the individual electrode arrays, each array was characterized for thickness. Both vertical and horizontal profilometry measurements were taken, and the average was reported. In Figures 4.5 and 4.6, the thickness mapping of each array is plotted. For the Zn films, the average thickness was 47.59 μm with a standard deviation of 2.29 μm, and for the Ag$_2$O films, the average thickness was 48.58 μm with a standard deviation of

2.26 μm. It should be noted that this particular experiment was done with a screen that had been used quite a bit already and may have degraded. The effects of screen quality degradation are discussed in a following section.

While tuning and optimizing the electrode ink compositions for screen printing, we were able to achieve thicknesses of approximately 50 μm for both Zn and Ag_2O films on a single print; by printing over the same layer multiple times, thicker, smoother, and less porous films are formed. Figure 4.7a and b show the profilometry of zinc and silver oxide films, depending on the number of print passes used to prepare the electrode. In order to deposit thicker electrodes, multiple screen-printing passes were used, letting each printed film dry at room temperature for 10 minutes before depositing the next. By depositing multiple layers of the same material, pinholes formed from the first layer were filled in, as well as yielding thicker electrodes films, with an average thickness of 120 μm for the zinc electrodes, and 70 μm for the Ag_2O electrodes. For Zn films, it is shown that the thickness of the film significantly improves with the number of print passes. The average thickness for Zn films after one, two, and three print passes are approximately 50 μm, 80 μm, and 120 μm, respectively. In comparison, the Ag_2O film thickness does not seem to increase significantly with additional passes. The average thickness for Ag_2O films after one, two, and three print passes are approximately 50 μm, 60 μm, and 70 μm, respectively. Despite multiple printing passes resulting in small changes in thickness, the primary benefit of printing multiple Ag_2O layers is to fill in pinhole defects in the films. As seen in Figure 4.8, the quality of the printed Ag_2O film improves drastically from one print to three print passes, with each additional pass filling in more pinholes in the layer below. Because of the improvements to film thickness and print quality, the battery arrays are fabricated using electrode films with three print passes.
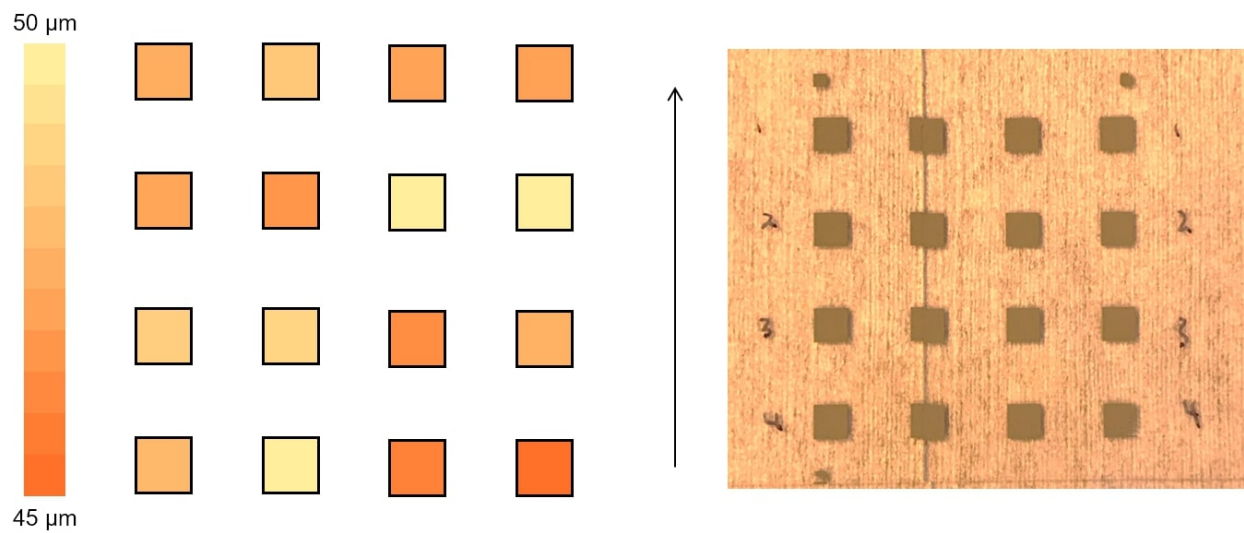
Figure 4.5: **Single-layer Zn electrode thickness characterization.** The average thickness was 47.59 μm with a standard deviation of 2.29 μm.

Figure 4.6: **Single-layer Ag$_2$O electrode thickness characterization.** The average thickness was 48.58 μm with a standard deviation of 2.26 μm.
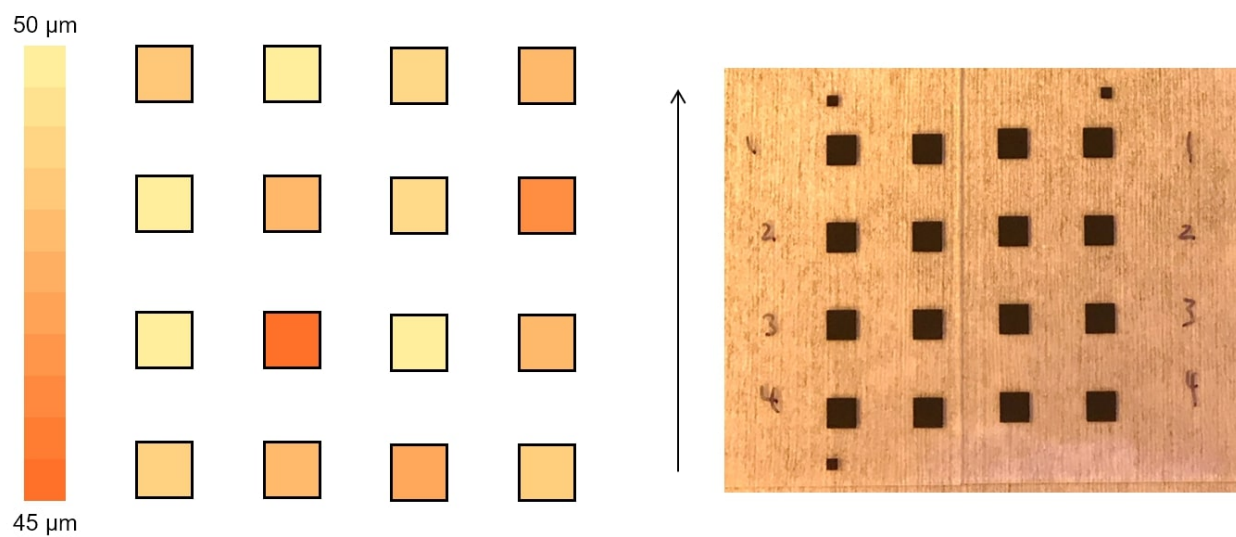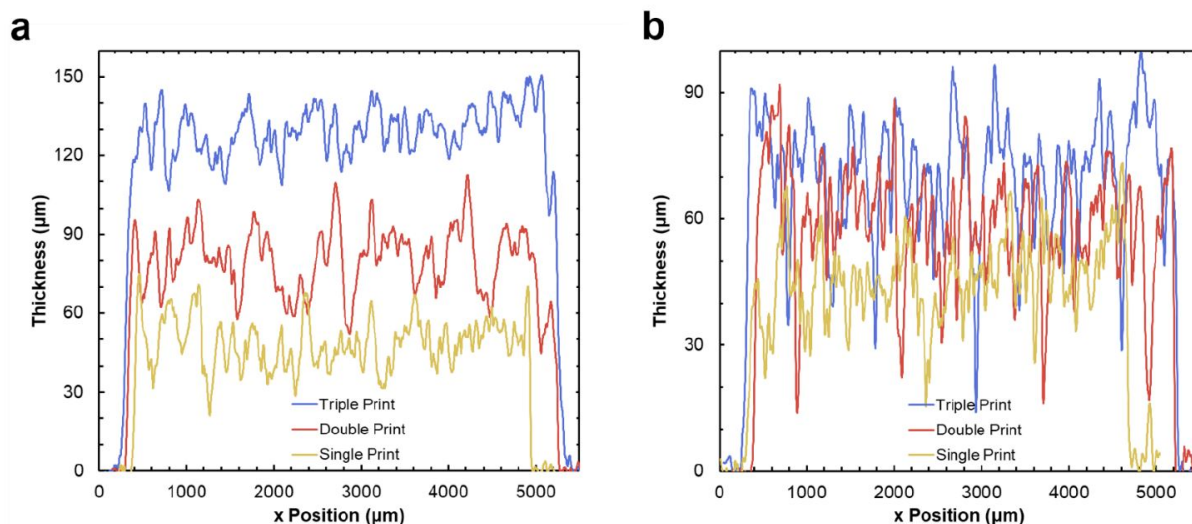
Figure 4.7: **Thickness characterization of multi-printed films.** (a) Profilometry measurements for screen-printed Zn films with varying number of print passes. (b) Profilometry measurements for screen-printed Ag$_2$O films with varying number of print passes.
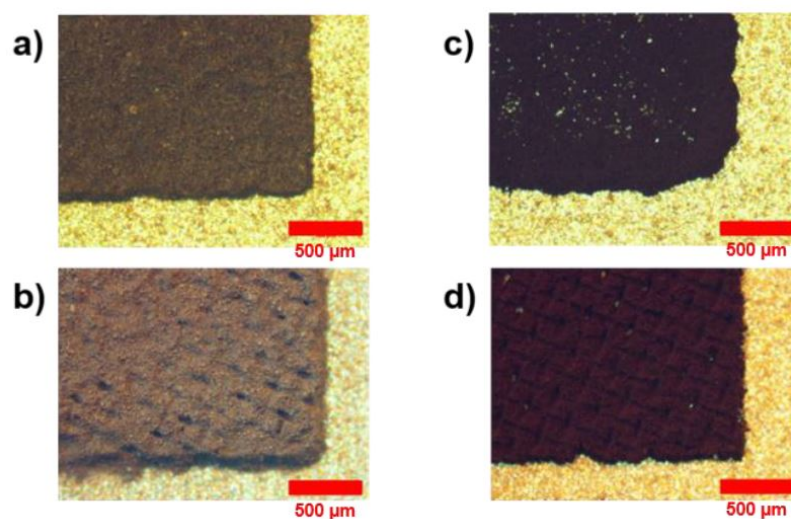
Figure 4.8: **Optical micrograph images of multi-printed films.** (a) Optical micrograph of a single printed Zn electrode. (b) Optical micrograph of a triple printed Zn electrode. (c) Optical micrograph of a single printed Ag$_2$O electrode. (d) Optical micrograph of a triple printed Ag$_2$O electrode. The scale bars in the micrographs represents 500 μm.

4.3.5   Screen quality

It was also observed that the quality of the printed electrode films was highly dependent on the quality and age of the screen. Even with the best maintenance, because of the large particle sizes of the electrode inks, the screen-mesh inevitably begins to clog with extended use resulting in rougher and thinner films with increased film defects, such as pinholes and incomplete transfers. As shown in Figure 4.9a, the average film thickness after a single-layer print of a Zn electrode is shown to decrease from 50 μm to 38 μm, and from 50 μm to 33 μm for Ag$_2$O films in Figure 4.9b. Due to the reduced film thickness, the effective mass loading of the inks is reduced as well; a numerical measurement for the mass loading may be determined by computing the area under the profilometry curve. The area under the curve after one pass decreased from 1.78e6 μm^2 to 1.67e6 μm^2 for Zn, and from 2.42e6 μm^2 to 1.33e6 μm^2 for Ag$_2$O. Therefore, one should take extreme care when cleaning the screens for the printed electrodes to maximize the lifetime of each screen, as well as ensure the printed film quality is maximized. Should the printed film quality and yield rate of the batteries begin to degrade, the screen will need to be replaced.

As part of the cleaning procedure to ensure the screen-mesh does not become clogged by solid material, we use both a solvent cleaning and physical cleaning process. After each individual printing pass, the screen is first soaked with ethylene. This is a preliminary solvent cleaning process to dissolve the binder and loosen and solid material. Afterwards, a dental water jet is used to gently scrub at the screen. Both sides of the screen are cleaned, and because of the water jet pulsing, the solid material is generally forced out of the screen-mesh. One should take care while scrubbing the underside of the screen, as the emulsion that forms the mask of the screen is deposited on this side. With too much force, the emulsion can be abrasively removed. In addition, selection of the emulsion material is key. Most commercial screen-printed inks use solvents to dissolve the inks, and as such their respective screen emulsions are solvent resistant and are generally not water resistant. In this work, the opposite is true. Because the inks are water based, we intentionally ordered screens with water resistant emulsions, and low solvent resistance.

4.4   Battery array characterization

4.4.1   Testing set-up

All experiments reported in the following sections were characterized with a Biologic BCS-810 battery tester. Prior to each measurement, an initialization step was done at 0.25 mA cm^{-2} for one minute. For the polarization measurements, each battery was discharged at a constant current density between 1 mA cm^{-2} and 8 mA cm^{-2} for two minutes. For the constant current discharge measurements, the battery was discharged at 0.2 mA cm^{-2}.
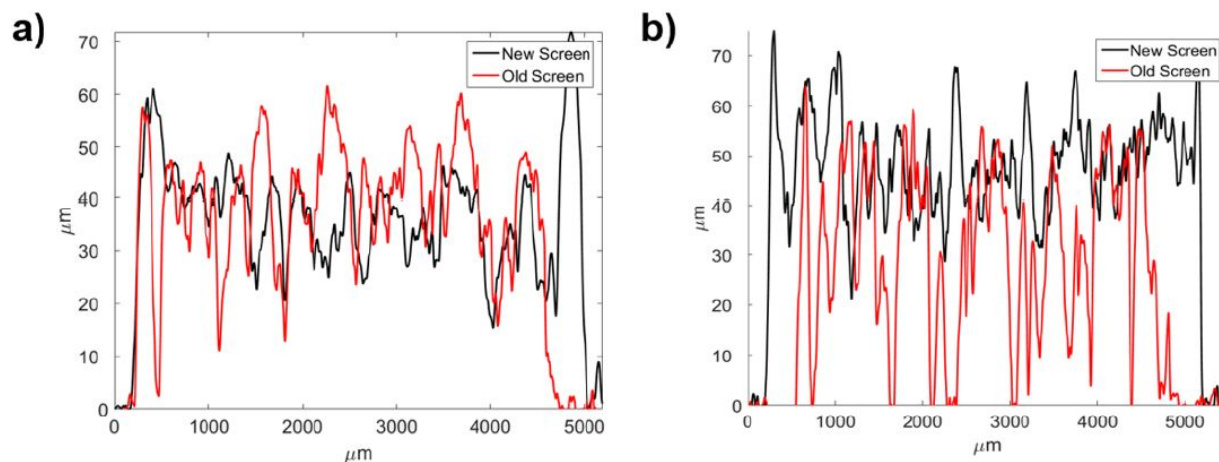
Figure 4.9: **Profilometry measurement of screen-degradation effect. (a)** Profilometry measurement for screen-printed Zn films after a single pass with a new screen and old screen. **(b)** Profilometry measurement for screen-printed Ag_2O films after a single pass with a new screen and old screen.

4.4.2   Single-cell performance

To evaluate the performance of the screen-printed batteries, single-cell batteries were first fabricated using screen printing methods and their performance was compared to our previous work using stencil printing techniques. Figure 4.10a shows the polarization data of the screen-printed cells. Cells were fabricated with 25 mm^2 electrode size and discharged at current densities ranging from 1 mA cm^{-2} to 12 mA cm^{-2}. It can be observed that the operating voltage decays slightly with increasing current density but maintains an operating potential above 1.4 V at current densities up to 12 mA cm^{-2} and has maximum power density of 17 mW cm^{-2}, which matches the results from our previous work on stencil printed batteries. The battery was also discharged at a constant current to determine its total areal capacity. Figure 4.10b displays the constant current discharge profile of the printed battery, which shows that the screen-printed cells can reach areal capacities of about 1.2 mAh cm^{-2}. In addition, it is shown that the standard deviations of the operating voltage and power densities are less than 50 mV and 200 mW cm^{-2}, respectively, which demonstrates the reproducibility of the screen-printed batteries.

4.4.3   Array performance

After screen-printed single-cell performance was established, screen-printed battery arrays were demonstrated. Using drop casted Ag interconnects between cells, batteries with array sizes of 2 x 1, 2 x 2, and 2 x 3 with electrode areas of 25 mm^2 were fabricated. As
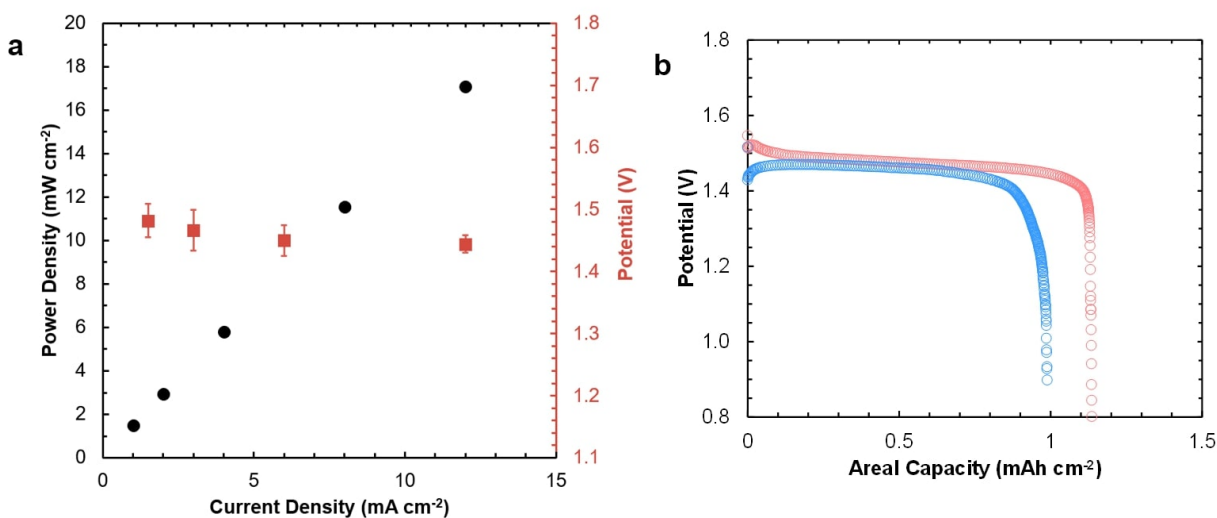
Figure 4.10: **Single-cell battery performance characterization.** **(a)** Single-cell battery polarization curve for a single 5 mm x 5 mm screen-printed Zn-Ag$_2$O battery at 2 mA cm^{-2}. **(b)** Single-cell battery discharge profile for a single 5 mm x 5 mm screen-printed Zn-Ag$_2$O battery at 2 mA cm^{-2}

shown in Figure 4.11, the operating voltages were shown to scale to an average about 2.95 V, 6.08 V, and 9.00 V for 2 x 1, 2 x 2, 2 x 3 array size batteries, respectively, which shows that there is little to no resistance introduced from the silver interconnects. It can be observed that the batteries maintain an operating potential above 2.9 V, 5.9 V, and 8.9 V at current densities up to 8 mA cm^{-2}, and have maximum power density of 17 mW cm^{-2}, 23 mW cm^{-2}, 72 mW cm^{-2} for 2 x 1, 2 x 2, 2 x 3 array size batteries, respectively. Like single-cell batteries, the operating voltage decays slightly with increasing current density and a small standard deviation for operating voltage (< 50 mV) and power densities (< 370 mV cm^{-2}) were observed. A side-by-side plot of the individual arrays is shown in Figure 4.12.
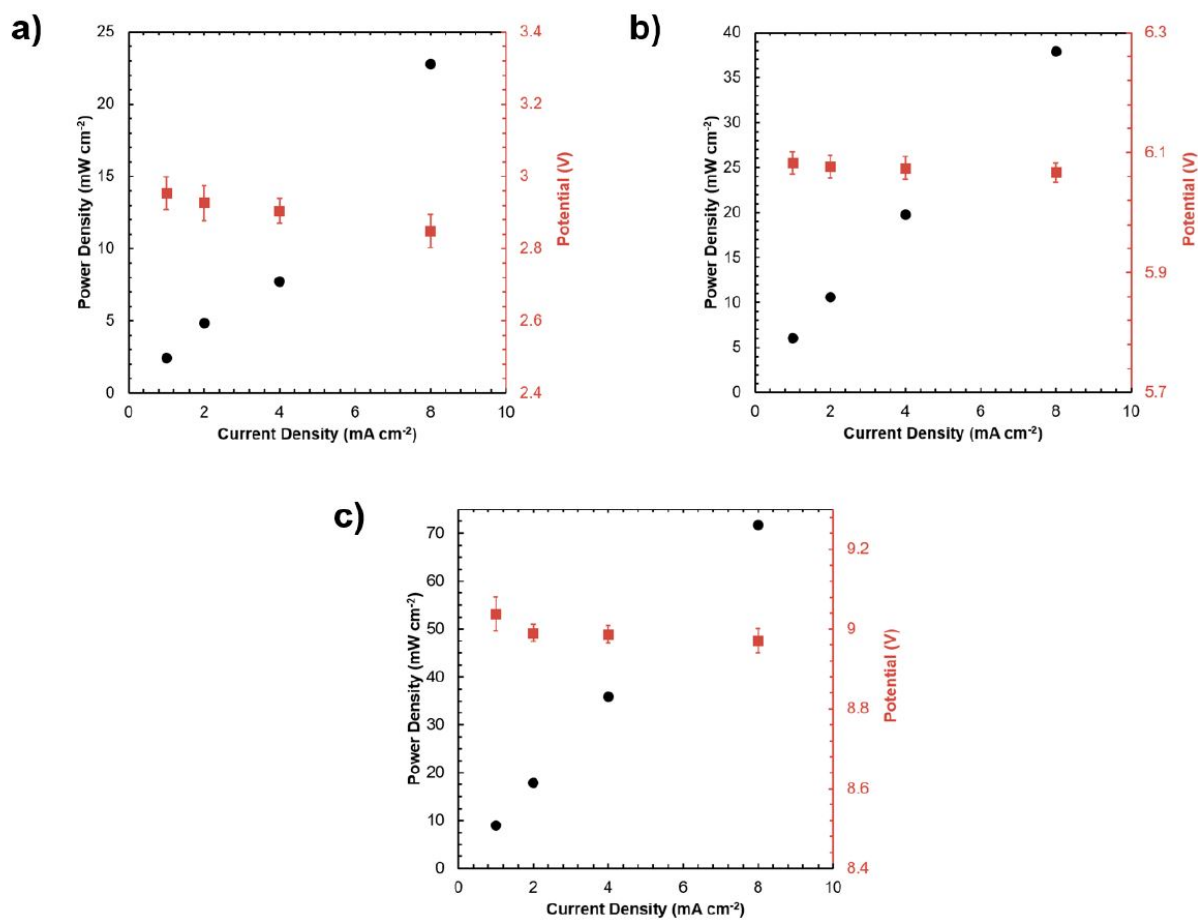
Figure 4.11: **Printed battery array polarization data for 2 x 1, 2 x 2, and 2 x 3 arrays.** Measured polarization data for Zn-Ag$_2$O battery arrays up to 8 mA cm^{-2} for **(a)** 2 x 1 arrays, **(b)** 2 x 2 arrays, and **(c)** 2 x 3 arrays.
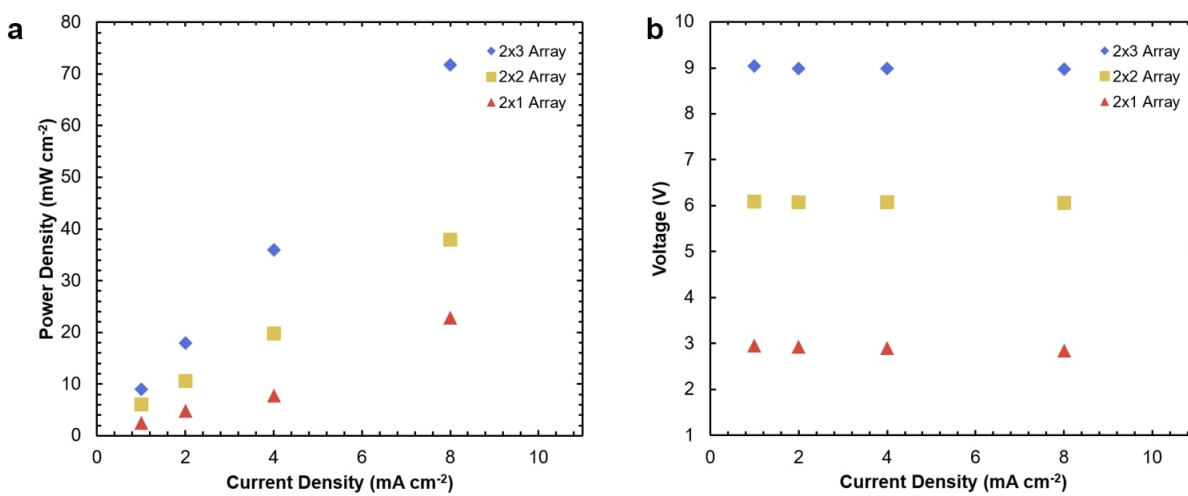
Figure 4.12: **Comparison of array electrical performance. (a)** Power density curve for 5 mm x 5 mm electrodes of various array dimensions. **(b)** Polarization curve for 5 mm x 5 mm electrodes of various array dimensions.

4.5 Chapter conclusions

In summary, we developed a printed battery array capable of achieving open circuit voltages at 1.5 V, 3 V, 6 V, and 9 V. By utilizing the vertical cell geometry and small footprint (0.25 cm^2) electrodes, the Zn – Ag$_2$O battery arrays we designed can be easily integrated into existing printing process flows. Using screen printing techniques, the current collectors, along with the anode and cathode electrodes are printed. By tuning the viscosity and mass loading of the electrode slurries, inks suitable for screen-printing were developed. Multiple print passes were done to increase the overall thickness of the film and improve print quality, such as reducing pinholes and surface roughness, to improve battery yield rate and capacity. With three print passes, we achieved Zn electrodes with average thicknesses of 120 μm and Ag$_2$O electrodes with average thicknesses of 70 μm. Battery arrays consisting up to six cells were fabricated and were able to maintain an operating voltage of 8.9 V at current densities up to 8 mA cm^{-2} and reach a peak power density of 72 mW cm^{-2}. Our work demonstrates the potential for scalable manufacturing of printed battery systems that can be integrated into miniature devices, while meeting high voltage requirements, such as IoT devices, biological devices such as BioMEMS, or wearable health monitoring devices.

4.6 References

[1] Brett Warneke, Matt Last, Brian Liebowitz, and Kristofer S.J. Pister. Smart dust: communicating with a cubic-millimeter computer. *Computer*, 34(1):44–51, 2001.

[2] Joseph M. Kahn, Randy Howard Katz, and Kristofer S.J. Pister. Emerging challenges: Mobile networking for "smart dust". *Journal of Communications and Networks*, 2(3):188–195, 2000.

[3] Yasser Khan, Donggeon Han, Jonathan Ting, Maruf Ahmed, Ramune Nagisetty, and Ana C. Arias. Organic multi-channel optoelectronic sensors for wearable health monitoring. *IEEE Access*, 7:128114–128124, 2019.

[4] Yasser Khan, Donggeon Han, Adrien Pierre, Jonathan Ting, Xingchun Wang, Claire M. Lochner, Gianluca Bovo, Nir Yaacobi-Gross, Chris Newsome, Richard Wilson, and Ana C. Arias. A flexible organic reflectance oximeter array. *Proceedings of the National Academy of Sciences of the United States of America*, 115(47):E11015–E11024, 2018.

[5] Margaret E. Payne, Alla Zamarayeva, Veronika I. Pister, Natasha A.D. Yamamoto, and Ana Claudia Arias. Printed, Flexible Lactate Sensors: Design Considerations Before Performing On-Body Measurements. *Scientific Reports*, 9(1):1–10, 2019.

[6] Maria R. Lukatskaya, Bruce Dunn, and Yury Gogotsi. Multidimensional materials and device architectures for future hybrid energy storage. *Nature Communications*, 7:1–13, 2016.

[7] Yasser Khan, Mohit Garg, Qiong Gui, Mark Schadt, Abhinav Gaikwad, Donggeon Han, Natasha A.D. Yamamoto, Paul Hart, Robert Welte, William Wilson, Steve Czarnecki, Mark Poliks, Zhanpeng Jin, Kanad Ghose, Frank Egitto, James Turner, and Ana C. Arias. Flexible Hybrid Electronics: Direct Interfacing of Soft and Hard Electronics for Wearable Health Monitoring. *Advanced Functional Materials*, 26(47):8764–8775, 2016.

[8] Ricardo E. Sousa, Carlos M. Costa, and Senentxu Lanceros-Méndez. Advances and Future Challenges in Printed Batteries. *ChemSusChem*, 8(21):3539–3555, 2015.

[9] Jolke Perelaer, Patrick J. Smith, Dario Mager, Daniel Soltman, Steven K. Volkman, Vivek Subramanian, Jan G. Korvink, and Ulrich S. Schubert. Printed electronics: The challenges involved in printing devices, interconnects, and contacts based on inorganic materials. *Journal of Materials Chemistry*, 20(39):8446–8453, 2010.

[10] Rajan Kumar, Kevin M. Johnson, Nicholas X. Williams, and Vivek Subramanian. Scaling Printable Zn–Ag 2 O Batteries for Integrated Electronics. *Advanced Energy Materials*, 9(13):1–9, 2019.

[11] Min Koo, Kwi Il Park, Seung Hyun Lee, Minwon Suh, Duk Young Jeon, Jang Wook Choi, Kisuk Kang, and Keon Jae Lee. Bendable inorganic thin-film battery for fully flexible electronic systems. *Nano Letters*, 12(9):4810–4816, 2012.

[12] Sheela Berchmans, Amay J. Bandodkar, Wenzhao Jia, Julian Ramírez, Ying S. Meng, and Joseph Wang. An epidermal alkaline rechargeable Ag-Zn printable tattoo battery for wearable electronics. *Journal of Materials Chemistry A*, 2(38):15788–15795, 2014.

[13] Abhinav M. Gaikwad, Gregory L. Whiting, Daniel A. Steingart, and Ana Claudia Arias. Highly flexible, printed alkaline batteries based on mesh-embedded electrodes. *Advanced Materials*, 23(29):3251–3255, 2011.

[14] Abhinav M. Gaikwad, Alla M. Zamarayeva, Jamesley Rousseau, Howie Chu, Irving Derin, and Daniel A. Steingart. Highly stretchable alkaline batteries based on an embedded conductive fabric. *Advanced Materials*, 24(37):5071–5076, 2012.

[15] Xiao Wang, Shuanghao Zheng, Feng Zhou, Jieqiong Qin, Xiaoyu Shi, Sen Wang, Chenglin Sun, Xinhe Bao, and Zhong Shuai Wu. Scalable fabrication of printed Zn//MnO2 planar micro-batteries with high volumetric energy density and exceptional safety. *National Science Review*, 7(1):64–72, 2020.

[16] Abhinav M. Gaikwad, Daniel A. Steingart, Tse Nga Ng, David E. Schwartz, and Gregory L. Whiting. A flexible high potential printed battery for powering printed electronics. *Applied Physics Letters*, 102(23), 2013.

[17] Rajan Kumar, Jaewook Shin, Lu Yin, Jung Min You, Ying Shirley Meng, and Joseph Wang. All-Printed, Stretchable Zn-Ag2O Rechargeable Battery via Hyperelastic Binder for Self-Powering Wearable Electronics. *Advanced Energy Materials*, 7(8), 2017.

[18] Thomas B. Reddy. *Linden's Handbook of Batteries*. Fourth edition, 2011.

[19] Kirt R. Williams and Richard S. Muller. Etch rates for micromachining processing. *Journal of Microelectromechanical Systems*, 5(4):256–269, 1996.

[20] Alla M. Zamarayeva, Akshaya Jegraj, Anju Toor, Veronika I. Pister, Cheryl Chang, Austin Chou, James W. Evans, and Ana Claudia Arias. Electrode Composite for Flexible Zinc–Manganese Dioxide Batteries through In Situ Polymerization of Polymer Hydrogel. *Energy Technology*, 8(3):1–9, 2020.

[21] Matthew Williams, Kirt R.; Gupta, Kishan; Wasilik. Etch Rates for Micromachining Processing—Part II. *Journal of Micromechanics and Microengineering*, 20(5):761–778, 2010.

[22] Kyle Braam and Vivek Subramanian. A stencil printed, high energy density silver oxide battery using a novel photopolymerizable poly(acrylic acid) separator. *Advanced Materials*, 27(4):689–694, 2015.

[23] Cher Yeoh*, Jonathan Ting*, Rajan Kumar, Donggeon Han, Vivek Subramanian, and Ana C. Arias. Screen Printed Zn-Ag2O Arrays for Integrated Electronics Arias * [+] C . Y . and J . T . contributed equally to this work . 2021. In preparation.

[24] Boualem Hammouda. Solvation Characteristics of a Model Water-Soluble Polymer. *Journal of Polymer Science*, 44:3195–3199, 2006.

[25] Thomas J. Hinton, Andrew Hudson, Kira Pusch, Andrew Lee, and Adam W. Feinberg. 3D Printing PDMS Elastomer in a Hydrophilic Support Bath via Freeform Reversible Embedding. *ACS Biomaterials Science and Engineering*, 2(10):1781–1786, 2016.

[26] David B. Kolesky, Ryan L. Truby, A. Sydney Gladman, Travis A. Busbee, Kimberly A. Homan, and Jennifer A. Lewis. 3D bioprinting of vascularized, heterogeneous cell-laden tissue constructs. *Advanced Materials*, 26(19):3124–3130, 2014.

[27] A. M. Reed and D. K. Gilding. Biodegradable polymers for use in surgery - poly(ethylene oxide)/poly(ethylene terephthalate) (PEO/PET) copolymers: 2. In vitro degradation. *Polymer*, 22(4):499–504, 1981.

[28] Woo Jin Hyun, Ethan B. Secor, Mark C. Hersam, C. Daniel Frisbie, and Lorraine F. Francis. High-resolution patterning of graphene by screen printing with a silicon stencil for highly flexible printed electronics. *Advanced Materials*, 27(1):109–115, 2015.

[29] Electrically conductive nickel ink. https://server.creativematerials.com/datasheets/DS_116_26.pdf.

Chapter 5

In-Mold Electronics

5.1 Introduction

Flexible, printed and hybrid textile electronics are at the forefront of novel electronic design. Printing techniques, including gravure, flexography and screen-printing, are widely exploited to produce functional films though recent developments in active thin film devices and are driving more complex assemblies such as OLEDs, flexible solar cells, electrochromic displays and consumer goods. Hybrid integrated electronics – printed electronics and inorganic components or textile substrates – add design flexibility and can offer unique performance characteristics specific to consumer electronics. However, certain surfaces are difficult to maintain truly conformal interfaces between printed flexible electronics and the surface. Depending on the surface complexity, it can be almost impossible to form a perfectly flush interface without wrinkles or folds in the substrate. How can we address the increasing design complexity of surfaces without detracting from the functionality of our printed electronics?

In-mold electronics (IME), the production process that integrates multiple substrates, printed electronic traces, soft membranes, microelectronic components and even textile interfaces is gaining increased interest because of technical and cost advantages including low capital costs, material utilization and rapid production. Thermoforming (also known as vacuum forming) is a critical process utilized in IME manufacture of complex parts. Currently the technology is driven by the automotive, control panel and instrumentation industries, with multi-material IMEs the current cutting edge of functional product development [1, 2]. Thermoforming is an enabler for IME; common in the packaging industry the process scales with both small and large part sizes. Thermoplastic sheet materials are often used as the substrate, the process temperature dictated by the polymer transition or melt temperature [3–5]. Thermoforming machines uniformly distribute heat to the plastic sheet – transfer to the part is dependent on the tool design. As the substrate is heated above its glass transition temperature, it becomes slightly pliable. While the substrate is pliable, it is forced over a mold, deforming the plastic greatly. Once the mold has completely been encased by the substrate, vacuum is drawn to pull the substrate into all of the contours of the mold. After

the substrate has cooled, one is left with a perfect shell of the mold, with all of the detailed contours the mold originally had. By combining this thermoforming process with existing printed electronics manufacturing techniques, functional 3D objects can be fabricated.

In the next section, I will outline and describe a work involving in-mold electronics, iMold. I will outline the design and fabrication process, and steps we took to ensure that the thermoformed electronics would maintain their electronic functionality. In addition, I will discuss a software assisted design approach, as well as the toolkit we developed, in order to help users develop in-mold electronics. Portions of this chapter are published in [6].

5.2   iMold: Enabling interactive design optimization for In-Mold Electronics

5.2.1   Design

The intuitive way to design in-mold electronics, starting from flat substrates to formed 3D objects, involves a few steps. In Figure 5.1, we can see the design process flowchart for conventional in-mold electronics. Starting from a mold design that we want to form a thermoplastic over, we can take some initial measurements to use as guidelines to approximate our 2D design. Using a tool like AutoCAD, we can sketch out the electronic component layout using the measured guidelines from our 3D mold. However, because there is no 3D visualization, we cannot determine what the electronic component layout will look like after thermoforming and any sort of deformation associated with it. One method to validate the design is to print out the 2D layout on paper and lay it over the mold to approximate where component may be positioned on the 3D mold [5–15]. Should there be any revisions that need to be made, they are done in a 2D design software and iteratively approximated on the mold. After settling on a design, the electronic layout is printed on the substrate and formed to the mold. Because there is no built-in alignment on the thermoforming tool, batch to batch variability can be high and there is some trial-and-error associated with the design process. This type of process is not ideal and can be further optimized with a software-assisted design process.

From Figure 5.2, we can see a proposed design process flow for software-assisted in-mold electronics. Starting with a design mold for the in-mold electronics, the software assisted components are depicted in dark green, where the original process flow is depicted in orange. Depending on if the mold design is too large to be modeled in one part or not, the software can split the part into multiple "slices" to improve the modeling accuracy and split up the computational load across multiple slices. After the mold has been properly rendered, the software develops a contour map based on the 2D to 3D mapping, and superimposes a gradient map of localized strain on both the 2D and 3D images. From here, the user can either import a .dwx file with drawn traces and pads for the electrical component layout, or draw them in manually on the design. If the user imports a design, there will be an auto-router feature, as most PCB software has a similar feature. After the electrical components have

been lain out, the software shows the user both the 2D and 3D generated structures, with the deformed electrical layout superimposed. Once the user has generated this view, they can edit the layout of the components in either the 2D or 3D perspective, with the opposite perspective being updated in real time. In addition to this, the user can set minimum tolerances on the interpolated resistance of certain traces after deformation, triggering warnings if they exceed a certain tolerance and prompting the user to reroute the layout such that they avoid regions of high local strain. Once the design is validated, the 3D layout is projected back to 2D based on the thermoforming deformation pattern, and a screen layout is generated [6].
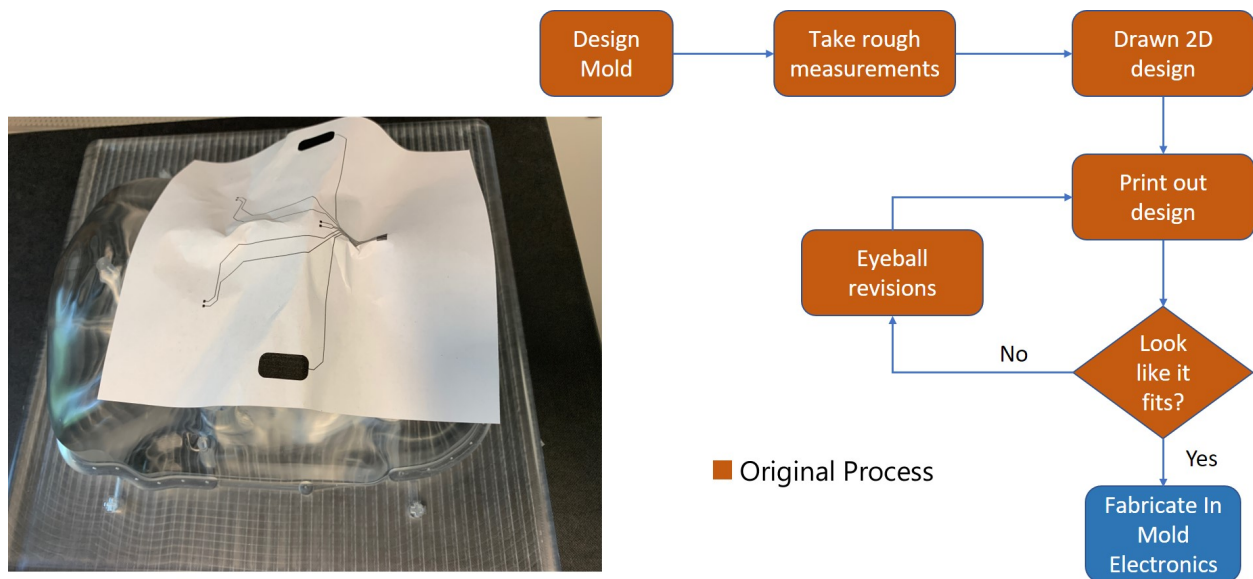
Figure 5.1: **Design process flowchart for conventional in-mold electronics.** Due to the lack of 3D visualization and confirmation, alignment and deformation of printed components is almost impossible to determine.
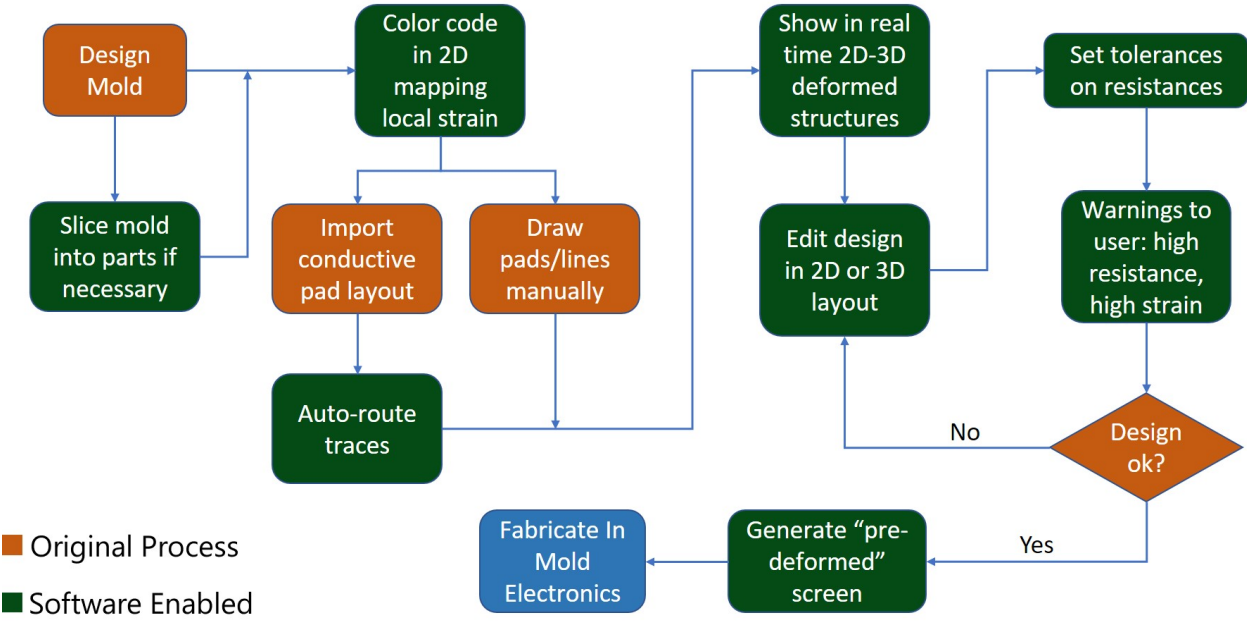
Figure 5.2: **Proposed design process flow for software-assisted in-mold electronics.**
With the additional of 3D visualization, as well as trace and component quality checks, the
design process gains reliability checks and users can validate designs prior to forming them.

```
Screen Print
Conductor/        Pick and                              Vacuum         Apply ACF
Dielectric   →    Place      → Encapsulate →            Form     →     and ribbon  →  Cut out part
(traces,          components                                           cable
pads)
```
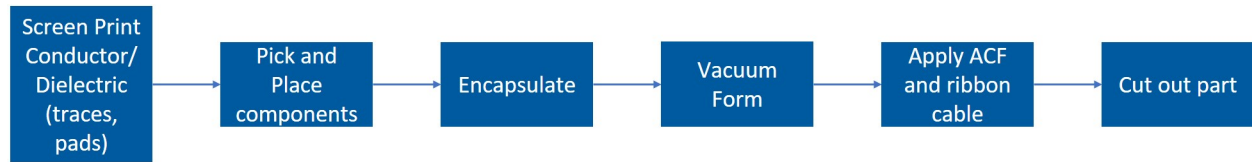
Figure 5.3: **Fabrication process flow for in-mold electronics.** Starting with the bare substrate, materials are screen-printed and dried. Any rigid components are then attached using a pick and place process, and then encapsulated. The substrate is then taking to be vacuum formed. After the part has been formed, connectors in the form of ribbon cables are attached with ACF. Finally the excess plastic is removed and the part is trimmed down to size.

After the screen layout is generated, the fabrication process is quite simple, seen in Figure 5.3. Starting with a thermoplastic substrate, the screen-printed materials are deposited onto the substrate. A commonly used substrate is Polyethylene terephthalate glycol (PETG), due to its low forming temperature. There are a variety of other materials, however one should be careful to note if the substrate is hygroscopic. Substrates that are hygroscopic absorb moisture at ambient and need to be pre-cured in an oven to remove any moisture before forming. Multiple layers of various materials can be deposited, and once they are fully cured, any solid state components can then be attached to the 2D substrate. A pick and place process is used for its simplicity and compatibility with larger substrates. Once all the components have been attached, they are then encapsulated by lamination with a thin film to apply vertical pressure to the components.

After all the components are attached, the 2D substrate with electronics on top can be vacuum formed. This process entails placing a mold inside of a thermoformer (Formech 686PT) [1, 16–19] and visually aligning the substrate above it. Once the heating elements have heated the substrate to an adequate temperature, the mold is raised into the substrate and vacuum is drawn. Anisotropic conductive films (ACF) are attached to the connectors of the substrate to interface with external electronics, and ribbon cables are applied to the ACF. Finally, the 3D component is trimmed using a dremel and the excess plastic is removed.

5.2.2   Screen-printing

One major challenge with in-mold electronics is ensuring that printed conductive traces do not crack during the forming process. Most conductive inks are silver microflake based, and are very prone to microcracking under low to moderate strain. Because of this, selecting an ink compatible with a thermoforming process is critical to ensuring the functionality of the electronics after the forming process. One such ink is Dupont ME603 [17], marketed as a screen-printable silver conductor specifically for in-mold electronics. Starting with a

12" x 12" x 1/8" PETG substrate (McMaster Carr), conductive ink is deposited using a screen-printing process (Ekra Semi-Automatic Screen and Stencil Printer).

Because of the low glass transition temperature of PETG, around 80 °C, annealing the screen-printed inks is not so trivial. The recommended anneal temperature for Dupont ME603 is 120 °C for 20 minutes in a box oven, however should the PETG substrate be exposed to this temperature prior to vacuum forming, it would deform during the ink curing process and lose structural integrity. Because of this, printed inks were cured at 70 °C for 2 hours minimum. Even at this lower temperature, the ME603 ink can fully cure due to its solvent fully evaporating during the curing process. In addition, the PETG substrate maintained its initial dimensions prior to annealing. When removing the substrates from the oven, it is recommended to apply a vertical pressure with a heavy metal plate such that while the substrate cools it does not curl up from uneven cooling. Doing so will yield a flat substrate with a properly cured layout printed on top.

5.2.3 Component attachment

To attach solid-state components to the printed PETG substrates, a pick and place process was used to ensure precise alignment as well as reliable contacts between placed components and their respected printed pads and traces. Here, we used a multi-prupose die bonder (Finetech FINEPLACER pic ma). In order to reliably attach the components to their respective pads, a few additional materials were used for both electrical and structural integrity. A cross sectional view of a surface mounted device (SMD) is shown in Figure 5.4. Starting from the PETG substrate with printed silver, we see that there is a conductive epoxy directly on top of the pads for the surface mounted device. This conductive epoxy functions both as an adhesive as well as a conductive interface between the printed traces and the surface mounted device [18]. We chose to use the Dupont ME902 conductive silver epoxy for it's compatibility with the Dupont ME603 printer silver traces. In addition to the silver epoxy, a structural epoxy (Loctite 3621) [20] was deposited in between the conductive pads such that it would make connection to the bare package of the surface mounted device. This functions as both a structural adhesive binding the package to the substrate, as well as a dielectric to prevent inter-pad shorting. By replacing the pick and place tool tip with a needle, small drops of both the conductive and structural epoxy and be precisely deposited on the printed PETG substrate using a pin-transfer method. After pin-transferring these two materials, the surface mounted devices were placed, using the pick and place tool, in their desired locations. The structures were then cured for 2 hours at 70 °C in a box oven. After cooled, an additional polyurethane (PU) film from Dupont Intexar is laminated at an elevated temperature of 120 °C over the surface of the surface mounted devices. This functions as a protective covering, and also applies a vertical strain down onto the SMDs, ensuring they remain in place. Because the film laminator applies high temperature for a short period of time, on the order of a few seconds, the PETG substrate does not deform significantly and can be continued to use for the remaining processes.
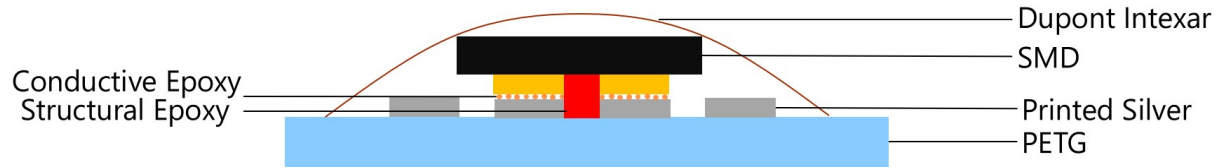
Figure 5.4: **Cross sectional view of pick and place attached component.** Surface mount components can be easily attached to the printed silver traces on a flat substrate. First, a conductive epoxy is pin-transferred onto the conductive silver pads. An additional structural epoxy is placed in between the pads with the same pin-transfer method. Using the pick and place tool, the SMD is aligned and attached to the printed pads. Finally, a top encapsulation layer (Dupont Intexar) is laminated to apply vertical pressure to the component.

5.2.4   Vacuum forming

In order to form the printed PETG substrates over a part, we needed to design various molds to test. Using Solidworks, as well as some 3D scans of objects, we were able to generate a variety of different molds seen in Figure 5.5. Figure 5.5a and b show the mold of an Xbox controller, used for a demonstrator discussed later in this section. Similarly, Figure 5.5c, a mold for a mask, is discussed later. Figure 5.5d shows a mold designed as a challenge structure for the vacuum forming process. There is a hemisphere, pyramid, cylinder, and wavelike structure on this mold. A screen was designed with surface mounted LEDs at various curvature points on each of the structures, and the individual LEDs were evaluated before and after the forming process to ensure proper functionality [20–31]. All of the molds were fabricated with a computer numerical control (CNC) router, all made out of acrylic. The choice of material for the mold is quite important. Depending on what material it is made from, the thermoforming process can damage the mold itself. An ideal material is wood due to its low thermal conductivity, however a variety of other materials could be used such as acrylic and other resin based materials. For this work, we chose to use acrylic because of its abundance, however it should be noted that with repeated forming with the same mold, the mold can begin to heat up and affect the forming quality of the part. It should also be noted that it is helpful to place the molded part up and away from the surface of the mold stage. For all of the molds shown here, there was a one inch "plate" included in all of the designs such that the formed part could be easily removed from the mold.

An additional challenge with molds is air venting. Because part of the thermoforming process requires drawing vacuum, the mold should ideally allow some sort of airflow, depending on the complexity of the part. If the part has a large number of contours, such as the one shown in Figure 5.6, one may choose to add additional venting holes to the part. It is recommended to make these holes as small as possible on the molding surface, and expand them in the back of the part, as large as 5 mm diameter, as to maximize airflow. In

addition, hollowing out regions behind densely populated air holes can improve the airflow. Finally, adding venting lines connecting various vent regions is recommended to improve airflow uniformity.

In this work, we used an industrial standard thermoforming machine (Formech 686PT). The machine is preheated at 70% power for 20 minutes prior to starting any process [2–6, 8–15, 32–41]. After the mold has been loaded into the tool, we raise the mold stage as close to level with the substrate loading stage as possible. This allows us to visually align the PETG substrate to the mold, and slowly drop down the mold stage until the substrate can be clamped in place. Once the substrate and mold have been aligned, the heat cycle is performed at 70% for 80 seconds, with all heating elements enabled. After ensuring the substrate is sufficiently pliable, the mold is raised into the substrate and vacuum is drawn for 10 seconds. The samples are then cooled in ambient for 20 seconds before purging the part from the mold using the pulse function for 10 seconds.

5.2.5 Trace strain and conductivity

In order to predictively model how the electrical performance of printed traces change during the forming process, a calibration curve of strain vs. trace resistance must be characterized. To effectively determine any trends, a screen layout was designed with a variety of test structures, shown in Figure 5.7a. Traces of varying thickness, but fixed length, were printed on a stretchable substrate, Dupont Intexar. In addition to these test structures, the connector for the printed electronics was also printed, in both vertical and horizontal orientations, to test when an attached connector would disconnect from the traces at various strains. Finally, pads for surface mounted components were also printed, again in both orientations, to evaluate the strain when surface mounted components would delaminate. These components were attached with the process outlined above, and were designed for an 0603 (imperial) package size. It should be noted that this package size determines the separation in the printed pads, and a larger component is on average more susceptible to delamination compared to a smaller component [20, 27–31, 42].

The screen-printed silver was then cured using the same 70 °C for 2 hour process, to ensure the same conductivity as the devices under test on PETG. The Intexar substrate was then stretched to various strain levels, and the resistances of the horizontal traces were then measured, shown in Figure 5.7b. The resistance of a trace that was no longer conductive was marked as "0" and the plot of the strain vs. normalized resistance of traces is shown in Figure 5.7c. As we can see, there is a general trend correlating the point of failure for the traces with the thickness of the trace. As we decrease the thickness of the trace from 1000 μm to 250 μm, we see the thinner traces fail catastrophically at an lower strain value than the thicker ones. In addition, an exponential fit is shown superimposed on the measured 1000 μm strain vs normalized resistance curve, with an R^2 value of 0.98.
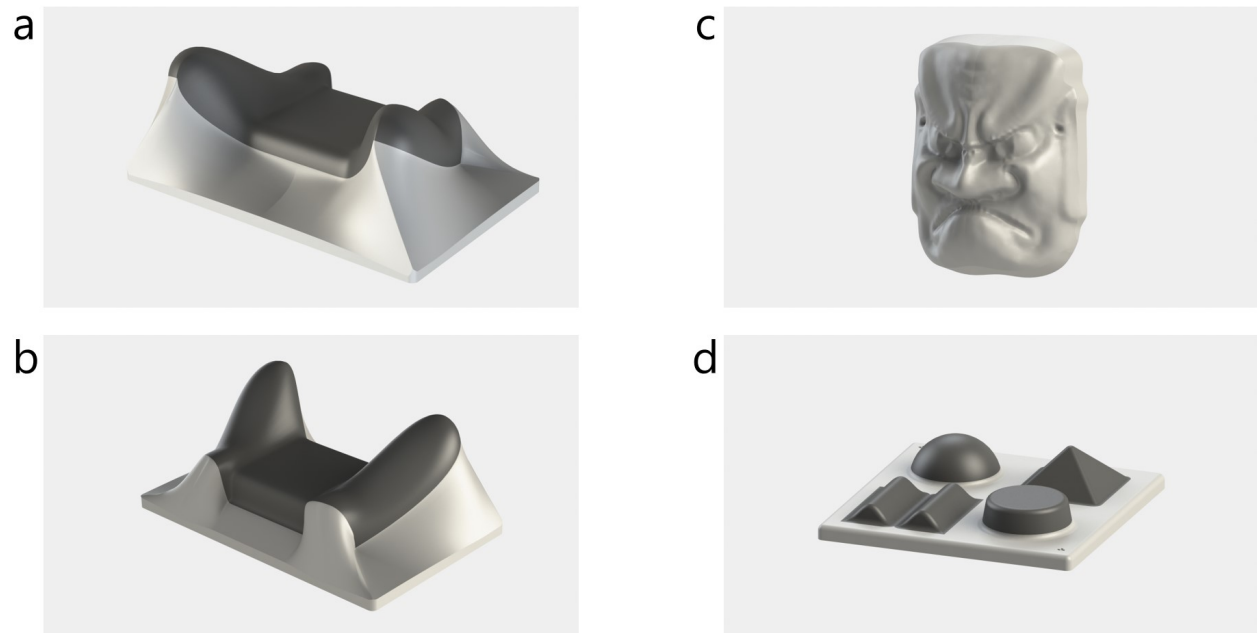
Figure 5.5: **Various molds used for forming in-mold electronic components. (a)** and **(b)** are two views of the underside of an Xbox controller. **(c)** is a mask mold and **(d)** is a test platform with various test structures of scaling difficulty to test the compatibility of vacuum forming with different geometries.
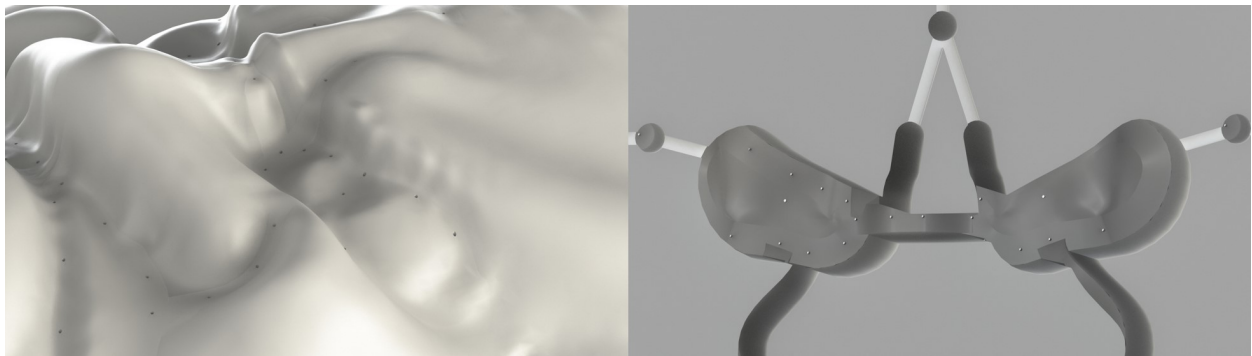
Figure 5.6: **Close-up view of mask mold eye contours with venting scheme.** Because the eye regions on the mask mold have high concavity, the vacuum of the thermoformer cannot pull down the substrate far enough into the cavity on its own. By adding an additional venting scheme on the backside, with connected airflow, the part forming is significantly improved.
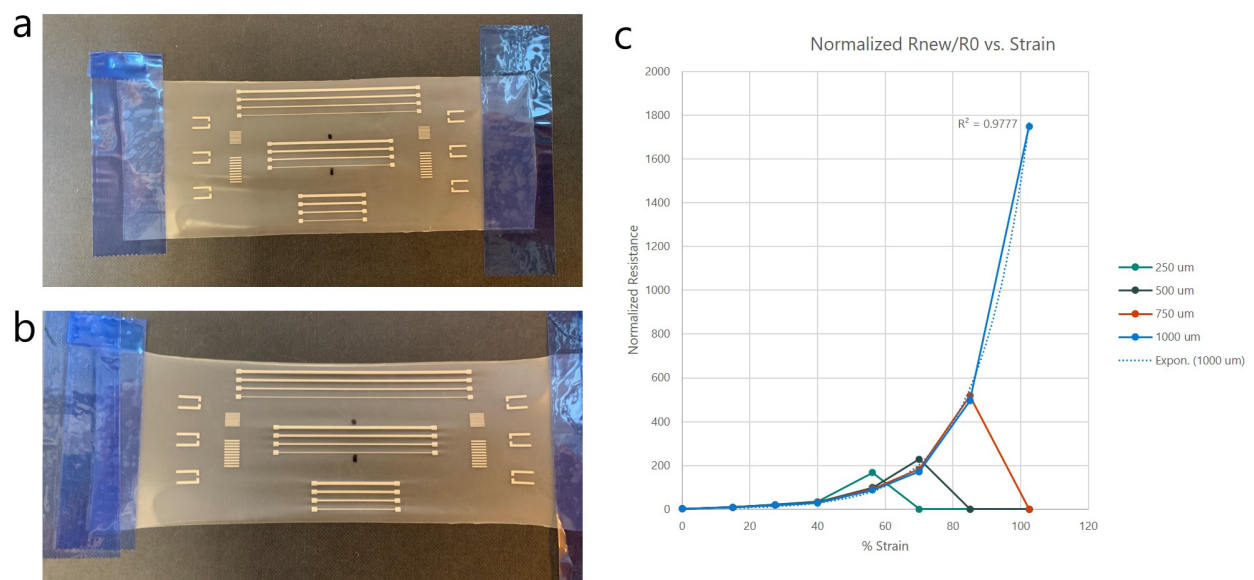
Figure 5.7: **Printed conductive trace strained conductivity characterization. (a)** Printed silver test structures on unstrained Dupont Intexar substrate. **(b)** Printed silver test structures on laterally strained Dupont Intexar substrate. **(c)** Strain vs. normalized resistance curve for printed silver traces of various thickness. As the trace thickness decreases, the traces fail catastrophically at lower values of lateral strain. An interpolated exponential relationship for a 1 mm thick trace is shown as a dotted line.

5.2.6   Computational design toolkit

We developed a computation design toolkit for interactively customizing the functional electronics patterns and detecting conductivity failures. In Figure 5.8, you can see the rough workflow of the software toolkit. Starting with a calibration mesh, we establish a mapping between the 2D printed substrate and the 3D formed shape via a geometry based simulation [2–4, 32–38]. In order to obtain a material dependent shape parameter involved in the mapping, we conducted a calibration onto a preset test mold. The shape parameter will remain the same if the substrate material is predetermined. With the established mapping, we provide users a set of interactive tools for placing connectors and semi-automatically generating the traces linking pins of connectors. Another import function we provide is the conductivity failure detection. Since there is large distortion introduced in regions with high curvature during the forming process, the conductivity in these regions could be increased dramatically and cause electrical functionality failure. Therefore it is important to detect such a failure and notify users to make adjustment to the trace [5, 6, 8–15, 39–41].

The idea of a 2D-to-3D mapping is inspired by a local/global parameterization approach for 3D regular surfaces. On a given 2D pattern D and its corresponding 3D shape S, each of the triangles t_d on D can be mapped onto its corresponding triangle t_s on S locally. We assume throughout the process, there is no self-intersection that can occur, which means that any of two triangles on the formed surface S will not intersect with each other. With this assumption, two types of transformations are introduced in the mapping, including a rotation and scaling [3]. The rotation represents the rigidity of the deformation during the process, while the scaling mimics the flexibility of the material. For each triangle t_d, the rotation and scaling are represented as matrix forms R_t and W_t. In the thermoforming process, it is not possible to only have rotation or scaling, and instead we combine the two transformations together and form a new transformation matrix T as

$$T_t = (1 - \alpha) \cdot R_t + \alpha \cdot W_t \tag{5.1}$$

where α is a scalar shape parameter to control how much the shape will be introduced in the forming process. α is material dependent as thinner materials are usually more flexible and have larger deformation, and vice versa. To obtain α for certain materials, we conduct a calibration, which is detailed below. Both R_t and W_t can be computed with the three vertices of triangle t_d on D and the vertices of t_s on S using a Singular Value Decomposition (SVD). The combined transformation matrix T_t is considered as the target transformation for each of the triangles t during the forming process. The actual transformation is expected to follow the target T_t, and can be computed by minimizing the objective function $E_{mapping}$ as follows:

$$E_{mapping} = \sum_{t=1}^{f_n} |||X_t - T_t|||_F^2 \tag{5.2}$$

where f_n is the total number of the triangles on D, T_t is the target transformation matrix for triangle t, X_t is the unknown transformation for t, and the $||| \cdot |||_F$ is the Frobenius norm. As $E_{mapping}$ is in the quadratic form, this optimization problem can be solved as a linear least-squares problem by solving a series of linear equations.

The shape parameter α depends on physical factors of the substrates, such as the Young's modulus of the substrate material, the Poisson ration, and the thickness of the substrate. To accurately establish a physical-mathematical model of the substrate based on the mechanics and Finite Element Analysis (FEA) is challenging and inefficient. Instead, we borrow the idea from [3] and conduct a series of experiments based calibrations. One test mold was a pyramid structure, shown in Figure 5.9. A 1mm x 1mm square grid was printed onto PETG using an ink transfer method from a laser printer. The printed grid was then scanned with a 3D scanner prior to and after thermoforming onto one of the calibration molds, shown in Figure 5.10. This process was then repeated with the other calibration mold. With the scanned 2D substrate data and the 3D formed data, we are able to compute the α from them. The computed $\alpha = 0.2143$ is fixed and used throughout all the tested examples.

Based on the 2D to 3D mapping, we developed a sequence of interactive tools for the user to define traces on the 2D substrate and preview the resultant 3D traces simultaneously. We adopt the styling curve as the representation of traces. The styling curve consists of a series of attribute nodes with not only position information, but also the triangular mesh connectivity information on the D. Since the triangular mesh connectivity of S is the same as the one for D, the defined styling curve can be instantaneously mapped onto S. There are two different types of the attribute node, the attribute edge node p_{edge} and the attribute face node p_{face}. Therefore, the position p_{edge} can be calculated by interpolating the two endpoints (p_1, p_2) of a triangular edge. Similarly an attribute face node is associated with a triangular faced with barycentric coordinates (u, v, w), where $u, v, w > 0$ and $u + v + w = 1$. Also its 3D position is calculated by interpolating the three vertices $(p_1, p_2, and p_3)$ of the triangular facet. Once the styling curve is defined on a 2D substrate, a 3D curve is obtained instantaneously based on the established 2D to 3D mapping.

Built upon the styling curves attribute nodes, we developed the curve creation and editing tools. Via the mouse left clicks, a set of points are picked as the control points. These control points are used to generate a smooth curve automatically by interpolating these picked points via the four-points interpolation scheme as follows:

$$c_i^* = -\frac{1}{16}c_{i-1} + \frac{9}{16}c_i + \frac{9}{16}c_{i+1} - \frac{1}{16}c_{i+2}, \tag{5.3}$$

where c_{i-1}, c_{i+1}, and c_{i+2} are the four sequencing control points and c_i^* is inserted between c_{i-1} and c_i. After repeating the four-points interpolation several times, more and more points will be inserted to the styling curve and the styling curve becomes smoother and smoother.
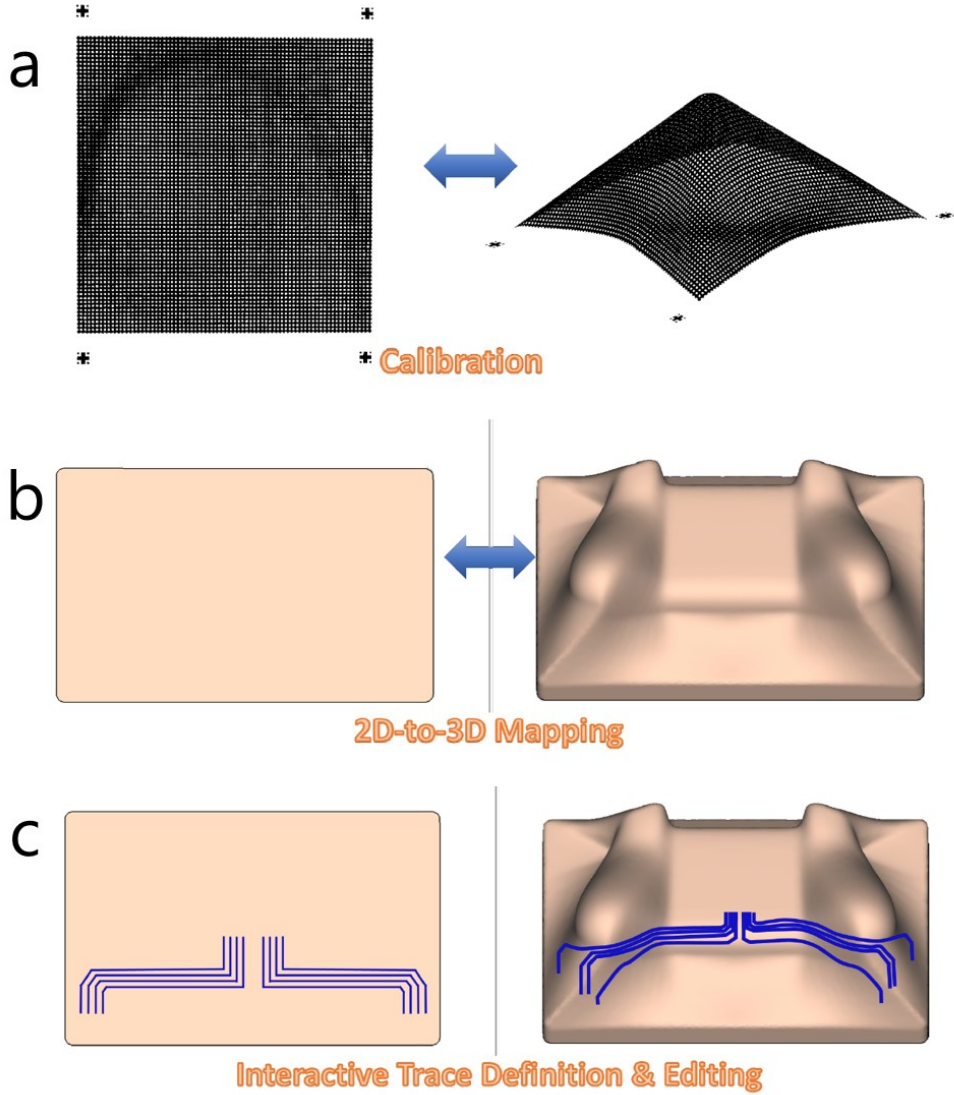
Figure 5.8: **Software toolkit for in-mold electronics.** **(a)** Calibration meshes are inputted into the software toolkit and used as a transformation matrix. **(b)** The mold design is fed into the toolkit and the 2D to 3D mapping of the mold is generated. **(c)** Interactive trace definition and editing. Users can draw designs on both the 2D and 3D renders and see the designs visualized in both dimensions in real time.

Figure 5.9: **Pyramid and hemisphere molds used for software calibration.** Two test structures were developed and used to calibrate the software toolkit.
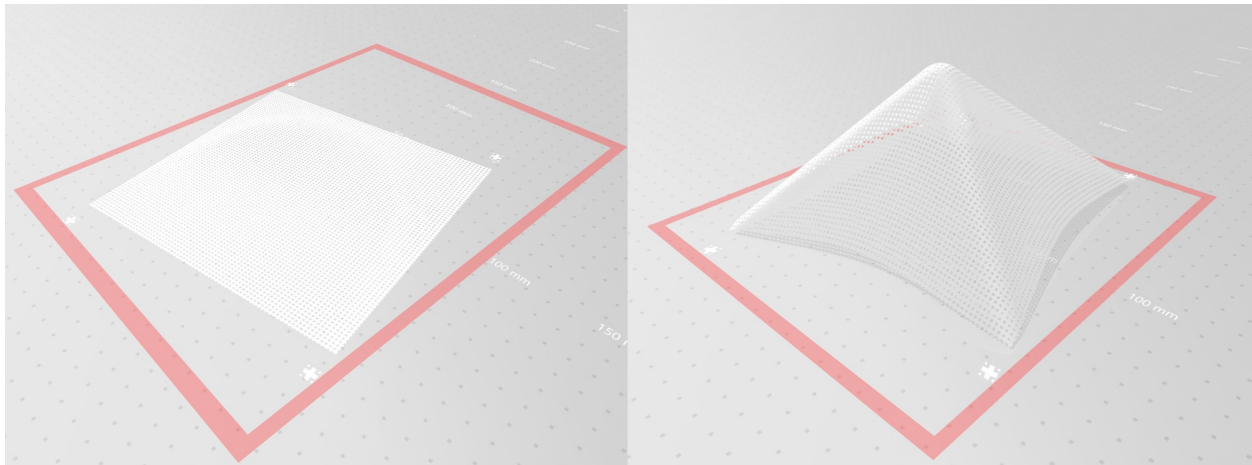
Figure 5.10: **3D scanned mesh calibration technique.** A 1 mm x 1 mm grid pattern was printed and transferred onto a flat PETG substrate and scanned using a 3D scanner. The substrate was then formed onto the calibration molds and re-scanned using the 3D scanner. The unformed and formed meshes were then used as calibration inputs to the software toolkit.

Figure 5.11: **Xbox controller in-mold electronics demo. Green:** Printed silver capacitive touchpads. **Blue:** Surface mounted thermistors. **Orange:** Surface mounted LED.

5.2.7   Applications

To interface the printed electronics on the PETG substrates with external electronics, we employed a flexible flat cable (FFC). An anisotropic conductive film was applied to the surface of the printed traced and the FFC. Then we applied heat and pressure for bonding, and Kapton tape was added over the bonded region as an additional securing mechanism. With this new FFC, we could connect the printed electronics to a microcontroller on external circuitry. We used an Arduino Uno and various other components on a breadboard to interface the printed and rigid components. Using this setup, we were able to realize two different demos.

One demo involves the Xbox controller molds from Figure 5.5a. The idea was to design an overmold that was able to characterize the quality of grip the user had on the controller. By placing single pad terminated traces on the grips, as well as surface mounted thermistors, the overmold can measure how many pads are being touched as well as the temperature of each palm. In addition, depending on the number of pads in good contact with the skin, a surface mounted 0603 green LED increases its brightness with increasing number of contacted pads. The schematic of the demo is shown in Figure 5.11. The capacitive touchpads are shown in green, fabricated from single layer screen-printed silver. The SMD thermistors are shown in

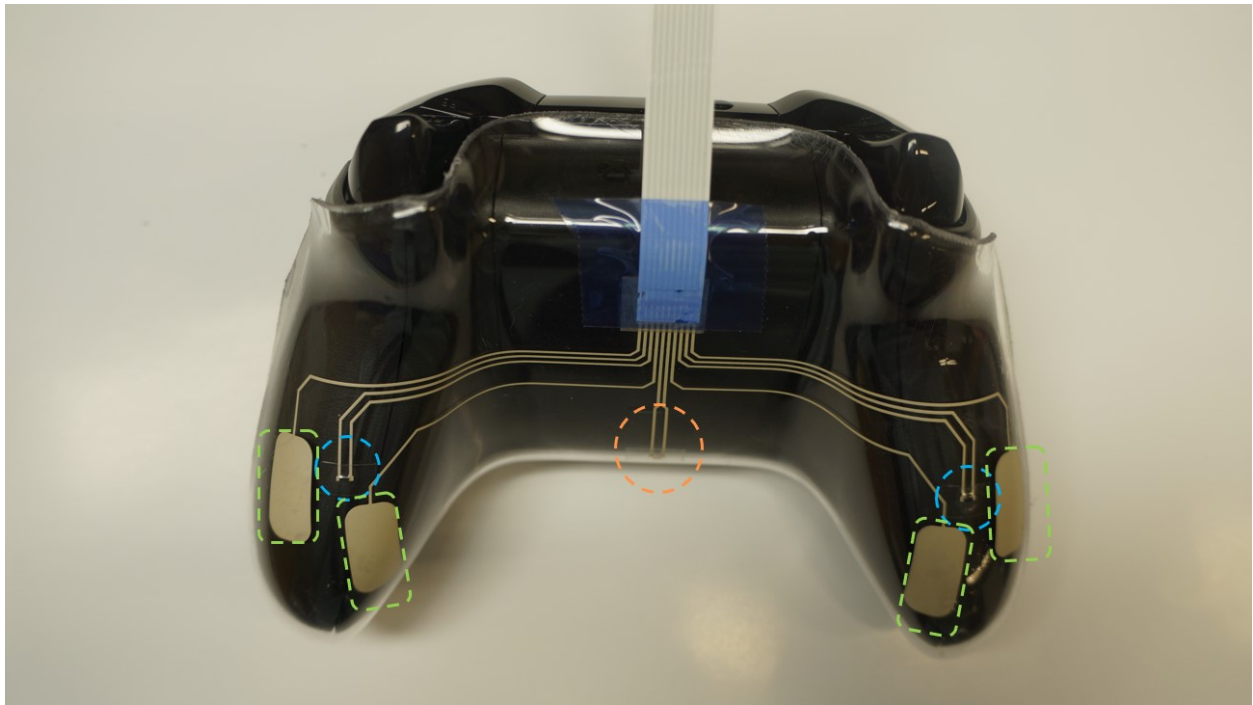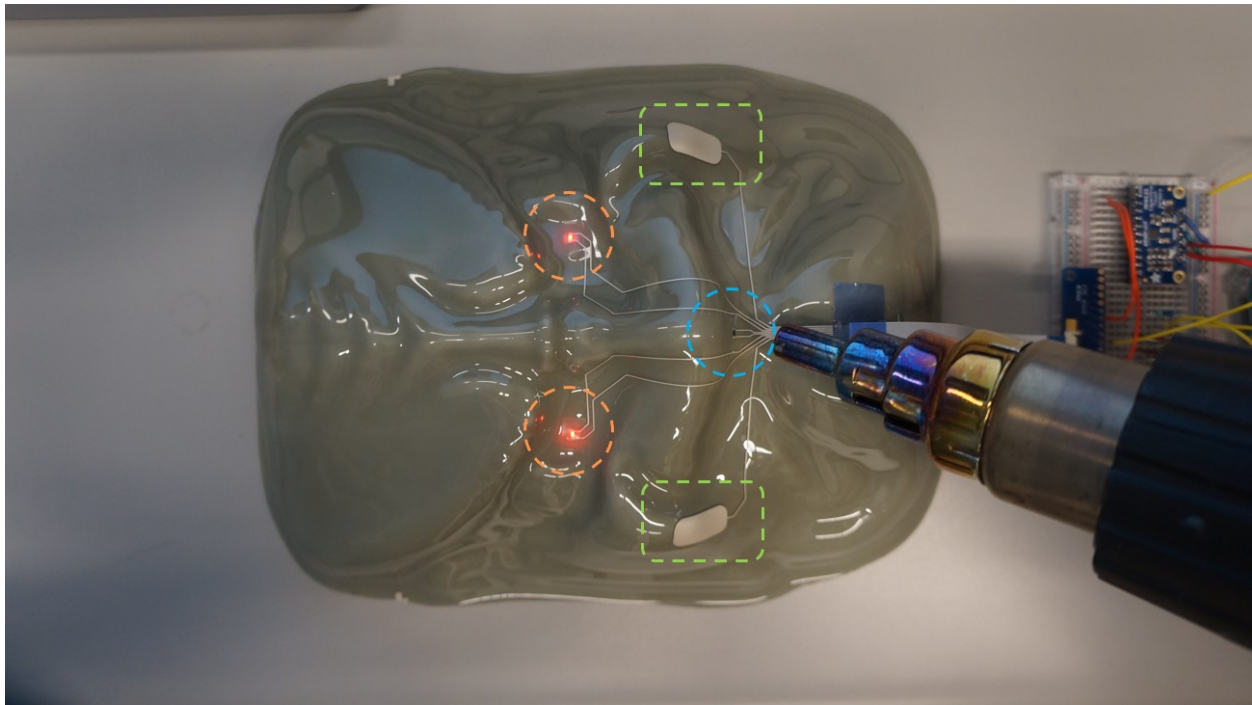Figure 5.12: **Mask in-mold electronics demo. Green:** Printed silver capacitive touch-pads. **Blue:** Surface mounted thermistor. **Orange:** Surface mounted LEDs.

blue, and the SMD LED is shown in orange.

Another demo involves using a mold from Figure 5.5c, a mask. This was motivated by designing a Halloween-type mask that can sense change the external appearance of the "eye" LEDs based on a few inputs. In Figure 5.12, we can see there are two SMD LEDs shown in orange, and a SMD thermistor shown in blue. In addition, there are single pad terminations for each cheek, acting as capacitive touchpads as well. Functionally, this mask behaves in the following manner: when either of the capacitive touchpads are tapped, the eye LEDs turn on. These LEDs can be toggled on or off by pressing the touchpad again. The thermistor on the nosepiece constantly reports the temperature, and as the user exhales, there will be a local increase in temperature. As the temperature increases, so does the brightness of the eye LEDs.

5.3 Chapter conclusions

In this chapter, we discuss IME as a possible solution to realizing functional electronics for highly complex interfaces. In addition, we present iMold, a novel software-guided IME process that enables interactive design optimization. We developed a computational design

toolkit to perform interactive customization of electronic patterns while optimizing given design with electrical failure detection. Moreover, we show a full IME process from design, fabrication and components assembly by embedding an automatic surface-mounting process before vacuum forming. Specific challenges in each step of the design and fabrication process are discussed in detail, and several applications are showed as examples. Our work will benefit people working in IME industry by providing systematic and seamless software-to-process workflow. Our future work will involve fully integrating our software with established IME process and conducting in-depth statistical technical evaluations on the proposed method.

5.4 References

[1] Accuform. T-sim. http://www.t-sim.com, Accessed: 2/10/2019.

[2] Rheoware. Rheoware. http://rheoware.com/, Accessed: 3/15/2019.

[3] Christian Schüller, Daniele Panozzo, Anselm Grundhöfer, Henning Zimmer, Evgeni Sorkine, and Olga Sorkine-Hornung. Computational thermoforming. *ACM Transactions on Graphics*, 35(4):1–9, 2016.

[4] Bart Plovie, Yang Yang, Joren Guillaume, Sheila Dunphy, Kristof Dhaenens, Steven Van Put, Björn Vandecasteele, Thomas Vervust, Frederick Bossuyt, and Jan Vanfleteren. Arbitrarily Shaped 2.5D Circuits using Stretchable Interconnects Embedded in Thermoplastic Polymers. *Advanced Engineering Materials*, 19(8):1–8, 2017.

[5] Jan Vanfleteren, Frederick Bossuyt, and Bart Plovie. A new technology for rigid 3D free-form electronics based on the thermoplastic deformation of flat standard PCB type circuits. *2016 12th International Congress Molded Interconnect Devices - Scientific Proceedings, MID 2016*, (Mid):1–4, 2016.

[6] Jonathan Ting, Yunbo Zhang, Sang Ho Yoon, James D. Holbery, and Siyuan Ma. IMold: Enabling interactive design optimization for in-mold electronics. *Conference on Human Factors in Computing Systems - Proceedings*, 2020.

[7] Jumana Abu-Khalaf, Razan Saraireh, Saleh Eisa, and Ala'Aldeen Al-Halhouli. Experimental characterization of inkjet-printed stretchable circuits for wearable sensor applications. *Sensors (Switzerland)*, 18(10):1–23, 2018.

[8] Binghao Wang and Antonio Facchetti. Mechanically Flexible Conductors for Stretchable and Wearable E-Skin and E-Textile Devices. *Advanced Materials*, 31(28):1–53, 2019.

[9] Charlie C.L. Wang. CyberTape: An interactive measurement tool on polyhedral surface. *Computers and Graphics (Pergamon)*, 28(5):731–745, 2004.

[10] Junichi Yamaoka and Yasuaki Kakehi. DrawForming. pages 615–620, 2016.

[11] Junichi Yamaoka, Yasuaki Kakehi, and Yoshihiro Kawahara. ActMold: Rapid prototyping of electronic circuits on 2.5D objects with interactive vacuum forming. *ACM SIGGRAPH 2017 Studio, SIGGRAPH 2017*, pages 2–3, 2017.

[12] Junichi Yamaoka and Yasuaki Kakehi. ProtoMold. pages 2106–2115, 2017.

[13] Bowei Zhang, Quan Dong, Can E. Korman, Zhenyu Li, and Mona E. Zaghloul. Flexible packaging of solid-state integrated circuit chips with elastomeric microfluidics. *Scientific Reports*, 3:1–8, 2013.

[14] Yunbo Zhang and Tsz Ho Kwok. An interactive product customization framework for freeform shapes. *Rapid Prototyping Journal*, 23(6):1136–1145, 2017.

[15] Yizhong Zhang, Yiying Tong, and Kun Zhou. Coloring 3d printed surfaces by thermoforming. *IEEE Transactions on Visualization and Computer Graphics*, 23(8):1924–1935, 2017.

[16] Sun Chemical. In-Mold Electronic Materials. https://www.sunchemical.com/product/%0Ain-mold-electronic-materials-ime, Accessed: 4/25/2021.

[17] DuPont. DuPont™ Intexar™ TE-11C Film – Insulectro. https://insulectro-pe.com/products/intexar™-te-11c-film, Accessed: 4/25/2021.

[18] DuPont. DuPont ™ ME902. *Technical Datasheet*, (K-29896):1–2, 2019. https://www.dupont.com/content/dam/dupont/amer/us/en/products/ei-transformation/documents/ME902.pdf.

[19] Base Film Te-c. Dupont ™ intexar ™ te-11c.

[20] Henkel. Loctite 3621. *Technical Datasheet*, 2014.

[21] Harish Devaraj and Rajiv Malhotra. Scalable forming and flash light sintering of polymer-supported interconnects for surface-conformal electronics. *Journal of Manufacturing Science and Engineering, Transactions of the ASME*, 141(4), 2019.

[22] Eastprint. IN-MOLD ELECTRONICS DESIGN & MANUFACTURING AT EASTPRINT, INC. https:%0A//www.eastprint.com/in-mold-electronics.html, Accessed: 4/25/2021.

[23] Ecm. Product List. http://www.conductives.com/new_products.php, Accessed: 4/21/2021.

[24] Khaled Elgeneidy, Gerhard Neumann, Michael Jackson, and Niels Lohse. Directly printable flexible strain sensors for bending and contact feedback of soft actuators. *Frontiers Robotics AI*, 5(FEB):1–14, 2018.

[25] Josue Ferri, Jose Vicente Lidón-Roger, Jorge Moreno, Gabriel Martinez, and Eduardo Garcia-Breijo. A wearable textile 2D touchpad sensor based on screen-printing technology. *Materials*, 10(12), 2017.

[26] Formech. Formech. https://formech.com/, Accessed: 1/2/2019.

[27] Karmen Franinović and Luke Franzke. Shape Changing Surfaces and Structures. pages 1–12, 2019.

[28] Richard Ghaffarzadeh, Khasha; Collins. In-Mold Electronics 2019-2029: Technology, Market Forecasts, Players. *Technical Report*, 2019.

[29] IDTechEx. In-Mold Electronics: challenges in every step?, 2019.

[30] Joshua A. Ledgerwood. Characterization of Flexible Hybrid Electronics Using. (June), 2017.

[31] Christine Kallmayer, Florian Schaller, Thomas Loher, Julian Haberland, Fabian Kayatz, and Andre Schult. Optimized Thermoforming Process for Conformable Electronics. *2018 13th International Congress Molded Interconnect Devices, MID 2018*, 2018.

[32] Anastasia Koivikko, Ehsan Sadeghian Raei, Mahmoud Mosallaei, Matti Mäntysalo, and Veikko Sariola. Screen-printed curvature sensors for soft robots. *IEEE Sensors Journal*, 18(1):223–230, 2018.

[33] Terho Kololuoma, Carlos Pinheiro, Ilkka Kaisto, Ashley Colley, Kari Ronka, Mikko Keranen, Timo Kurkela, Tuomas Happonen, Marko Korkalainen, Minna Kehusmaa, Lucia Gomes, Aida Branco, and Sami Ihme. Adopting Hybrid Integrated Flexible Electronics in Products: Case—Personal Activity Meter. *IEEE Journal of the Electron Devices Society*, 7(c):761–768, 2019.

[34] Ligang Liu, Lei Zhang, Yin Xu, Craig Gotsman, and Steven J. Gortler. A local/global approach to mesh parameterization. *Eurographics Symposium on Geometry Processing*, 27(5):1495–1504, 2008.

[35] Creative Materials. Conductive Silver Inks., 2019.

[36] Stefanie Mueller, Anna Seufert, Huaishu Peng, Robert Kovacs, Kevin Reuss, François Guimbretière, and Patrick Baudisch. Formfab: Continuous interactive fabrication. *TEI 2019 - Proceedings of the 13th International Conference on Tangible, Embedded, and Embodied Interaction*, pages 315–323, 2019.

[37] TactoTek Oy. Tacto Tek. https://tactotek.com, 10/30/2019.

[38] Omeed H. Paydar, Christopher R. Wottawa, Richard E. Fan, Erik P. Dutson, Warren S. Grundfest, Martin O. Culjat, and Rob N. Candler. Fabrication of a thin-film capacitive force sensor array for tactile feedback in robotic surgery. *Proceedings of the Annual International Conference of the IEEE Engineering in Medicine and Biology Society, EMBS*, pages 2355–2358, 2012.

[39] M. F.M. Sharif, A. A. Saad, M. Z. Abdullah, F. C. Ani, M. Y.T. Ali, M. K. Abdullah, M. S. Ibrahim, and Z. Ahmad. A study on thermoforming process of stretchable circuit and its performance in manufacturing of automotive lighting. *AIP Conference Proceedings*, 1901(December), 2017.

[40] Tom Sterken, Jan Vanfleteren, Tom Torfs, Maaike Op De Beeck, Frederick Bossuyt, and Chris Van Hoof. Ultra-Thin Chip Package (UTCP) and stretchable circuit technologies

for wearable ECG system. *Proceedings of the Annual International Conference of the IEEE Engineering in Medicine and Biology Society, EMBS*, pages 6886–6889, 2011.

[41] Jari Suikkola, Toni Björninen, Mahmoud Mosallaei, Timo Kankkunen, Pekka Iso-Ketola, Leena Ukkonen, Jukka Vanhala, and Matti Mäntysalo. Screen-Printing Fabrication and Characterization of Stretchable Electronics. *Scientific Reports*, 6(May):1–8, 2016.

[42] Pentti Karioja, Jukka-Tapani Mäkinen, Kimmo Keränen, Janne Aikio, Teemu Alajoki, Tuomo Jaakola, Matti Koponen, Antti Keränen, Mikko Heikkinen, Markus Tuomikoski, Riikka Suhonen, Leena Hakalahti, Pälvi Kopola, Jukka Hast, Ralf Liedert, Jussi Hiltunen, Noriyuki Masuda, Antti Kemppainen, Kari Rönkä, and Raimo Korhonen. Printed hybrid systems. *Nanosensors, Biosensors, and Info-Tech Sensors and Systems 2012*, 8344(March 2012):83440G, 2012.

Chapter 6

Conclusions and future outlook

In this dissertation, we first presented an overview of flexible electronics, as well as various printing techniques. We then further discussed the integration of conventional rigid electronics with flexible electronics, and defined flexible hybrid electronics, as well as an empirical system. In Chapter 2, we presented an example of passive printed sensors, printed thermistor arrays. We overviewed the fabrication process of the fully screen-printed arrays, and explored the optimization of custom screen-printable NiO inks. We further demonstrated the efficacy of the printed arrays by using them to plot temperature maps of a commercial lithium-ion battery discharged at various C-rates. For examples of printed active sensors, in Chapter 3, we presented an all-organic optoelectronic sensor for pulse oximetry. We thoroughly discussed the two fabrication processes involved for OLED and OPD devices, and demonstrated the viability of the printed devices as biophotonic sensors. Furthermore, we discussed various alternate geometries of OLEDs and OPDs, used in a single pixel sensor, and how they could influence the PPG signal magnitude. In Chapter 4 we introduce a possible solution to printed energy sources for FHE, printed Zn-Ag$_2$O battery arrays. We discuss the unique vertical geometry enabling series connection between adjacent cells, the Zn and Ag$_2$O ink optimization for screen-printing, as well as the fabrication process. Finally in Chapter 5, we discuss an extension of printed flexible electronics, in-mold electronics. Specifically addressing the challenge of developing electronics for highly custom surfaces, a process to fabricate printed electronics on 2D and then form them into 3D functional electronics was outlined, and several example works were discussed.

Overall, we demonstrated a wide range of printed components for flexible hybrid electronics - passive sensors, active sensors, and batteries. The sensor development, fabrication, and characterization are also discussed in detail. The bulk of the work in this dissertation still utilize rigid PCBs to interface with printed sensors, however we demonstrated the viability and compatibility of printed electronics and conventional rigid electronics. Furthermore, this dissertation presented a wide range of potential applications for the various printed works we demonstrated.

As we continue to add additional devices, printing methods, and integration techniques to our repertoire, we continue to broaden our horizons for potential applications of flexible

hybrid electronics. The materials and methods used here can be easily extended to areas outside of the examples discussed in this dissertation. Some of the prospective projects and applications for future work are listed below:

1. Integrated impedance and optoelectronic sensors for wound monitoring and stimulation

2. Printed sensors for food packaging

3. Printed vias enabling double-sided electronics

4. SimuPrint: Multi-functional single substrate printed electronics

6.1 Integrated impedance and optoelectronic sensors for wound monitoring and stimulation

Annually in the US there are over 72 million instances of acute wounds from accidents or surgical procedures, and chronic wounds affect approximately 6.5 million patients, which amounts to \$15 billion in wound care product costs in 2010. Innovations in wound dressings has advanced towards incorporating diagnostic sensors to assess wound conditions such as oxygen level, pH, and bacterial growth to reduce treatment delays. In contrast, the therapeutic strategies are lagging behind and mostly limited to moisture control and anti-microbial agents. By developing an integrated theranostic device with both sensing and stimulating capabilities, a disruptive treatment platform to both monitor and accelerate wound healing could be realized [1–11].

For both acute and chronic cutaneous wounds, the use of electrical stimulation (ES) in conjunction with the standard care is shown to speed up healing. In ES therapy a low current less than 1 mA is applied to the wound region by putting electrodes on or near the damaged skin tissues. ES is effective for pain management as established in a double-blind study. This method was granted FDA pre-market approval in 2002 for clinical use on chronic wounds that fail to heal with standard care. The Centers for Medicare and Medicaid Services have issued a national coverage decision to pay for ES therapy for conditions such as stage 3 and 4 chronic wounds. However, there is an adoption barrier to the ES therapy, due to the costs of the electrodes and the labor required in attaching the multitude of electrodes. An integrated monitoring and treatment system will overcome this usage barrier [1–9].

Flexible electronics for medical sensing is advantageous compared to conventional rigid electronics due to the conformal nature of flexible electronics. By maintaining high quality conformal interfaces with the body, flexible electronics can extract biomedical signals with higher signal to noise ratio (SNR). In addition, many of the current developments in flexible wearable electronics involve using soft and pliable substrates, some even stretchable, which improve the quality of comfort for a wearable device when compared to rigid ones.

Previously from our group, we reported on printed flexible impedance electrodes used for mapping pressure ulcer progression [12]. The observation was that there is a correlation

between the status of the wound and the impedance measurements. A flexible array was used to map the wound, which has the advantage discussed above, a highly conformal interface enabling high quality signal acquisition.

In addition to the impedance spectroscopy method, wound oxygenation measurements would be useful for physicians to monitor the status of the wound. As discussed in Chapter 3, a flexible reflectance oximeter offers many advantages over the conventional transmission mode finger probe used in most hospitals [12–18]. A smart bandage that uses both impedance spectroscopy and tissue oxygenation to monitor wound health would provide information to healthcare providers on whether a wound is healing or not, with the additional signal redundancy from two different sources. As seen in Figure 6.1a, by placing the sensor directly on top of the wound, it would function two-fold: as an encapsulation to the open wound, as well as providing valuable sensor data to healthcare providers. In this particular sensor, printed gold electrodes are used to collect the impedance data from the wound, while the printed optoelectronics are used to perform tissue oxygenation measurements. In addition to the impedance measurements, the printed gold electrodes in Figure 6.1b can be used to source low amounts of current to the wound, as a form of electrostimulation. After the sensor data has been collected, it can be reconstructed on a 2D surface to show the interpolated wound area and status over a period of time, shown in Figure 6.1c.

6.2   Printed sensors for food packaging

There is an increasing demand for detecting the freshness and safety of food with continuous monitoring techniques, allowing users to track the quality of their food throughout the packing and shipping process. This end-to-end monitoring requires intelligent food packaging that can relay the status of the food intermittently to users. There are a variety of signals of interest to report on. Environmental factors like temperature, humidity, and tamper protection are already commonly monitored [19]. However, other internal environmental factors like gas composition, microorganisms, and light are not frequently monitored. Because of the varying types of form factors foods can be packaged in, printed flexible electronics are a great form factor for food monitoring sensors. Especially with the advancements in near-field communication (NFC) and radio frequency identification (RFID), there has been an increase in sensor tags in the realm of printed electronics. Some works have reported on polling sensor tags intermittently to acquire tag data to be transmitted, and others have reported on direct integration of printed sensors into the food packaging [19–21]. As discussed in this dissertation, there are already many existing printed sensors that can detect signals such as light, gas composition, temperature, etc. In addition, there have been significant advancements in the realm of printed antennas [22, 23], allowing for seamless antenna integration into flexible sensor form factors.
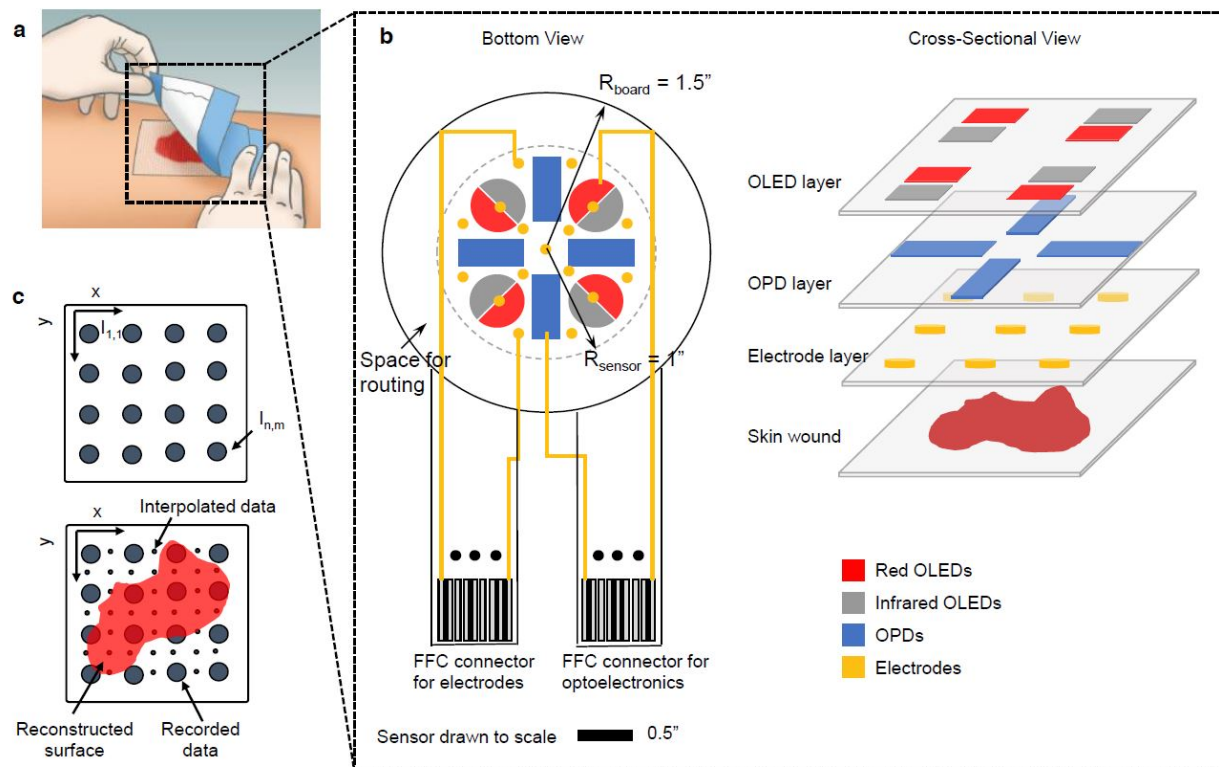
Figure 6.1: **Integrated impedance and optoelectronic sensors for wound monitoring and stimulation. (a)** Proposed wound monitoring patch placement on open wound. **(b)** Bottom and cross-sectional view of proposed patch. **(c)** Collected data visualized on 2D plane from measured optoelectronic and impedance sensor data.

6.3   Printed vias enabling double-sided electronics

Currently, commercial printed circuit boards can accommodate significantly more complex circuit designs than printed electronics reported in literature are capable of. One step towards bridging the gap in design complexity between the two would be to develop printed vias for printed electronics. By doing so, printed electronics would be able to accommodate double sided electronic designs - electronics on one side of a substrate would be able to interface with the other side without wires or additional complexity. Kujala et al. demonstrated a screen-printed conductive via through a laser-cut opening in PET [24]. By varying the diameter of the cut, they were able to improve the quality of connection through the via. This method is viable, however is susceptible to failure due to the nature of most printed silver inks. Because most of the screen-printed silver inks used commercially are somewhat brittle, flexing a via printed with this method could result in microcracking, and ultimately increase via resistance.

However, another work from Yamaoka, et al. used a rigid eyelet to improve the quality of their vias [25]. Although this work primarily uses laser cut copper tape for conductive traces, the idea of using eyelets as a rigid interface for traces on both sides of a substrate is interesting. This particular solution can improve the quality of contact and overall conductivity of traces during flexing, and potentially mitigate the problem overviewed above. By combining the screen-printed vias with the rigid eyelet, we could potentially develop printed vias that enable double-sided electronics. As part of my internship at Microsoft, I explored this idea very briefly and prototyped a potential printed via with eyelet and show the conductivity of this flexible via in Figure 6.2. Openings were made in a flexible substrate using laser cutting, and conductive traces were screen-printed on both sides in a cross-shaped pattern. Finally, an eyelet was attached to reinforce the via. Using a multimeter, I was able to validate the via was conductive, even while flexed.

6.4   SimuPrint: Multi-functional single substrate printed electronics

Previously, work has been demonstrated from our group realizing printed multi-color OLEDs on a single substrate [26]. As an extension of this work, it would be interesting to pursue if we could realize a single substrate with two different functionalities, with a single print process. In Figure 6.3a, we can see the proposed fabrication process for SimuPrint. Starting with a bare PEN/ITO substrate, the substrate is uniformly treated with a self-assembled monolayer of fluorosilane, making the substrate uniformly hydrophobic. From there, regions are masked off with Kapton tape and the exposed regions are treated with an air plasma, etching away the monolayer. This leaves the exposed areas locally hydrophilic. From there, PEDOT:PSS is doctor blade coated over the two hydrophilic lanes, and the individual active layers for the functional materials are subsequently blade coated. For this work, a proposed OLED and OPD are fabricated adjacent to each other, and as such the

emissive layer and bulk heterojunction of the OLED and OPD, respectively, are printed. From there, the devices are ready for evaporation. A pixel schematic of the two devices can be found in Figure 6.3b, and the printed substrate can be found in Figure 6.3c. This is a work in progress, and further characterization results on the individual devices, as well as the optimzation process, will be reported on in a future publication.

6.5   Outlook

Researchers have continued to push the limits of flexible and printed electronics, optimizing their performance and tuning their manufacturing processes such that they can be scaled to commercial levels of production. Conventional semiconductor processing is still limited compared to printed electronics, especially when vacuum processing is involved due to how difficult it is to scale to large area. Eventually, if we would be able to manufacture printed electronics on a R2R scale of production, as well as minimize the amount of conventional solid-state electronics we use, FHE can be the ideal platform for flexible electronics. By combining this form factor of electronics with advancements in machine learning and on-chip processing, FHE can provide the best end-user experience for flexible sensing applications, especially in the wearables market. With an additional 10 - 20 years of continued research, we believe that FHE can be optimized for low-cost large-area manufacturing, and address many challenges in the printed electronics community for years to come.

Figure 6.2: **Prototype screen-printed via with eyelet reinforcement. (a)** Screen-printed traces on flexible Kapton substrate with eyelet reinforcement. **(b)** and **(c)** Resistance measurement of unflexed via on Kapton and flexed via on Dupont Intexar substrates, respectively.
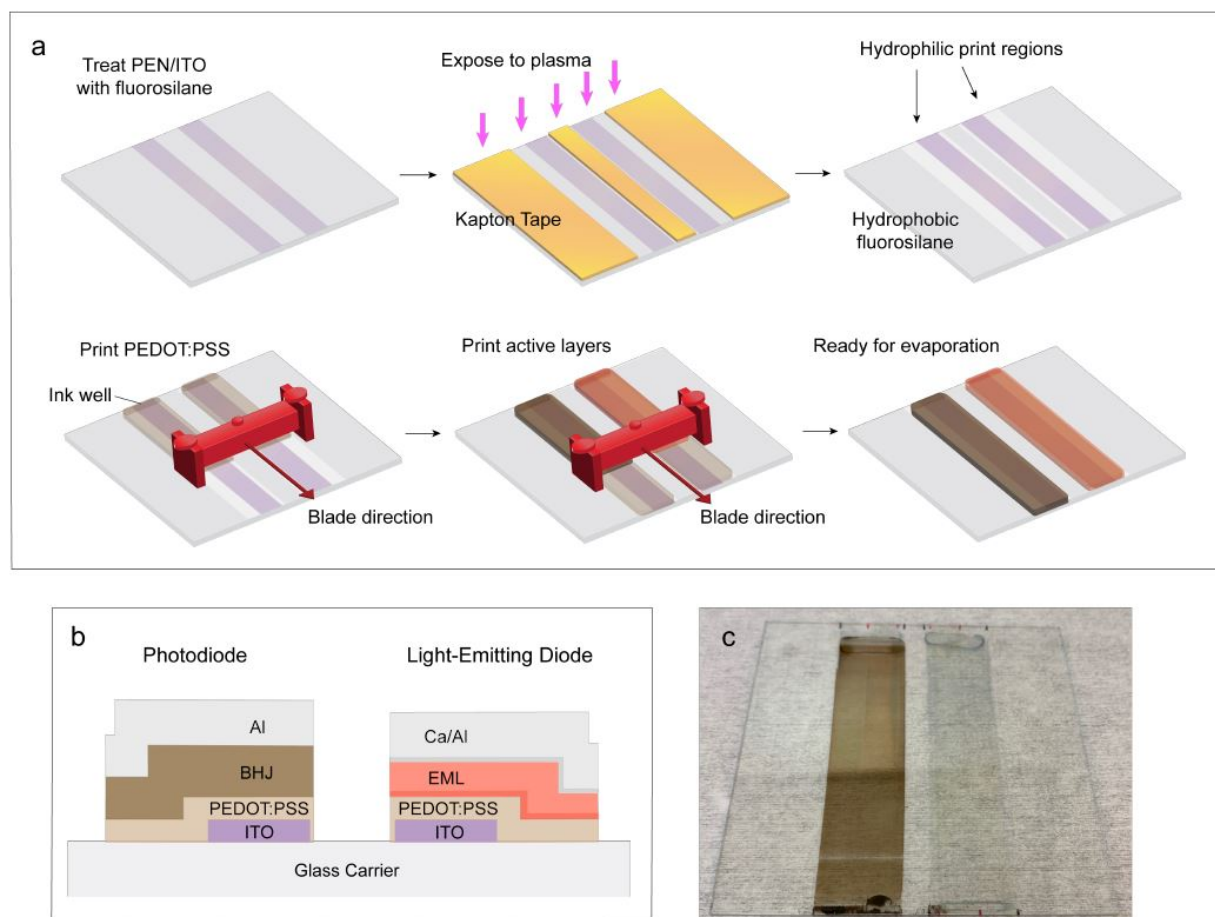
Figure 6.3: **Overview of fabrication for multi-functional single substrate electronics. (a)** Schematic of fabrication process. **(b)** OPD and OLED layer schematic. **(c)** Photo of printed OPD and OLED layers on PEN substrate.

6.6   References

[1] Min Zhao, Bing Song, Jin Pu, Teiji Wada, Brian Reid, Guangping Tai, Fei Wang, Aihua Guo, Petr Walczysko, Yu Gu, Takehiko Sasaki, Akira Suzuki, John V. Forrester, Henry R. Bourne, Peter N. Devreotes, Colin D. McCaig, and Josef M. Penninger. Electrical signals control wound healing through phosphatidylinositol-3-OH kinase-γ and PTEN. *Nature*, 442(7101):457–460, 2006.

[2] Min Zhao. Electrical fields in wound healing-An overriding signal that directs cell migration. *Seminars in Cell and Developmental Biology*, 20(6):674–682, 2009.

[3] Richard Nuccitelli, Pamela Nuccitelli, Changyi Li, Suman Narsing, David M. Pariser, and Kaying Lui. The electric field near human skin wounds declines with age and provides a noninvasive indicator of wound healing. *Wound Repair and Regeneration*, 19(5):645–655, 2011.

[4] Sara Ud-Din, Anil Sebastian, Pamela Giddings, James Colthurst, Sigrid Whiteside, Julie Morris, Richard Nuccitelli, Christine Pullar, Mo Baguneid, and Ardeshir Bayat. Angiogenesis is induced and wound size is reduced by electrical stimulation in an acute wound healing model in human skin. *PLoS ONE*, 10(4):1–22, 2015.

[5] Chao Yu, Zong-Qian Hu, and Rui-Yun Peng. Effects and mechanisms of a microcurrent dressing on skin wound healing: a review. *Military Medical Research*, 1(1):24, 2014.

[6] Sara Ud-Din and Ardeshir Bayat. Electrical Stimulation and Cutaneous Wound Healing: A Review of Clinical Evidence. *Healthcare*, 2(4):445–467, 2014.

[7] Luther C. Kloth. Electrical stimulation for wound healing: A review of evidence from in vitro studies, animal experiments, and clinical trials. *International Journal of Lower Extremity Wounds*, 4(1):23–44, 2005.

[8] Gaurav Thakral, Javier LaFontaine, Bijan Najafi, Talal K. Talal, Paul Kim, and Lawrence A. Lavery. Electrical stimulation to accelerate wound healing. *Diabetic Foot and Ankle*, 4(February), 2013.

[9] Chandan K. Sen, Gayle M. Gordillo, Sashwati Roy, Robert Kirsner, Lynn Lambert, Thomas K. Hunt, Finn Gottrup, Geoffrey C. Gurtner, and Michael T. Longaker. Human skin wounds: A major and snowballing threat to public health and the economy: PERSPECTIVE ARTICLE. *Wound Repair and Regeneration*, 17(6):763–771, 2009.

[10] Manuel Ochoa, Rahim Rahimi, and Babak Ziaie. Flexible sensors for chronic wound management. *IEEE Reviews in Biomedical Engineering*, 7:73–86, 2014.

[11] Tim R. Dargaville, Brooke L. Farrugia, James A. Broadbent, Stephanie Pace, Zee Upton, and Nicolas H. Voelcker. Sensors and imaging for wound healing: A review. *Biosensors and Bioelectronics*, 41(1):30–42, 2013.

[12] Yasser Khan, Felippe J. Pavinatto, Monica C. Lin, Amy Liao, Sarah L. Swisher, Kaylee Mann, Vivek Subramanian, Michel M. Maharbiz, and Ana C. Arias. Inkjet-Printed Flexible Gold Electrode Arrays for Bioelectronic Interfaces. *Advanced Functional Materials*, 26(7):1004–1013, 2016.

[13] Tomàs Guinovart, Gabriela Valdés-Ramírez, Joshua R. Windmiller, Francisco J. Andrade, and Joseph Wang. Bandage-Based Wearable Potentiometric Sensor for Monitoring Wound pH. *Electroanalysis*, 26(6):1345–1353, 2014.

[14] Michael Jünger, Andreas Arnold, Daniel Zuder, Hans Werner Stahl, and Susanna Heising. Local therapy and treatment costs of chronic, venous leg ulcers with electrical stimulation (Dermapulse®): A prospective, placebo controlled, double blind trial. *Wound Repair and Regeneration*, 16(4):480–487, 2008.

[15] Sonja A. Weber, Niall Watermann, Jacques Jossinet, J. Anthony Byrne, Jonquille Chantrey, Shabana Alam, Karen So, Jim Bush, Sharon O'Kane, and Eric T. McAdams. Remote wound monitoring of chronic ulcers. *IEEE Transactions on Information Technology in Biomedicine*, 14(2):371–377, 2010.

[16] Sarah L. Swisher, Monica C. Lin, Amy Liao, Elisabeth J. Leeflang, Yasser Khan, Felippe J. Pavinatto, Kaylee Mann, Agne Naujokas, David Young, Shuvo Roy, Michael R. Harrison, Ana Claudia Arias, Vivek Subramanian, and Michel M. Maharbiz. Impedance sensing device enables early detection of pressure ulcers in vivo. *Nature Communications*, 6:1–10, 2015.

[17] Amy Liao, Monica C. Lin, Lauren C. Ritz, Sarah L. Swisher, David Ni, Kaylee Mann, Yasser Khan, Shuvo Roy, Michael R. Harrison, Ana C. Arias, Vivek Subramanian, David Young, and Michel M. Maharbiz. Impedance sensing device for monitoring ulcer healing in human patients. *Proceedings of the Annual International Conference of the IEEE Engineering in Medicine and Biology Society, EMBS*, 2015-November:5130–5133, 2015.

[18] Claire M. Lochner, Yasser Khan, Adrien Pierre, and Ana C. Arias. All-organic optoelectronic sensor for pulse oximetry. *Nature Communications*, 5:1–7, 2014.

[19] Yu Liao, Rui Zhang, and Jun Qian. Printed electronics based on inorganic conductive nanomaterials and their applications in intelligent food packaging. *RSC Advances*, 9(50):29154–29172, 2019.

[20] Nattinee Bumbudsanpharoke, Jungwook Choi, and Seonghyuk Ko. Applications of nanomaterials in food packaging. *Journal of Nanoscience and Nanotechnology*, 15(9):6357–6372, 2015.

[21] Giovanni A. Salvatore, Jenny Sülzle, Filippo Dalla Valle, Giuseppe Cantarella, Francesco Robotti, Petar Jokic, Stefan Knobelspies, Alwin Daus, Lars Büthe, Luisa Petti, Norbert

Kirchgessner, Raoul Hopf, Michele Magno, and Gerhard Tröster. Biodegradable and Highly Deformable Temperature Sensors for the Internet of Things. *Advanced Functional Materials*, 27(35):1–10, 2017.

[22] Carol L. Baumbauer, Matthew G. Anderson, Jonathan Ting, Akshay Sreekumar, Jan M. Rabaey, Ana C. Arias, and Arno Thielens. Printed, flexible, compact UHF-RFID sensor tags enabled by hybrid electronics. *Scientific Reports*, 10(1):1–12, 2020.

[23] Yasser Khan, Arno Thielens, Sifat Muin, Jonathan Ting, Carol Baumbauer, and Ana C. Arias. A New Frontier of Printed Electronics: Flexible Hybrid Electronics. *Advanced Materials*, 32(15):1–29, 2020.

[24] Manu Kujala, Terho Kololuoma, Jari Keskinen, Donald Lupo, Matti Mantysalo, and Thomas M. Kraft. Screen Printed Vias for a Flexible Energy Harvesting and Storage Module. *2018 International Flexible Electronics Technology Conference, IFETC 2018*, m:1–6, 2018.

[25] Junichi Yamaoka, Mustafa Doga Dogan, Katarina Bulovic, Kazuya Saito, Yoshihiro Kawahara, Yasuaki Kakehi, and Stefanie Mueller. FoldTronics: Creating 3D objects with integrated electronics using foldable honeycomb structures. *Conference on Human Factors in Computing Systems - Proceedings*, 2019.

[26] Donggeon Han, Yasser Khan, Jonathan Ting, Simon M. King, Nir Yaacobi-Gross, Martin J. Humphries, Christopher J. Newsome, and Ana C. Arias. Flexible Blade-Coated Multicolor Polymer Light-Emitting Diodes for Optoelectronic Sensors. *Advanced Materials*, 29(22), 2017.